Near-Infrared Quantum Dots For Bioimaging And Targeting Applications

by

Chai Hoon Quek

Department of Mechanical Engineering & Materials Science
Duke University

Date:_____

Approved:

_____
Prof. Kam W. Leong, Supervisor

_____
Prof. Piotr Marszalek

_____
Prof. Stefan Zauscher

_____
Prof. Mark Wiesner

Dissertation submitted in partial fulfillment of
the requirements for the degree of Doctor
of Philosophy in the Department of
Mechanical Engineering & Materials Science in the Graduate School
of Duke University

2014

ABSTRACT

Near-Infrared Quantum Dots For Bioimaging And Targeting Applications

by

Chai Hoon Quek

Department of Mechanical Engineering & Materials Science
Duke University

Date:_____

Approved:

_____
Prof. Kam W. Leong, Supervisor

_____
Prof. Piotr Marszalek

_____
Prof. Stefan Zauscher

_____
Prof. Mark Wiesner

An abstract of a dissertation submitted in partial
fulfillment of the requirements for the degree
of Doctor of Philosophy in the Department of
Mechanical Engineering & Materials Science in the Graduate School of
Duke University

2014

Abstract

A series of silver-doped zinc slelenide quantum dots were synthesized in aqueous medium with emission across the visible and near-infrared region. These QDs were evaluated in vitro with rat macrophages cell line (RAW 264.7) and human mesenchymal stem cells (*h*MSC). Viability assay indicates that these quantum dots have low cytotoxicity in duration of 24 h. In vivo biodistribution study shows that these bare QDs are different from conventional QDs, it traversed through systemic route and could accumulate in the stomach of nude mice. We performed conjugation of the QDs to monoclonal CD44v6 antibody and tested with human gastric adenocarcinoma cell lines found validated the targeting specificity property of these QDs. The QDs were also conjugated to heparin and used to formulate nanocomplexes with chitodan to encapsulate tumor necrosis factor-alpha. Quantitative imaging analysis revealed in vivo trafficking kinetics of the NPs to the lymph nodes after subcutaneous administration into nude mice. This study demonstrates the potential of incorporation of near-infrared-emitting QDs in nanocarrier drug delivery allows effective in vivo trafficking of the biodistriution events and will be of greatly improve the development new drug nanocarrier formulations.

Contents

List of Tables

List of Figures

Acknowledgements

First of all, I would like to express my deepest thanks and appreciation to my advisor, Prof. Kam Leong for his invaluable guidance, advice and support. My sincere appreciation is extended to my committee members, Dr. Piotr Marszalek, Dr. Stefan Zauscher and Dr. Mark Wiesner for their support throughput this study.

I would like to acknowledge the financial support of the CEINT at Duke University and Medtronic. A big thank you Honfai Chan, Dr. James Fang, Prof. Soman Abraham, Mohammed Arifuzzaman, Dr. Cheryl Chan, Dr. Anthony Ribeiro, Prof. Chilkoti, Prof. Sempowski, Kristina Riebe, Michelle Gignac, Dr. Steve Zhang for their help rendered. Special thanks to all the lab members if Leong Lab and administrative staffs of MEMS Department in Duke University for their assistance at one time or another.

Finally, I would like to extend my heartfelt appreciation to my family and friends for their spiritual support and encouragement.

Chapter 1

Introduction

1.1 Overview

Nanotechnology is a fast growing field aiming to develop products that can possibly bring improvements to the life of human beings. Among the many different products created from nanotechnology, quantum dots (QDs) are the most widely studied and have being fabricated into several commercial applications such as quantum dots light emitting diodes (Colvin *et al.* 1994; Coe *et al.* 2002), electronic displays (Cho *et al.* 2009) and solar cell panels (Schuler *et al.* 2007; Sargent 2012; Semonin *et al.* 2012). Recently, QDs are also gaining popularity in biomedical research as imaging probes due to their unique physiochemical and optical properties (Alivisatos *et al.* 2005; Zhang *et al.* 2008). They have narrow emission spectra tunable by size and/or composition (Alivisatos 1996), exceptional brightness and photostability (Michalet *et al.* 2005) and their surface are amenable to incorporate functional groups (Clapp *et al.* 2006; Mei *et al.* 2009; Susumu *et al.* 2009).

QDs are typically comprised of binary combination of elements from periodic groups of II-VI (CdSe and CdTe), III-V (InP and InAs) or IV-VI (PbS), affording a range of emission wavelengths from the UV to the near infrared. To date, majority of quantum dots that are commercially available are CdSe, CdTe

and PbSe that are typically synthesized in organic solvents and high temperatures (Murray *et al.* 2000). With the implementation of the "Restriction of Hazardous Substances Directive" (RoHS) in February 2003 by the European Union and January 2007 in California, there is an increasing awareness to phase out the use of cadmium, lead and other heavy metal-containing quantum dots in the consumer products.

To circumvent this issue, significant efforts are invested to develop safe alternatives to toxic metal-containing QDs (Pons *et al.* 2010; Park *et al.* 2011; Zhang *et al.* 2011). However, to our knowledge, all these reported systems are based on the conventional high temperature synthesis strategies. In 2007, many researchers were overwhelmed by the achievement of Rogach *et. al.* in developing an aqueous route to prepare thiol-capped cadmium telluride (Rogach *et al.* 2007) and set the pace for intensive research to develop green chemistry for producing QDs. Nonetheless, aqueous synthetic route to produce heavy metal-free, near-infrared emitting QDs is still lacking. We propose here to develop a rational green synthetic strategy to produce novel heavy metal-free zinc selenide (ZnSe) based QDs that will potentially can be applied to biomedical research. We will first explore to find a suitable hydrophilic stabilizer that will produce stable ZnSe QDs in aqueous phase. Once we establish the base conditions for the synthesis, we will utilize the doping technology commonly used in semiconductor production (Cao 2011) and incorporate trace amount of dopant into the ZnSe QDs. The findings of Peng *et. al. (Chen et al. 2009; Xie et al. 2009)*

and Zheng *et. al. (Xing et al. 2008)* indicated that copper dopant can be used to tune the emission towards higher wavelength. In this thesis, the effect of inclusion of salts of group 11 elements of the periodic table in the QDs synthesis will be investigated. After we ascertain the parameters to produce stable, visible to near-infrared emitting QDs, we will continue to assess its optical, structural, size and surface charge characteristics. Thereafter, we will perform proof-of-concept experiments to demonstrate the versatile biomedical applications of the QDs the with two different model systems: (1) for specific cell labeling study whereby QDs conjugated with a primary monoclonal antibody will be used to target the surface glycoprotein CD44v6 antigen that is expressed by early gastric adenocarcinoma cancer cell line; (2) to probe the *in vivo* trafficking of QDs-labeled drug nanocarrier in a nude mouse model. Depicted in Figure 1 is the overview of the specific aims of this thesis.

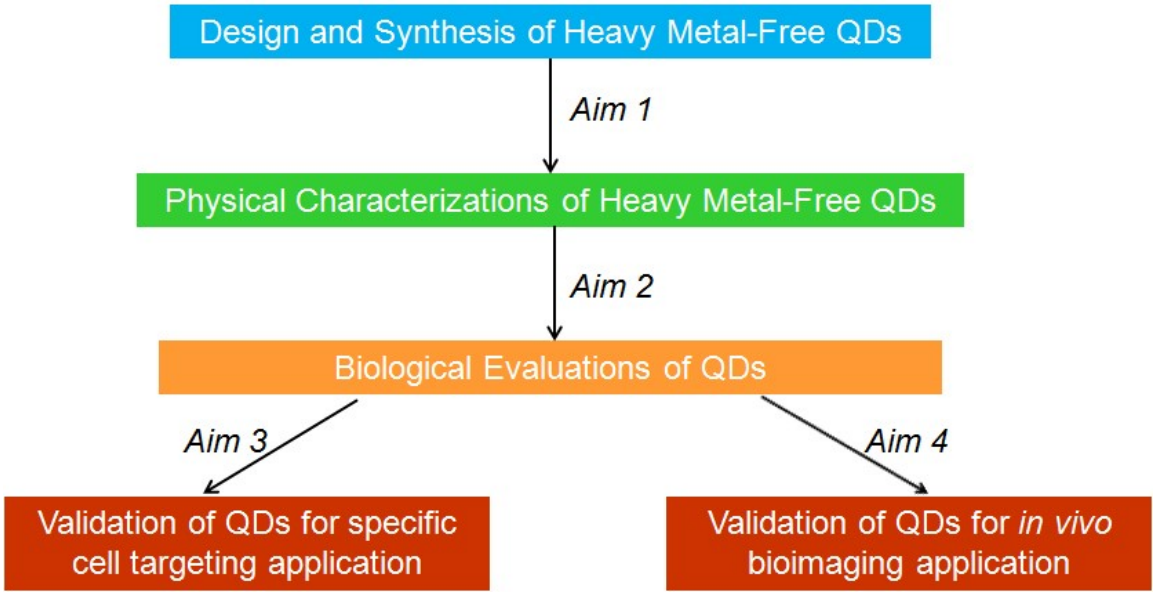

Figure 1. Overview of specific aims. The specific aims of this project will explore the development and characterization of a novel, heavy-metal free QDs as well as to evaluate their potential for biomedical applications.

1.2 Thesis Organization

The present work is organized in the following way. Chapter 2 will provide an overview of near-infrared fluorescent nanoprobes with applications specifically in the area of *in vivo* optical imaging. Succeeding chapters will show how we have designed new heavy-metal free QDs for bioimaging and targeting applications.

Chapter 3 will discuss the synthesis of group 11 transition metal-doped zinc selenide quantum dots (QDs) which emit in the visible to near-infrared regions. The challenges faced in dopant selection, optimization of growth rate and emission are addressed. Optical, size and structural characterizations of these QDs will also be presented.

Chapter 4 covers the biological evaluations of the QDs. In this section, we sought to address (1) if the presence of QDs perturb biological function and (2) can the optical properties of QDs be upheld in biological environments?

Chapter 5 will illustrate the versatility of conducting surface decoration of QDs with specific targeting moiety. The antibody we will use for this study is a primary monoclonal antibody against CD44v6 antigen. The challenge to prevent the conjugation at the active sites of the antibody will be discussed. The antibody affinity after conjugation reaction will be determined by cellular study.

Chapter 6 will concentrate on our effort to establish the near-infrared emitting QDs as a nanoprobe for delivery to the lymph nodes. The challenges to (1) control the size of the QD-labeled nanocomplexes to below 80 nm and (2) scrutinize the stability of the nanocomplexes during the *in vivo* study will be dealt in this section.

Chapter 7 then summarized the research work and highlights the unique properties and limitations of our approach. It also covers some of the future research directions that can stem from this work.

Chapter 2

Near-Infrared Fluorescent Nanoprobes for *in Vivo* Optical Imaging

2.1 Introduction

The first medical imaging was realized in the late 1895 by Wilhelm Röntgen shortly after he discovered X-ray and applied to capturing the images of the bones of a hand on film (Kevles 1997). The immediate consequence of this discovery triggered intense development of new imaging technologies, such as X-ray computed tomography, magnetic resonance imaging, positron emission tomography, ultrasound and optical imaging, that are indispensable to diagnostic medicine (Table 1) (Massoud *et al.* 2003; Rudin *et al.* 2003). These imaging technologies differ predominantly in the following aspects: resolution, penetration depth, temporal resolution and energy expended for generation of the image.

Today, these modern imaging technologies coupled with newly developed imaging probes are widely used in monitoring disease progression, interrogating cellular and molecular events, evaluating safety and toxicology in drug discovery and development, and assessing therapeutic efficacy *in vivo* (Weissleder 2001; Contag 2002; Weissleder 2002; Rudin *et al.* 2003; Gross *et al.* 2006; Hargreaves 2008; Rudin 2009; Dufort *et al.* 2010; Koba *et al.* 2011; Sivaraman *et al.* 2011). Among the different imaging modalities, optical imaging, which owes its origin to single-cell *in vitro* studies, is attractive for small animal imaging because of its

lower cost, portability, and potentially high spatial resolution with customizable fine-tuning. Despite being one of the most attractive techniques to provide noninvasive and nonionizing *in vivo* visualization (Hickson 2009), optical imaging is impeded by the tendency of living biological tissues to absorb and scatter photons and generate strong autofluorescence, which interferes with signal collection and processing (Figure 2) (Frangioni 2003). In addition, living tissues also contain other major NIR absorbers, such as water, lipids oxyhemoglobin and deoxyhemoglobin (Weissleder 2001) that prove challenging for optical imaging. To overcome these barriers, intense research has focused on developing highly sensitive and efficient fluorescent probes that function in the biologically transparent window of the first and second NIR region (NIR I, 650–950 nm, and NIR II, 1000–1350 nm) (Figure 3) (Smith *et al.* 2009). Near-infrared (NIR) fluorescent probes offer advantages of high photon penetration, reduced light scattering and minimal autofluorescence from living tissues, rendering them valuable for noninvasive mapping of molecular events, assessment of therapeutic efficacy, and monitoring of disease progression in animal models. This review will provide a broad overview of the available NIR fluorescent probes, their optical properties and potential applications for *in vivo* imaging.

Table 1. Overview of imaging systems for small animals.

Modality	Resolution	Depth	Optimal use	Signal	Training/ expertise required	Cost [+]
MRI	10–100 μm	No limit	Anatomical assessment, investigation of physiological, metabolic, molecular and genetic events.	RF[*] waves (Nonionizing radiation)	Yes (Certified radiologists)	$$$
PET	0.8–1.4 mm	No limit	Investigation of physiological, metabolic, molecular and genetic events.	γ-rays (Ionizing radiation)	Yes (Certified radiologists)	$$$
SPECT	0.8–1.4 mm	No limit	Investigation of physiological, metabolic, molecular and genetic events.	γ-rays (Ionizing radiation)	Yes (Certified radiologists)	$$
CT	50 μm	No limit	Anatomical assessment.	X-ray (Ionizing radiation)	Yes (Certified radiologists)	$$
Ultrasound	50 μm	mm	Anatomical assessment, investigation of physiological, metabolic, molecular and genetic events.	Sound waves (Nonionizing radiation)	Yes (Certified sonographers)	$$
Fluorescence optical imaging	0.3 μm	<1 cm	Metabolic, molecular and genetic events.	Light waves (Nonionizing radiation)	No	$

MRI, Magnetic resonance imaging; PET, Positron emission tomography; SPECT, Single photon emission computed tomography; CT, Computed tomography. [*]RF, radiofrequency, [+]Cost of system: $ < 100,000; $$ 100–300,000; $$$ 1–3 millions.

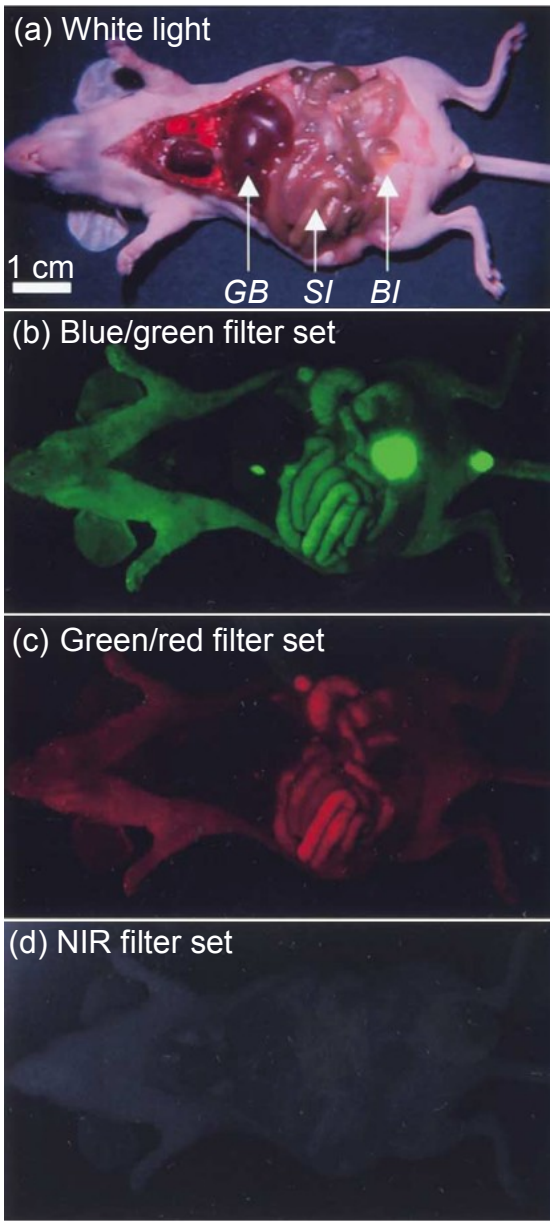

Figure 2. Wavelength-dependent autofluorescence of vital organs and body fluids. (a) Image of the viscera of an athymic nude mouse taken immediately after sacrifice. The arrows indicate the location of gall bladder (GB), small intestine (SI) and bladder (BI). Tissue autofluorescence was imaged using three different excitation/emission filter sets; (b) blue/green (460–500 nm/505–560 nm); (c) green/red (525–555 nm/590–650 nm); and (d) Near-infrared (NIR) (725–775 nm/790–830 nm). (Reprinted with permission from (Frangioni 2003), copyright 2003 Elsevier).

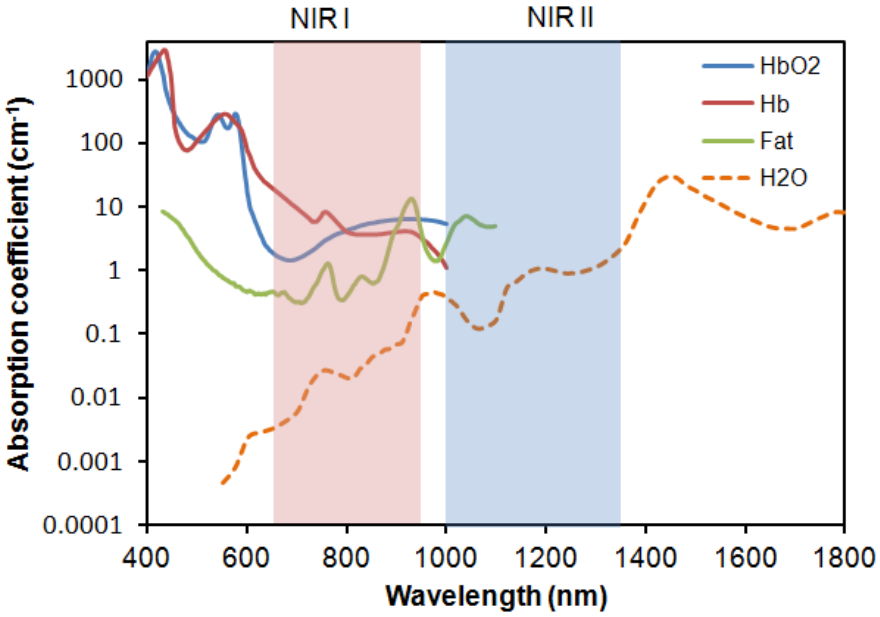

Figure 3. Absorption coefficient (on a log scale) of oxygenated blood, deoxygenated blood, fatty tissue and water as a function of wavelength *(*Quek *et. al.* 2012).

2.2 Labeling Mechanism of Fluorescent Probes

Optical imaging has increasingly been used for dynamic noninvasive imaging of biological events in mouse models. Due to the lack of NIR fluorescence contrast generated by most tissues in the biological transparency window, exogenous fluorescent probes have to be administered for *in vivo* studies in order to visualize living tissues in its native physiological state. Ideally, the fluorescent probes to be administered should be biologically stable in the *in vivo* environment, and accumulate and produce imaging contrast at the target site. Fluorescent probes are classified according to their mechanism of contrast generation, collectively as non-specific, targeting and activatable (Figure 4) (Weissleder 2002).

Non-specific probes simply have differential distribution and are used to assess physiological processes such as changes in blood volume, permeability and perfusion in angiogenesis (Figure 4a). Typically, they achieve only low target-to-background signals due to the non-binding circulating probes producing significant background fluorescence within the compartment.

Tissue- or cell-specific contrast is created by coupling a targeting moiety to a fluorescent probe that binds specifically to a receptor thus generating the readout signal (Figure 4b). These probes can report more detailed information about the biological events than non-specific probes. Targeting probes can achieve high target-to-background signals provided the targeting moiety has a high affinity for the receptor and any unbound probes are thoroughly removed from the system, thereby reducing the background fluorescence.

Activatable probes comprise of donor-acceptor fluorophores that are coupled to each other in close proximity to maintain a quenched state (Figure 4c). The fluorescence emission is activated by enzyme-mediated cleavage that releases the fluorescent probes. Activatable probes can attain high target-to-background signals as these probes in their native injected state are relatively undetectable.

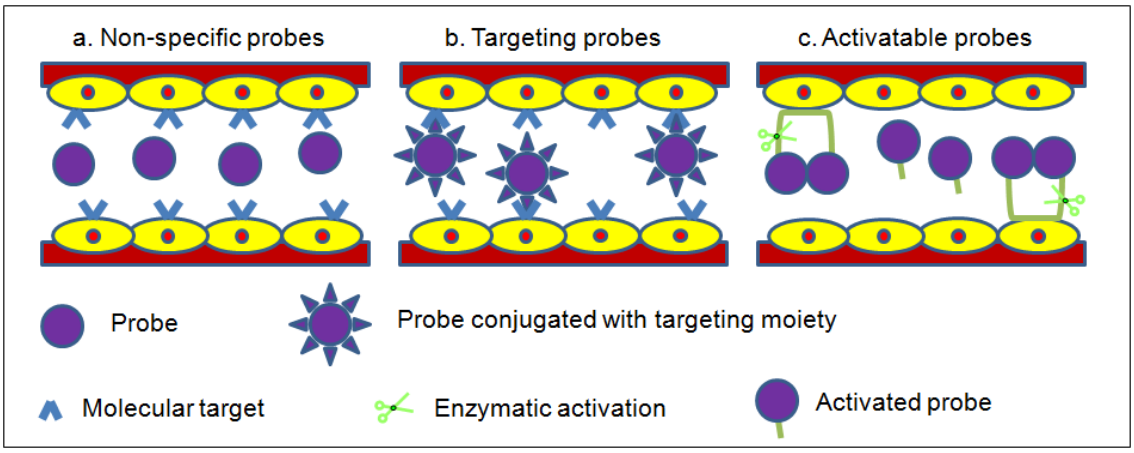

Figure 4. Modes of contrast generation of fluorescent probes. (a) Non-specific compartmental distribution of the probes. (b) Targeted binding of probes via surface ligands to molecular targets. (c) Activatable probes quenched in their native state and become fluorescent by enzyme-mediated cleavage.

2.3 Small Organic Fluorophores

2.3.1 Non-Specific Organic-Dye Probes

The choice of a suitable dye for *in vivo* imaging depends on many factors. The most important consideration would be the molar extinction coefficient and quantum yield of the dye in the NIR region (Gioux *et al.* 2010; Schaafsma *et al.* 2011). Of all the dyes, cyanine makes up the majority of commercial fluorescent probes for *in vivo* applications. Cyanine is a synthetic dye family of the polymethine group with a conjugated chain of odd number of carbon atoms linked between two nitrogen centers (Figure 5) (Mishra *et al.* 2000). Among this class of compounds, carbocyanine dyes with indolic groups are readily available commercially and have also been synthesized in a large variety of analogues. The structure of carbocyanine is formed by reaction of two indolic isomers (either identical or different) linked on each end of a C1, C3 or C5 methine. The absorption and fluorescence emission wavelength is determined both by the chain length of the methine and the side chains attached to the indolic groups. Table 2 shows a series of commercially available carbocyanine dyes emitting in the visible to NIR range. These dyes generally exhibit high molar extinction coefficients but only have moderate fluorescence quantum yields up to 30 %. A prominent representative of the NIR cyanine dye is Indocyanine green (ICG). ICG was first synthesized in the fifties (Licha 2002) and is the only clinically approved dye available commercially. It has been used in optical imaging of changes in blood-brain barrier permeability after thrombus formation in a mouse

model of cerebral venous thrombosis (Kim *et al.* 2005) and liver perfusion in mouse (Liu *et al.* 2011). Clinically, ICG has been used in clinical retinal angiography (Herbort *et al.* 1998), hepatic function testing (Achilefu *et al.* 2002) and imaging of human brain (Liebert *et al.* 2006; Liebert *et al.* 2011). Since ICG binds tightly to plasma proteins and becomes confined to the vascular system, they are widely used for intraoperative assessment of vascular flow in cardiovascular surgery (Raabe *et al.* 2003; Taggart *et al.* 2003; Yamamoto *et al.* 2011). Because of its amphophilicity and a shortage of functional groups available for conjugation, ICG could only function as a non-specific probe for *in vivo* imaging.

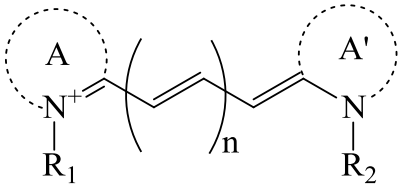

Figure 5. Generalized structure of cyanine dyes. A and A' are two quaternized heteroaromatic bases.

2.3.2 Targeting Organic-Dye Probes

Covalent attachment of targeting moieties such as antibodies, antibody fragments, proteins and peptides to fluorescent dyes can significantly improve the target-to-background signal. The strategy of conjugating antibodies to cyanine dyes were first demonstrated by Folli *et al.* and Ballou *et al.* (Folli *et al.* 1994; Ballou *et al.* 1995) and applied to fluorescence imaging of tumor in mice. Antibodies, however, have found limited utility due to their unfavorable

pharmacokinetics. The typical circulating half-life of antibodies is much shorter than the time required accessing a small tumor with reasonable accumulation, thus rendering effective targeting rare using antibodies (Ballou *et al.* 1997).

To improve the pharmacokinetics of *in vivo* contrast agents, a possible approach is to reduce the conjugate molecular size while still preserving the targeting affinity of the labeled dyes. Neri *et al.* demonstrated this idea by conjugating antibody single chain fragments selected from phage display libraries against an angiogenesis-associated oncofetal fibronectin isoform to cyanine dyes and applied to imaging of angiogenesis in a variety of animal models (Neri *et al.* 1997; Birchler *et al.* 1999). Alternative strategy is also shown in the work by Achilefu *et al.* and Licha *et al.* highlighting the successful application of receptor-specific peptide-dye conjugates for fluorescent imaging of tumors (Becker *et al.* 2001; Bugaj *et al.* 2001; Achilefu *et al.* 2002). As a whole, fluorescent dyes can be readily functionalized to achieve targeting.

2.3.3 Activatable Organic-Dye Probes

The concept of activatable NIR probes was introduced by Weissleder *et al.* for *in vivo* imaging of enzyme activity (Weissleder *et al.* 1999). Enzyme-activatable probes contain either two identical or different fluorophores linked in close proximity to each other by a specific peptide linker. The fluorescence of the probes is essentially undetectable in the quenched state. After enzymatic cleavage, the fluorophores are separated to restore the fluorescence emission. A large number of activatable probes have been documented, among them the

enzyme activation of NIR targeting dyes is mediated mainly by tumor associated proteases, such as cathepsins, caspases and matrix metalloproteinases (Bremer *et al.* 2003; Weissleder *et al.* 2003; Figueiredo *et al.* 2006; Blum *et al.* 2007; Bullok *et al.* 2007; Edgington *et al.* 2009). The ability of activatable fluorescent probes to detect gene expression is particularly useful as a means to diagnose malignant molecular process in the early disease state (Marten *et al.* 2002).

Table 2. Structures and optical characteristics of commercial NIR cyanine dyes.

Dye	Structure	Abs/Em (Becker *et al.*)	Molar extinction coefficient (M^{-1} cm^{-1})	Quantum yield
Indo-Cyanine Green (ICG) (Schaafsma *et al.* 2011)	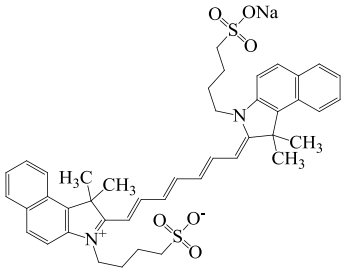	807/822	121,000	0.09
Cy5.5 NHS ester∗	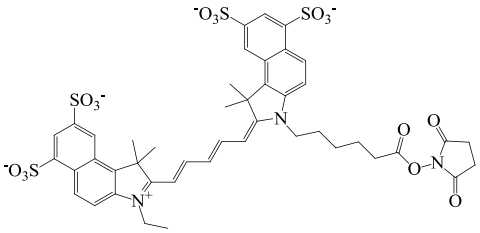	675/694	250,000	0.23
Cy7 NHS ester∗	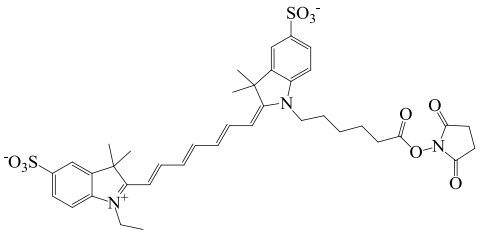	747/774	200,000	0.28
Cy7.5 NHS ester§	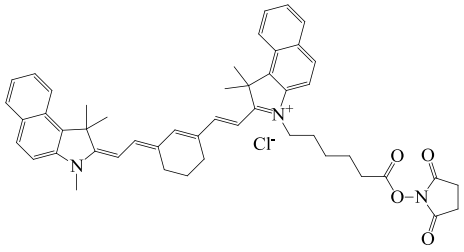	788/808	223,000	N.A.

∗ Information is obtained from supplier GE Healthcare website; § Information is obtained from supplier Lumiprobe website.

2.4 Nanomaterial-Based Fluorescent Probes

Despite the long history of *in vivo* optical imaging, organic dyes have suffered from small Stokes shifts, poor photostability, high plasma protein binding rate, aggregation and background fluorescence in aqueous medium (Escobedo *et al.* 2010). Attention has been increasingly channeled toward nanotechnology to search for new class of more effective probes. Many nanomaterials are already widely used as catalysts, and energy storage and electronic devices (Fischer *et al.* 1997; Lordi *et al.* 2001; Baughman *et al.* 2002; Huynh *et al.* 2002; Porti *et al.* 2003). Their application to the biomedical arena has attracted a similarly enthusiastic following. Interest in the nanomaterials arises from the fact that at nanoscale the properties of materials can be very different from their bulk counterparts. Firstly, nanomaterials when compared to the same mass of material existing in a larger form have a much higher surface area. As such, nanomaterials are more chemically reactive because of the high surface energy. In addition, at nanoscale range, quantum effects begin to dominate the behavior of matter, affecting the optical, electrical and magnetic behavior of materials (Buhro *et al.* 2003; Roduner 2006).

Lately, the integration of nanotechnology with medicine has found many novel applications of nanomaterials. Nanoparticles can be engineered to overcome biological barriers for effective and targeted delivery of drugs, genes, and contrast agents (Bruchez *et al.* 1998). Active moieties such as proteins, peptides and nucleic acids can easily be conjugated to the surface of the nanoparticles for use as non-specific, targeting or activatable nanoprobes. The

following sections are devoted to the recent development of some particulate NIR fluorescent nanoprobes for potential *in vivo* imaging.

2.4.1 Quantum Dots

Fundamentally, quantum dots (QDs) are semiconductor nanocrystals that absorb photons of light and re-emit photons at a different wavelength (Figure 6a) (Michalet *et al.* 2005). Typically, QDs are of ~2–20 nm in diameter depending on the core composition and the surface coating or functionalization. Most of the QDs reported have a core/shell structure (Figure 6b) with the core composed of atoms from periodic groups II–VI (CdSe, CdTe, CdS, PbSe, ZnS and ZnSe), III–V (GaAs, GaN, InP, InAs), and IV–VI (PbS). QDs differ from traditional organic fluorescent dyes and naturally fluorescent proteins in several important aspects. Firstly, QDs are extremely efficient in generating fluorescence, often by an order of magnitude higher than traditional fluorophores. In addition, QDs fluoresce without involving conjugated double-bond systems, thus exhibit greater photostability to enable long-term imaging without the concern of photo-induced deterioration. Another practical advantage of QDs is that their emission spectra are narrow and symmetric, thus minimizing any overlapping of colors in multi-component imaging applications. With the same underlying material, varying the size of the QDs could give rise to different emission peaks, giving QDs unprecedented tunability. This enables the use of a single laser to excite and achieve multicolor emission for multiplexed assays (Bruchez *et al.* 1998; Chan *et al.* 2002; Alivisatos 2004; Medintz *et al.* 2005). These unique properties of QDs

have been increasingly exploited as bioimaging agents (Dubertret *et al.* 2002; Gao *et al.* 2004; Clarke *et al.* 2006; Li *et al.* 2010), theranostic platforms to deliver and track siRNA-based therapy (Derfus *et al.* 2007; Tan *et al.* 2007; Hong *et al.* 2010; Lee *et al.* 2010), nanosensors to study intracellular trafficking and unpacking of DNA nanocomplexes (Chen *et al.* 2006; Clapp *et al.* 2006; Ho *et al.* 2006; Chen *et al.* 2008), and cell lineage-tracing agents to follow the development of stem and progenitor cells *in vivo* developmental (Rieger *et al.* 2005; Slotkin *et al.* 2007).

For *in vivo* imaging, the fluorescent emission wavelengths of the QDs ideally should be around 700–1000 nm, in the NIR region to minimize the endogenous fluorescence and the interference from major absorbers in the body. As presented in Figure 6a, CdTe (Zintchenko *et al.* 2009; Gaponik *et al.* 2010), CdTe/CdSe (Kim *et al.* 2004), CdHgTe/ZnS (Rogach *et al.* 2001; Tsay *et al.* 2004), InAs (Zimmer *et al.* 2006), $InAs_xP_{1-x}$/InP/ZnSe (Kim *et al.* 2005), and PbSe (Dai *et al.* 2009; Jasieniak *et al.* 2011) are the possible QDs that emit in the NIR I region. All these QDs are usually passivated with a layer of ZnS or ZnSe to protect the core from oxidation and to prevent the leaching of toxic heavy metal ions such as Cd, Hg, As and Pb into the surrounding solution. However, with the several reports indicating Cd-containing QDs showing cytotoxicity under extreme conditions (Derfus *et al.* 2004; Kirchner *et al.* 2005; Hardman 2006; Cho *et al.* 2007; Guo *et al.* 2007), there is a rising concern of using them for long term *in vivo* applications. Therefore, attention has been channeled to develop new class of quantum dots comprising of less-toxic elements. Some of these newly

developed NIR QDs include Cu-doped InP/ZnSe (Xie *et al.* 2009), CuInSe (Allen *et al.* 2008; Park *et al.* 2011), and $CuInS_2$/ZnS (Pons *et al.* 2010; Koba *et al.* 2011; Zhang *et al.* 2011).

Among the synthetic routes of QDs, the most commonly used technique is to first generate the core by injecting liquid precursors into nonpolar coordinating organic solvent at a temperature as high as 300 °C and subsequently growing the shell layer of ZnS onto the core (Chan *et al.* 2002; Alivisatos *et al.* 2005; Michalet *et al.* 2005; Smith *et al.* 2006). QDs generated by this method are by default hydrophobic and are unsuitable for use in biological systems. To render them dispersible in aqueous medium, the QDs such as $CuInS_2$/ZnS are transferred into aqueous phase either by ligand exchange with dihydrolipoic acid/polyethylene glycol 1000 (DHLAPEG100) or by encapsulation in phospholipid micelles (Dubertret *et al.* 2002; Uyeda *et al.* 2005; Carion *et al.* 2007; Pons *et al.* 2010). The resulting water-soluble QDs emit at wavelength greater than 700 nm and could achieve good quantum yield of 30%. *In vivo* sentinel lymph node imaging with the $CuInS_2$/ZnS QDs were performed in the work of Pons *et al.* by subcutaneous injection into regional lymph nodes (Thayer *et al.*) of healthy mice. It was observed that the QDs preferentially accumulated at the injection site, in the two regional LNs and to a lesser extent in other organs over a 10-day observation period (Pic *et al.* 2010). The results suggest that the LNs would be more sensitive toward acute QD toxicity. They further compared the inflammatory response of the two regional LNs treated with $CuInS_2$/ZnS and CdTeSe/CdZnS QDs. Histological sections indicated inflammation only occurred

at 10 times dose concentration for cadmium-free QDs than for the Cd-containing counterparts (Figure 6c, d). This study highlights the advantage of cadmium-free QDs for safer NIR *in vivo* imaging.

2.4.2 Colloidal Silicon Quantum Dots

Silicon is one element that is most widely used in the microelectronics industry due to its outstanding performance as an electronic material (Melinon *et al.* 2007; Vogel 2007). Its inherit nontoxic and environmentally friendly characteristic has attracted much attention to develop silicon quantum dots (Si QDs) for biological applications (Erogbogbo *et al.* 2008; Fujioka *et al.* 2008; Park *et al.* 2009; Erogbogbo *et al.* 2010). An important step toward realizing these applications is the fabrication of colloidally and optically stable, water-dispersible Si QDs. Silicon QDs are typically prepared in a two-step process: first by CO_2 laser pyrolysis of silane to generate non-photoluminescent crystalline Si particles with an average diameter of 5 nm (Li *et al.* 2003). Etching with mixture of hydrofluoric acid and nitric acid is then followed to reduce the size and passivate the surface of the particles (Hua *et al.* 2006). Using this method Si QDs with size ranging from 1 to 5 nm and emission from blue to NIR can be obtained.

In 2004, Li *et al.* first demonstrated the potential of Si QDs for biological applications. They grafted water-soluble polyacrylic acid Si QDs to label Chinese hamster ovary (CHO) cells for *in vitro* imaging (Li *et al.* 2004). In the recent work by Park *et al.* they delivered Si QDs loaded with anti-cancer drug doxorubicin D-LPSiNPs into BALB/c mice and monitored both accumulation and degradation *in*

vivo (Figure 7) (Park *et al.* 2009). Si QDs are exhibiting the attractive attributes to be an effective and biocompatible nanomaterials system for theranostic purpose; they will undoubtedly see intense effort for further improvement and innovative applications.

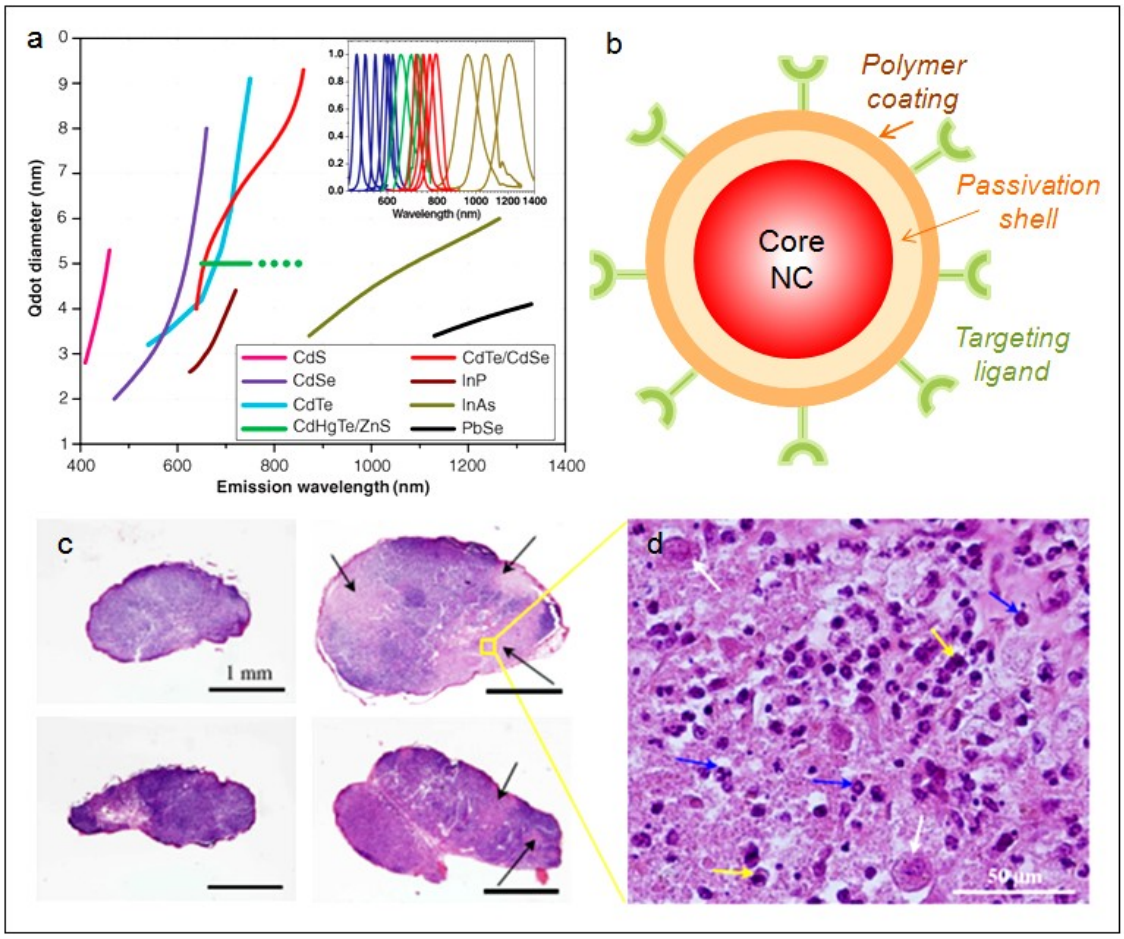

Figure 6. (a) Emission maxima and sizes of quantum dots of different composition. (Reprinted with permission from (Michalet *et al.* 2005), copyright 2005 Science). (b) Typical structure of a quantum dots (QD) for biomedical applications. The core of the QD is passivated by a second semiconductor material. The core/shell QD is made hydrophilic and biocompatible by a polymer coating. The surface of the QD is conjugated with a targeting ligand for specific recognition and interaction with biological molecules. (c) Histology sections of lymph node (Thayer *et al.*) 10 days post-injection: control regional auxiliary LN (RALN) (upper left), control right lateral thoracic LN (RLTLN) (lower left), RALN injected with QDs (upper right), and RLTLN injected with QDs (lower right). The lighter regions indicated with black arrows are the sites of inflammation. (d) Magnification of an inflammation area from RALN. There were many polynuclears observed but only some were indicated with blue arrows. Histiocytes (yellow arrows) and also vacuoles of digestion were also observed. (Reprinted with permission from (Pic *et al.* 2010), copyright 2009 Academy of Molecular Imaging).

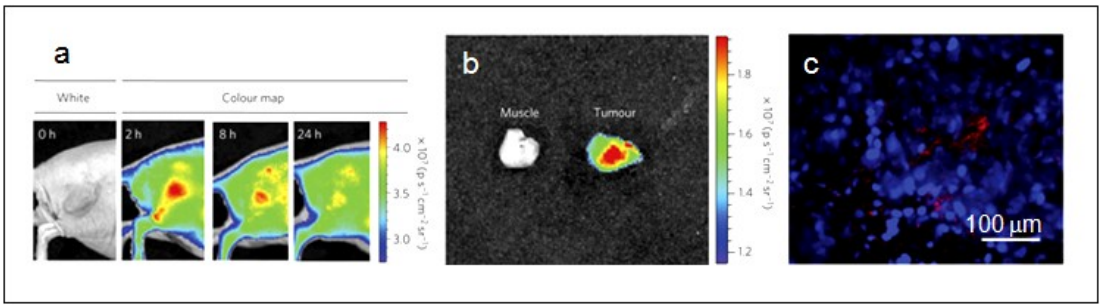

Figure 7. (a) Representative fluorescence images of a mouse with an MDA-MB-435 tumor. The mouse was imaged using a 615–665 nm excitation filter and an 810–875 nm emission filter at the indicated time post-intravenous injection of D-LPSiNPs (20 mg/kg). A strong signal from D-LPSiNPs is observed in the tumor, indicating significant passive accumulation in the tumor by the enhanced permeability and retention (Neri *et al.*) effect. (b) *Ex vivo* fluorescence images of the tumor from the mouse used in (a). (c) Fluorescence images of a tumor slice from the mouse in (a). Red and blue indicate D-LPSiNPs and cell nuclei (DAPI stain). (Reprinted with permission from (Park *et al.* 2009), copyright 2009 Macmillan)

2.4.3 Gold Nanoclusters

Fluorescence of noble metal nanoclusters (NCs) of gold and silver comprising of several to tens of atoms have drawn great attention in the past decade because of their remarkable optical properties (Zheng *et al.* 2007; Devadas *et al.* 2010; Wu *et al.* 2010; Guo *et al.* 2011; Selvam *et al.* 2011; Sun *et al.* 2011; Yuan *et al.* 2011). Because of their minuscule size, high chemical stability and biocompatibility, NCs are increasingly being exploited for sensing (Huang *et al.* 2009; Shang *et al.* 2009; Wei *et al.* 2010), biolabeling (Yu *et al.* 2007; Richards *et al.* 2008) and bioimaging (Yu *et al.* 2009). Typically, the size of NCs is less than 2 nm and their properties are governed by their subnanometer dimensions. Their size regime is intermediate of atomic and nanoparticles in which they no longer have plasmon resonance and Mie's theory is non-applicable (Zheng *et al.* 2007). In fact, the size of noble metal NCs is comparable to the Fermi wavelength of the conduction electrons, leading to molecule-like features such as discrete size-dependent electronic transitions, fluorescence and charging properties.

Multitudes of strategies have been developed for the synthesis of gold nanoclusters (AuNCs). One of which is chemical reduction of Au precursors in the presence of thiol stabilizers to afford AuNCs that fluoresce in the blue to near-IR regions (Negishi *et al.* 2004; Negishi *et al.* 2005; Wang *et al.* 2005; Negishi *et al.* 2007; Shichibu *et al.* 2007). However these NCs exhibit low quantum yields (QY) (0.001–0.1%). AuNCs can also be prepared via template-

assisted synthesis within the cavities of dendrimers (Zheng *et al.* 2007) with greater than 10% QY at the expense of fairly long reaction time of ~2 days along with the production of large nanoparticles (NPs) as byproduct. Another commonly used technique to prepare AuNCs is by ligand-induced core etching of metal NPs to yield blue-emission NCs (Duan *et al.* 2007). Fine-tuning of the core etching method led Lin *et al.* to generate NIR AuNCs by first producing 6-nm diameter gold nanoparticles core stabilized with dihydrogenlipoic acid (DHLA) (AuNC@DHLA) (Jana *et al.* 2003; Lin *et al.* 2009). Conjugation of AuNC@DHLA with biomolecules can easily be achieved with the carboxyl group on DHLA via carbodiimide chemistry. Polyethylene glycol (PEG, 5 kDa), PEG-biotin and avidin have been attached in this manner. The shortcoming of these NCs is the low quantum yield of 1–3%. Nevertheless, the authors demonstrated the specific labeling capability of the AuNCs toward fixed human hepatoma cells ($HepG_2$) and also the non-specific uptake of the AuNCs by human aortic endothelial cells. The results make obvious that these AuNCs are relatively nontoxic.

With increasing interest in applying NIR fluorescent probes for bioimaging, effort has been devoted to developing biocompatible AuNCs via aqueous synthetic routes with biological molecules (Bao *et al.* 2010). Xie *et al.* (Xie *et al.* 2009) has developed an innovative method by exploiting the reducing capability of bovine serum albumin (BSA) to prepare AuNCs consisted of 25 gold atoms with red emission (Xie *et al.* 2009). The synthesis is similar to the biomineralization activities of organisms. Once added to aqueous BSA solution the Au ions were sequestered and entrapped within the protein molecules. The

reduction ability of BSA was activated when the pH of the reaction was adjusted to ~12 and the ions were progressive reduced to AuNCs *in situ* (Figure 8a). Additional reductant, such as $NaBH_4$ would be required to yield AuNCs that emit at 683 nm. The quantum yield of the NIR AuNCs produced by this method was also low (0.1%). Despite that, Wu *et al.* demonstrated the applicability of these AuNCs for *in vivo* tumor fluorescence imaging using MSD-MB-45 and HeLa tumor xenograft models. They attributed the high accumulation of the NIR AuNCs in the tumor areas to the enhanced permeability and retention (Neri *et al.*) effects (Figure 8b) (Wu *et al.* 2010).

2.5 Carbon Materials

2.5.1 Single-Walled Carbon Nanotubes

Carbon nanotubes (CNTs) represent another class of nanomaterials attract intense interest since their discovery in 1991 (Iijima 1991). CNTs are cylindrical tubes of sp^2 carbon with superior optical, electrical, and mechanical properties, thus have wide range of potential applications as nanoelectronics devices and engineered composite materials (Fischer *et al.* 1997; Baughman *et al.* 2002). In addition, CNTs have been extensively explored as intracellular delivery vehicles for drugs, proteins and genes in cancer therapy (Feng *et al.* 2011; Liu *et al.* 2011).

CNTs are categorized as single-walled nanotubes (SWNTs) and multi-walled nanotubes (MWNTs). So far, only SWNTs have been reported to possess high emission in the NIR II region, making them suitable for deep-tissue in vivo

imaging (Welsher *et al.* 2009). In general, SWNTs are most commonly synthesized by chemical vapor deposition that involves the heating of an alumina substrate with a layer of transition-metal catalytic nanoparticles, which serve as seeds to nucleate the growth of the nanotubes in a furnace with a stream of hydrocarbon gas flowing through the tube reactor (Dai 2002). SWNTs synthesized by this method have vast possibilities in the type of carbon tube molecules, giving rise to variation in band gaps ranging from ~10 meV to ~0.5 eV (Dai 2002).

Welsher *et al.* suggested that the biggest obstacle in realizing the potential of SWNTs as NIR II probes is producing SWNTs with high quantum efficiency and good biocompatibility (Welsher *et al.* 2009). To overcome this issue, the authors came up with a strategy of first debundling and solubilizing the hydrophobic, pristine SWNTs in sodium cholate by sonification, followed by surfactant exchange to displace the sodium cholate with pegylated phospholipid (DSPE-mPEG). The resulting water-soluble SWNTs exhibit several emission peaks across the NIR II region when excited at 808 nm (Figure 9). When delivered into athymic nude mice via tail-vein injection, the systemic circulation and biodistribution of the SWNTs can be followed for over two minutes (Figure 9) (Welsher *et al.* 2011). This work shows the advantages of fluorescence imaging in the NIR II region and their potential impact in advancing nanomedicine.

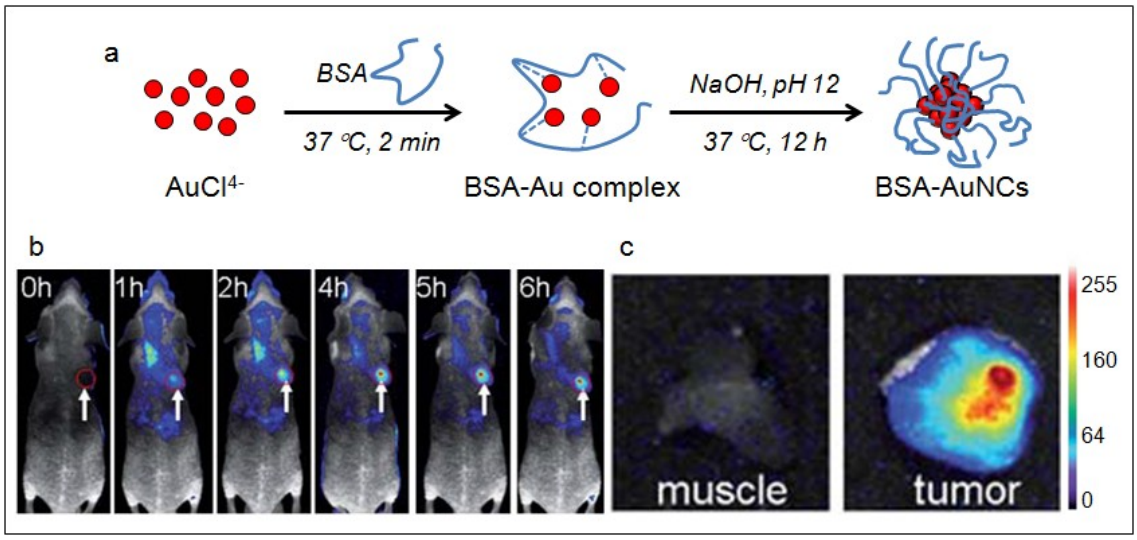

Figure 8. (a) Schematic of the formation of AuNCs in BSA solution. (b) Fluorescence images of mice with a MDS-MB-45 tumor. Strong signal from AuNCs was observed in the tumor (red circle), indicating significant passive accumulation in the tumor by the EPR effect. White arrows indicate tumor site. (c) *Ex vivo* fluorescence image of the muscle and tumor tissue around the tumor from the mice used in b. (Reprinted with permission from (Wu *et al.* 2010), copyright 2010 The Royal Society of Chemistry).

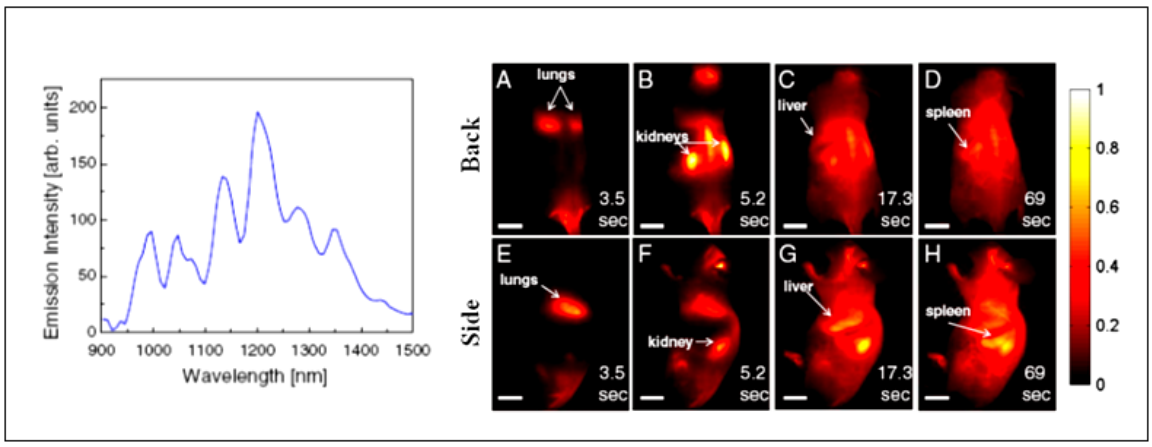

Figure 9. *Left panel*: Fluorescence spectrum of DSPE-mPEG functionalized SWNTs excited at 808 nm, showing several emission peaks in the NIR II ranging from 1000–1400 nm. *Right panel*: Frames from video imaging of mice injected with SWNTs. At 3.5 s (**A** and **E**) post tail-vein injection, the lungs are the dominant feature, corresponding to flow of oxygen-poor, SWNT-rich blood to the lungs. At 5.3 s (**B** and **F**), the SWNT-rich blood flows through the highly vascularized kidney followed by the liver at 17.3 s (**C** and **G**) and the spleen at 69 s (**D** and **H**). (Reprinted with permission from (Welsher *et al.* 2011), copyright 2011 PNAS).

2.6 Conclusion and Outlook

The potential of NIR fluorescent nanoprobes for *in vivo* application is unlimited. The drawbacks of organic dyes such as poor photostability, undesired aggregation and fluorescence in aqueous solution can be resolved by innovative NIR nanoprobe designs. In particular the versatile, nanomaterials-based NIR fluorescent probes offer ample opportunity to optimize their optical and targeting properties. Among all nanomaterial-based fluorescent probes, Si QDs is the only system that can be directly loaded with drugs and biodegraded into silicic acid that can be excreted efficiently through renal clearance. Like other nanomaterial-based fluorescent probes, improvement of their quantum efficiency, however, will still require significant effort. Robust and environmentally friendly synthetic routes that can produce these nanomaterials-based NIR nanoprobes with uniform size and colloidal stability represent other significant challenges. The widespread application of NIR fluorescent nanoprobes awaits demonstration of their long term biocompatibility, *in vivo* targeting efficacy as well as parallel development of advanced optical instrumentation for deep-tissue imaging capability. Nevertheless, their role in advancing the field of nanomedicine will undoubtedly be essential.

Chapter 3

Synthesis and Characterizations of Water Soluble, Silver-Doped Zinc Selenide Quantum Dots

3.1 Background

Nanomaterials are increasingly being used in the biomedical field because they have size comparable to biological molecules (Figure 10). They can effectively interact with biomolecules either on the surface of cells or within cells, thus can be used to interrogate molecular events. Nanomaterials can be engineered to incorporate multifunctionalities into a single platform thereby achieving simultaneous treatment and diagnosis. In particular, nanoparticles have been used in drug delivery for more than two decades owing to their stable and large payload delivery, multiplexing capacity, precise targeting capability, and tunable biodistribution profiles (Jokerst *et al.* 2011). Recently, they are gradually more popular for imaging purposes due to their unique way of interaction with electromagnetic waves (Wagner *et al.* 2006). Some of the newly developed nanoparticles for imaging include gold nanoclusters and colloidal silicon nanoparticles. The advantages of gold nanoclusters are its ultrasmall size (< 2 nm) and biocompatibility, but its quantum yield has yet to go beyond 0.1 %. Colloidal silicon nanoparticles are biocompatible and biodegrable with reasonable quantum yield of ~10.2 %. However, it is unsuitable for *in vivo* imaging due to that its absorption range falls in the visible range, a region where tissues and body fluids readily absorb and scatter photons and interferes with

signal collection and processing (Quek *et. al*. 2012). To date, the most studied nanoparticles for bioimaging is quantum dots (QDs), and the overall goal of this research is to explore new strategy to develop novel hydrophilic QDs for biomedical research applications.

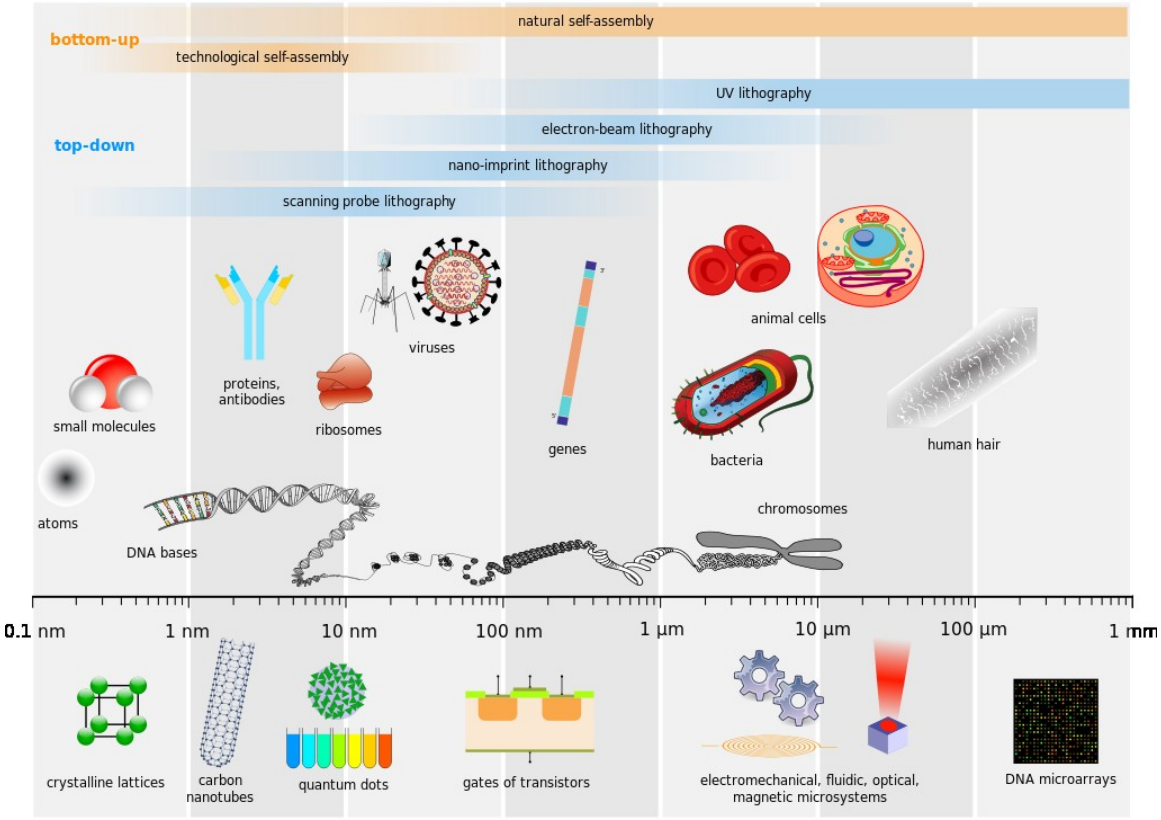

Figure 10. A comparison of the scales of biological entities and nanomaterials. (http://en.wikipedia.org/wiki/Nanoscopic_scale#mediaviewer/File:Biological_and_technological_scales_compared-en.svg)

Quantum dots (QDs) are widely exploited in the optoelectronic industries as superior nanomaterials for use as light emitting diode, data storage and quantum information processing (Jeon *et al.* 1991; Hong *et al.* 2001). Lately, as a result of the success in making water-soluble QDs along with the integration of

nanotechnology with biology and medicine, quantum dots have emerged as potential candidates for several important biological applications.

Fundamentally, QDs are luminescent semiconductor nanocrystals that absorb photons of light and re-emit photons at a different wavelength QDs (Figure 11). Typically, QDs are of ~2-20 nm in diameter depending on the atoms it was made up of and the surface coating or functional groups added. Most of the QDs reported have a core/shell conjugate structure with core composed of atoms from periodic groups II-VI (CdSe, CdTe, CdS, PbSe, ZnS and ZnSe), III-V (GaSz, GaN, InP, InAs), and IV-VI (PbS). QDs have several important differences as compared to traditional organic fluorescent dyes and naturally fluorescent proteins. Firstly, QDs are extremely efficient for generating fluorescence which could often be many times higher than traditional fluorophore. In addition, QDs fluoresce without involving conjugated double-bond systems, thus exhibit greater photostability and enabling long-term imaging experiments to be carried out without the fear of any photo-induced deterioration. Another practical advantage of QDs is that, the emission from QDs is precise, narrow and symmetric, as so, the overlapping other colors is minimal. With the same underlying material, varying the size of the QDs could give rise to different emission peaks, giving QDs unprecedented tunability, thus enable the use of a single laser to excite to achieve multicolor emission and multiplexed assays to be achieved simultaneously (Chan *et al.* 1998; Bruchez *et. al*. 1998; Chan *et. el*. 2002). With all these unique properties, QDs show promising biological applications as, bioimaging agents (Clarke *et al.* 2006), siRNA (Derfus *et al.*

2007), FRET (Clapp *et al.* 2006), cell lineage tracing agents (Rieger *et al.* 2005, Slotkin *et. al*. 2007).

To date, QDs used in biological applications mostly contain cadmium as core material. They are synthesized via conventional technique involving the injection of precursors into reaction flasks containing boiling, nonpolar coordination organic solvents, such as trioctylphosphine (Marten *et al.* 2002), trioctylphosphine oxide, and hexadecylamine (Smith *et al.* 2006). At elevated temperature, the precursors decompose to form monomers that allow nucleation to occur and subsequently leading to the generation hydrophobic, nearly monodisperse nanocrystals with high fluorescence emission intensity. For biological applications, additional surface modification steps are required to render the solubility of the QDs in aqueous media which typically led to an alteration of optical properties of the nanocrystals.

Over the past decade several major advances have been achieved in development of QDs in aqueous environments due to increasing recognition of the potential of QDs for biomedical applications (Gaponik *et al.* 2010). Thus far, ZnSe (Zheng *et. al*. 2007; Xing *et. al*. 2008), CdS, CdSe, CdTe (Zheng *et al.* 2007), and HgTe (Rogach *et al.* 2001) have been successfully prepared in aqueous solution stabilized with thiol ligands. However, the issue of possible leakage of toxic heavy metal ions *in vivo* is at large a major concern that impedes the wide application of QDs. In this context, we proposed to develop an aqueous method to prepare heavy metal-free quantum dots intended for biological applications. We describe here the synthesis of silver-doped zinc selenide

quantum dots in water with L-glutathione as stabilizing ligand. The physical and optical characteristics of the as-synthesized QDs are also evaluated.

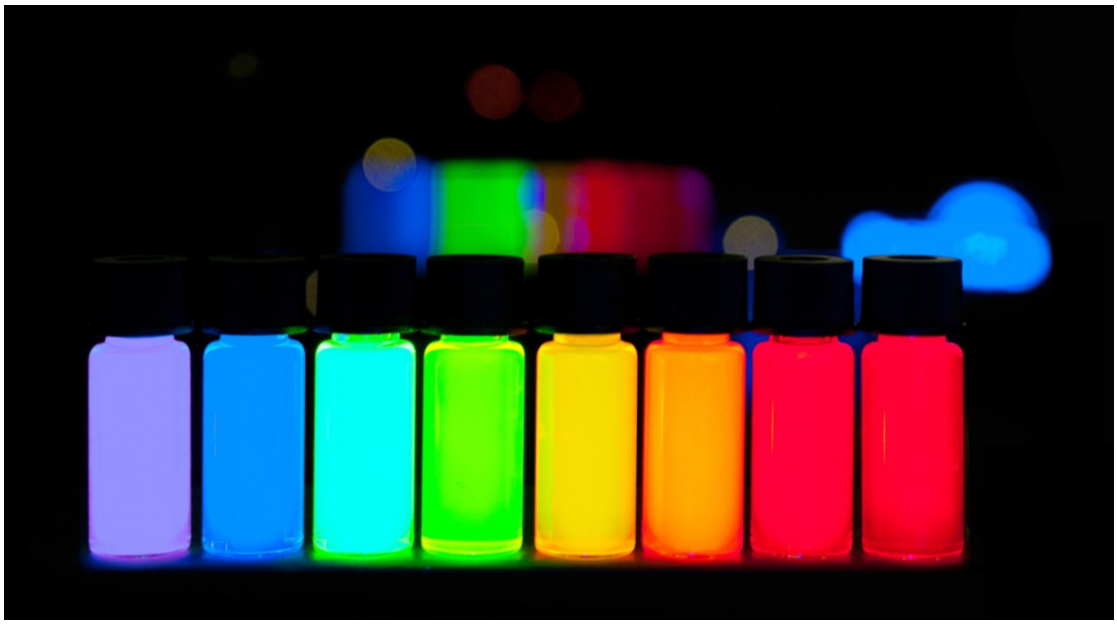

Figure 11. Photos of a series of ZnCdSeS alloyed Quantum Dots with gradually stepping emission from violet to deep red.
(http://www.plasmachem.com/shop/en/226-zncdses-alloyed-quantum-dots)

3.2 Experimental Details

3.2.1 Materials

Zinc acetate, copper (II) acetate, silver acetate, selenium powder (~100 mesh), L-glutathione reduced, citric acid trisodium salt, DL-cysteine, and sodium borohydride were purchased from Sigma-Aldrich (St. Louis, MO, USA). Gold (III) acetate was acquired from Alfa Aesar. Solvents used for synthesis and spectroscopic measurements were purchased from J. T. Baker and EMD Chemicals. All chemicals were used without further purification.

3.2.2 Spectroscopic and Microscopic Measurements

Ultraviolet-visible spectra were measured by a double monochromator Shimadzu UV2501PC spectrophotometer equipped with a 50W halogen lamp and a D_2 lamp and using a 1.0 cm path length quartz cell. Spectra were presented in terms of λ_{max} in nm, the wavelength of the absorption peak, and absorbance, A, as defined by the following equation:

$$A = log_{10}\left(\frac{I_0}{I}\right)$$

where I_0 is the intensity of the radiant energy striking the sample, and I is the intensity of the radiation emerging from the sample.

A more convenient expression of absorption intensity is that derived from the Lambert-Beer law as described:

$$A = \varepsilon cl$$

where ε = molar absorptivity of the sample,

c = concentration of solute expressed in moles per litre,

l = path length through the sample.

Fluorescence spectra were measured on Cary Eclipse Fluorescence Spectrophotometer equipped with a xenon flash lamp excited at 420 nm and 5 nm bandpass. The fluorescence quantum yield (Φ_x) is given by the ratio of photons absorbed to photons emitted through fluorescence. In order to determine the quantum yield, QD515 was dissolved in 0.1 M sodium acetate buffer (pH 5.2) while QD625 and QD710 were dissolved in phosphate buffered saline (PBS) in a

series of concentrations. The uv-vis absorbance readings were recorded using a 10 mm fluorescence cuvette. Absorbance readings of QD515 were taken at 420 nm, QD625 and QD710 were monitored at 540 nm. The emission spectra of QD515 excited at 420 nm, QD625 and QD710 excited at 540 nm were recorded on the spectrofluorometer to generate a plot of integrated fluorescence intensity *vs* absorbance with intercept at 0. For this study, fluorescein dissolved in 0.1 M NaOH was used as know standard for evaluation of QD515, rhodamine 101 in 0.01 % HCl/ethanol was used for QD625 and QD710 testing. The quantum yield was calculated based on the equation:

$$\Phi_x = \Phi_{ST}\left(\frac{Grad_x}{Grad_{ST}}\right)\left(\frac{n_x^2}{n_{ST}^2}\right)$$

where the subscripts ST and X denote standard and test respectively, Φ is the fluorescence quantum yield, *Grad* the gradient from the plot of integrated fluorescence intensity *vs* absorbance, and n the refractive index of the solvent.

The X-ray diffraction pattern was collected on a XDIF1 X-Ray Diffractometer Philips X'Pert PRO MRD HR X-Ray Diffraction System with a Cu X-ray source operated at 40 kV and 20 mA. Nanocrystal powders were smeared onto silicon wafers for analysis.

The particle size of the water-soluble silver-doped ZnSe nanocrystals were characterized using transmission electron microscopy (TEM, FEI Tecnai G² Twin). Samples for TEM were prepared by putting a drop of suspension on carbon/formvar coated, 300-mesh copper grid.

Zeta potential measurement was recorded on a Malvern Nano ZS Zetasizer.

3.2.3 Synthesis of Silver-Doped Zinc Selenide Quantum Dots

On the whole, all reactions were performed under argon gas. Sodium hydroselenide (NaHSe) was freshly prepared based on a previous method (Klayman *et al.* 1973) and was swiftly added to a reaction flask containing a mixture of zinc acetate (1 M, $ZnOAc_2$) and silver acetate (0.01 M, AgOAc) with L-glutathione (GSH) as stabilizer. The pH values of the reactions were adjusted to with 10 M NaOH. The molar ratio of $ZnOAc_2$:Se: GSH used in the experiments was kept at 8:1:15-21 while $ZnOAc_2$:AgOAc was at 50-100:1. The reactions were performed at room temperature. The final emission of the QDs was controlled by varying the growth time and pH. After the reaction, 2-propanol was added to the QDs until turbidity occurred; the nanocrystals were isolated by centrifugation and washing of the product was repeated another two times. The pelletized nanocrystals was dissolved in Millipore water and purified by ultrafiltration with 3 K MWCO membrane. The purified product was freeze dried and stored under argon atmosphere at 4 °C.

3.3 Results and Discussion

3.3.1 Synthesis of water soluble, sliver-doped ZnSe (ZnSeAg) QDs

A series of ligand (cysteine, citric acid sodium salt, and L-glutathione) was tested to determine if stabilized ZnSe QDs could be obtained. The reaction was performed at reflux temperature and the results are summarized in Appendix A. The results clearly indicated that thiol functional group has an important role in the synthesis. During the reaction the thiol proton will cleave and bind to the surface of the QDs thereby stabilizing the products. Citric acid sodium salt does not contain thiol functional group thus no QDs could be formed from the reaction. However, with cysteine as stabilizer, the QDs formed eventually precipitated at the end of reaction due to aggregation. We have identified that GSH is the appropriate stabilizer for the subsequent reactions.

We next screened through the acetate salt of copper, silver and gold to verify which dopant has the capability to tune the emission into the near-infrared range. Our results in Appendix B indicate that using copper (II) acetate as dopant, we could only tune the emission to 438 nm, which is non ideal for bioimaging. We did not obtain any QDs with gold (III) acetate as dopant probably due to both ZnSe and gold nanoparticles were formed at the same time and bound to each other, leading to quenching of the fluorescent signal of the products. With silver acetate as dopant, the as-synthesized QDs could be tuned to have near-infrared emission. However, to achieve controllable growth rates, the reactions with silver acetate as dopant have to be performed at room temperature.

QDs have attracted significant attention for several important biomedical applications. While most QDs were prepared through organometallic synthetic route, there is a rising interest to develop aqueous-based synthesis involving milder reagents along with biomolecules. Glutathione (GSH) is a tripeptide comprising a carboxylate and amino groups in a single molecule. GSH exists in most organisms and has widely being used for detoxification of heavy metals (Singhal *et al.* 1987). In our design, we have selected to use L-GSH as the stabilizing ligands to allow us to further introduce bioactive moieties that would recognize specific biological structure. The synthesis of silver-doped QDs was based on the reaction of zinc acetate and sodium hydroselenide. Since the emission of ZnSe is located in the ultraviolet range, metal impurities are often added as dopant into ZnSe nanocrystals to alter the emission range (Erwin *et al.* 2005; Norris *et al.* 2008). In the synthesis we have incorporated silver acetate that resulted in a red shift in the emission peaks that is in agreement with the report by Mocatta, *et. al*. (Mocatta *et al.* 2011). The influence of parameters, such as concentrations of precursors and pH of reaction were systematically investigated and the results are summarized in Appendix C-H.

The schematic for the synthesis is as depicted in Figure 12. The growth of the ZnSeAg nanocrystals in aqueous solution was controlled by the Ostwald ripening process, whereby monomers released by the dissolution of smaller particles are consumed by the larger particles. Some studies on cadmium-based nanocrystals have shown that at lower pH, Cd^{2+}-thiol complexes tightly on the surface of the nanocrystals thus inhibiting the growth (Swayambunathan *et al.*

1990; Gao *et al.* 1998). Similarly in our system, when the pH of the reaction decreased from 7 to 5, the growth rate of the nanocrystals decreased remarkably (Figure 13).

3.3.2 Physical characterizations of QDs

Figure 14a shows an image of the ZnSeAg QDs under the illumination of a 365 nm ultraviolet light, the corresponding absorption and emission spectra are depicted in Figure 14b. Representative compositions are presented in Table 3; under optimal conditions, the as-synthesized GSH-capped ZnSeAg QDs with broad absorption (up to ~ 700 nm) and emission ranging from 515-710 nm could be synthesized within 15-160 min.

TEM analysis of sample QD710 indicated the diameter of the QDs is ~2-8 nm (Figure 15a). At such a low feed dopant concentration, it was not possible to distinguish the metal regions in the micrograph, indicating that the Ag atoms are dispersed in the nanocrystals. Further evidence is shown in the x-ray diffraction (Figure 15b) where no fingerprints of Ag domain. The XRD result indicated that the as-synthesized nanocrystals belonged to the cubic zinc blende structure. The peak positions of ZnSeAg were located between positions for pure cubic ZnSe and pure cubic ZnS. This result suggested that the surface Zn^{2+}-GSH layer might have slightly decomposed, leading to the incorporation of sulfur into the nanocrystals (Li *et al.* 2005). In addition, some broadening of the peaks is observed that can be due to a small degree of structural disorder in the naocrystals. Zeta potential analysis (Figure 15c) showed that QD710 has an average -35.9 mV. We account this observation to ionization of the two carboxyl

group on GSH at pH 5 and presented an overall negative surface charge on the QDs.

From EDX analysis (Figure 16 and Table 4), we conclude that with we can use as low as 0.03 mol % of silver dopant to tune the emission of the QDs to 710 nm. Figure 17 and 18 are plots of fluorescence intensities vs absorbance of fluorescein, QD510, rhodamine 101, QD625 and QD710 respectively. The gradients of the plots were obtained to evaluate the quantum yield of the silver-doped ZnSe samples. The quantum yield of QD515, QD625 and QD710 are found to be 20-47 % and is summarized in Table 5.

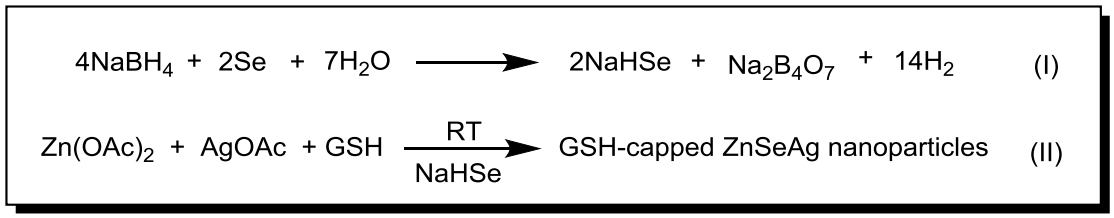

Figure 12. Synthesis of ZnSeAg QDs via green chemistry route.

Table 3. Representative synthesis compositions for obtaining quantum dots with emission as indicated in table.

Sample	E_{max} (nm)	$Zn(OAc)_2$ (mmol)	AgOAc (mmol)	GSH (mmol)	NaHSe (mmol)	pH	Reaction time (min)
QD515	**515***	0.1	0.001	0.122	0.012	8	15
QD625	**625**	0.1	0.001	0.252	0.012	5	15
QD710	**710**	0.1	0.001	0.122	0.012	7	160

** Disperse the QDs in water or PBS and allow the Ag^+ to leach out (~ 4 weeks).*

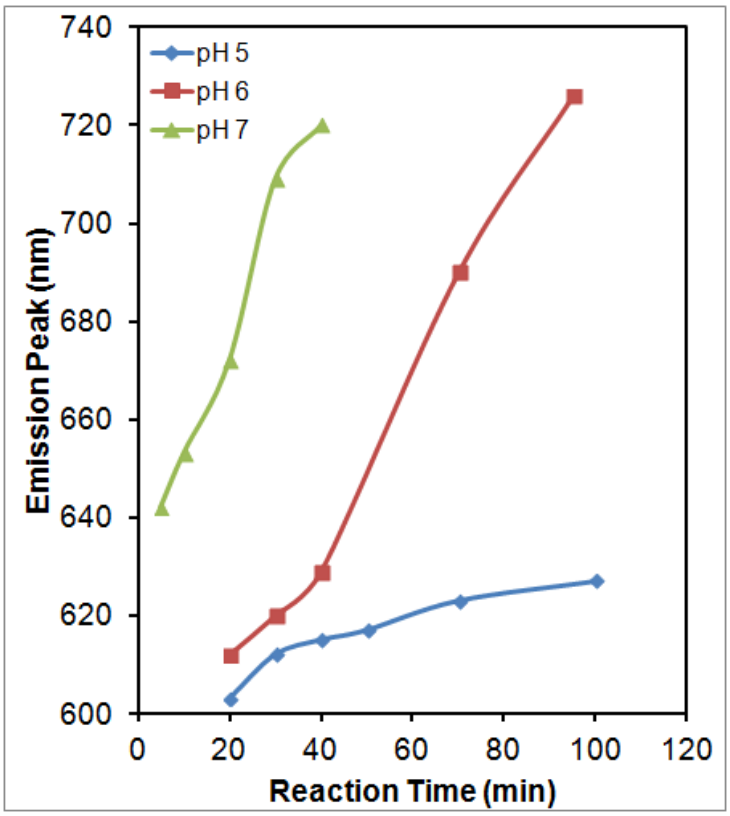

Figure 13. Growth rate as a function of the emission peak for ZnSeAg at different pH.

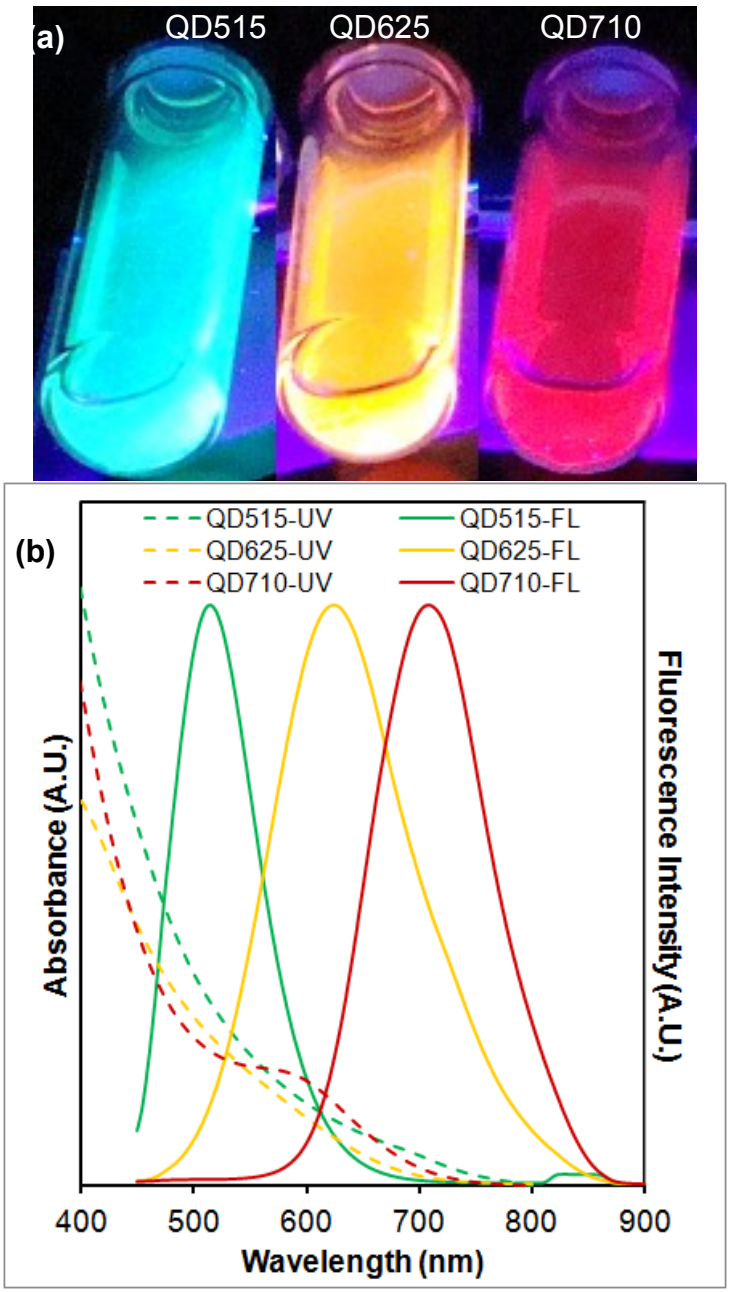

Figure 14. (a) Photographs of QD510, QD625 and QD710. (b) Absorption spectra (dotted lines) and fluorescence spectra (solid lines) of ZnSeAg QDs with three different colors.

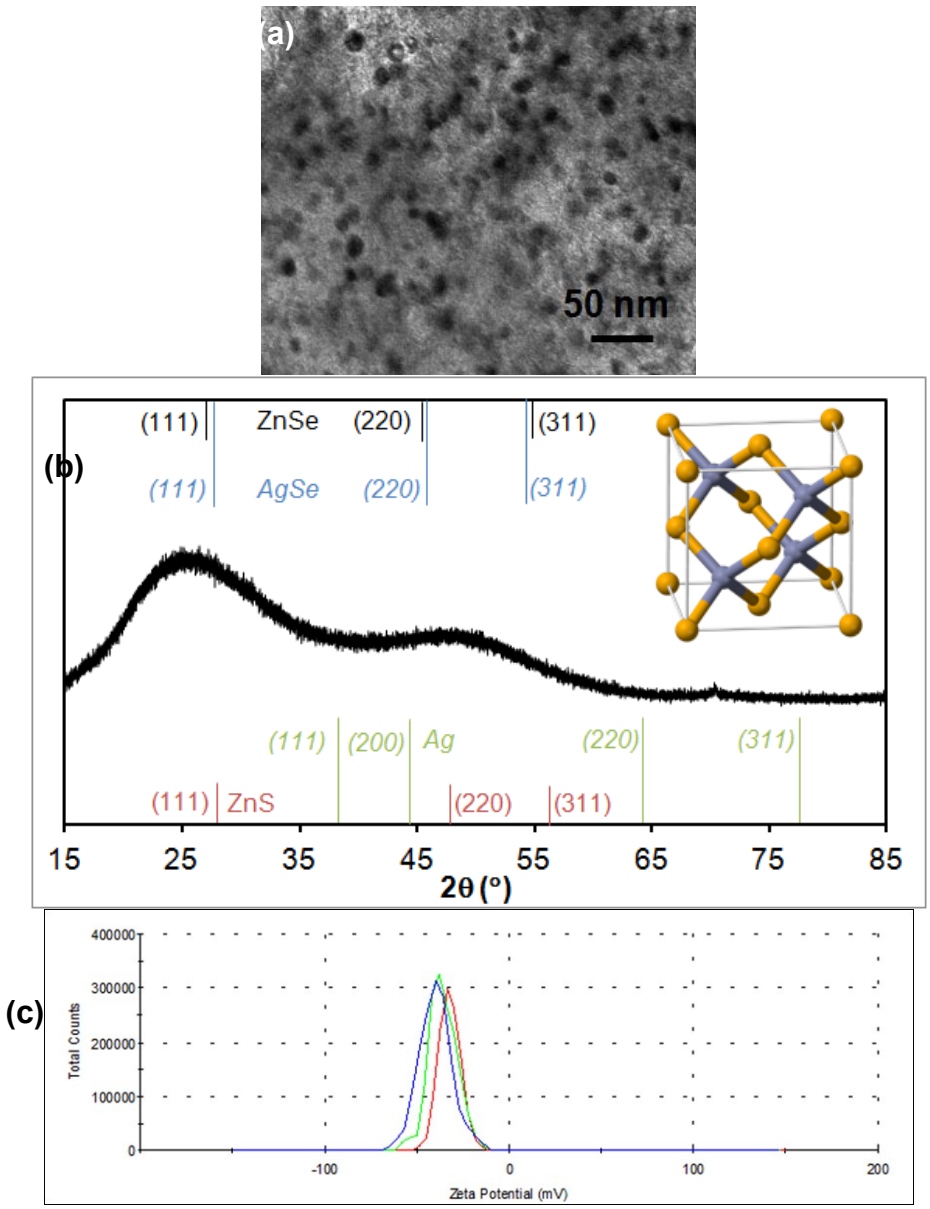

Figure 15. (a) TEM image of QD710. (b) Powder x-ray diffraction of QD710 indicated a zinc blende crystal structure, insert is a zinc blende unit cell (http://upload.wikimedia.org/wikipedia/commons/e/e8/Zinc-selenide-unit-cell-3D-balls.png). (c) Zeta potential analysis of QD710.

Table 4. Elemental composition of QD710 from EDX

Mole Ratio	Zn	Se	S	Ag
Feed Ratio	2.5	1	2.5	0.10
Observed Ratio	2.27	1	2.39	0.03

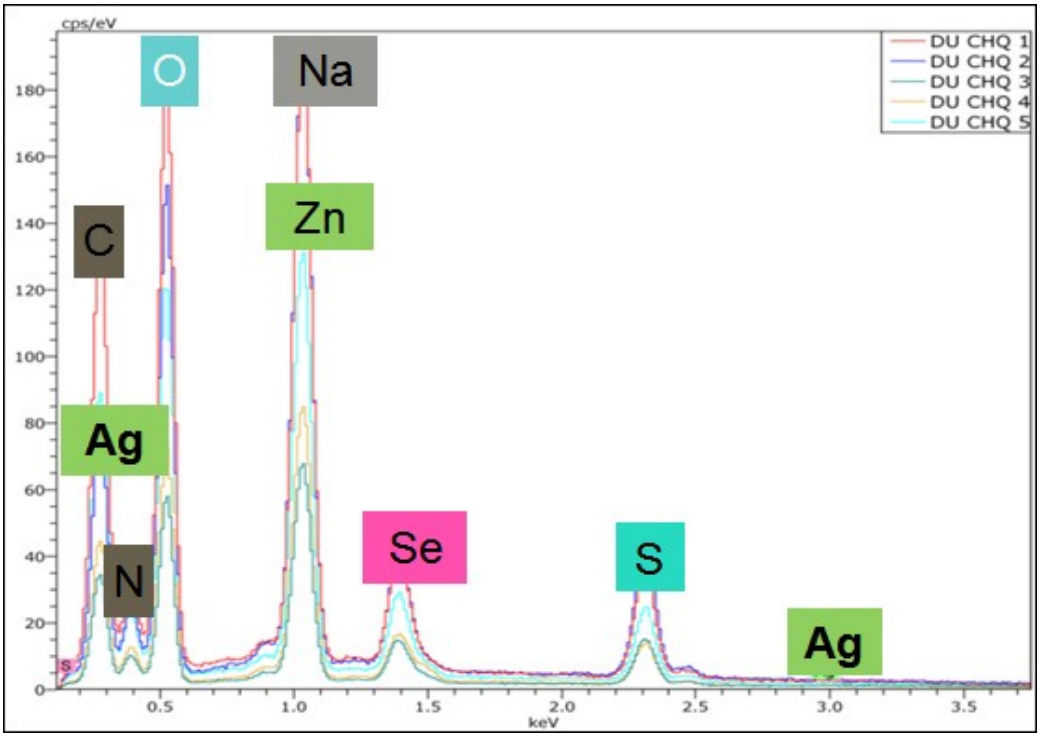

Figure 16. Energy-dispersive x-ray (EDX) analysis of QD710.

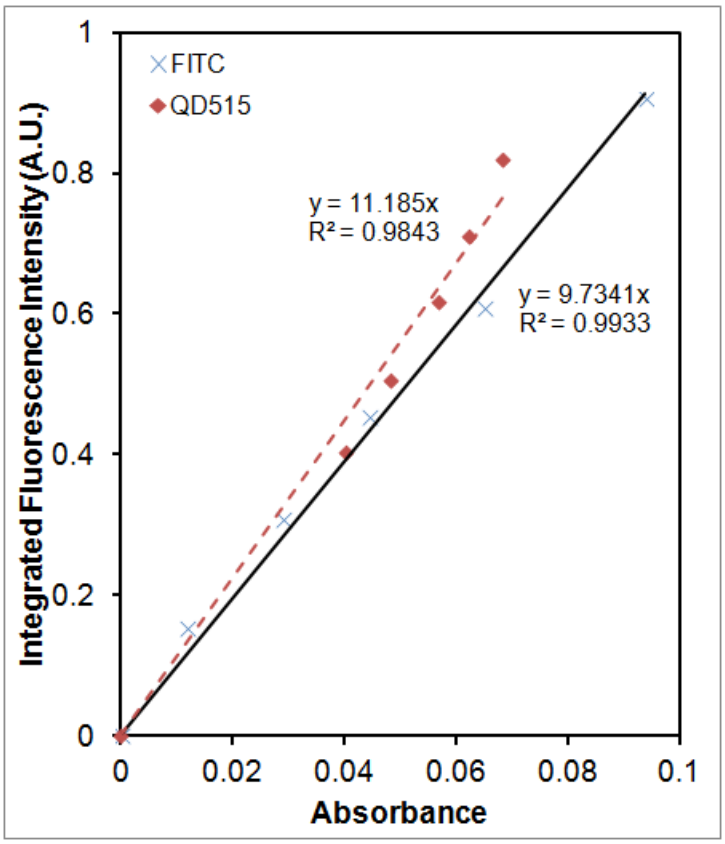

Figure 17. Plots of fluorescence intensities vs absorbance of fluorescein and QD510.

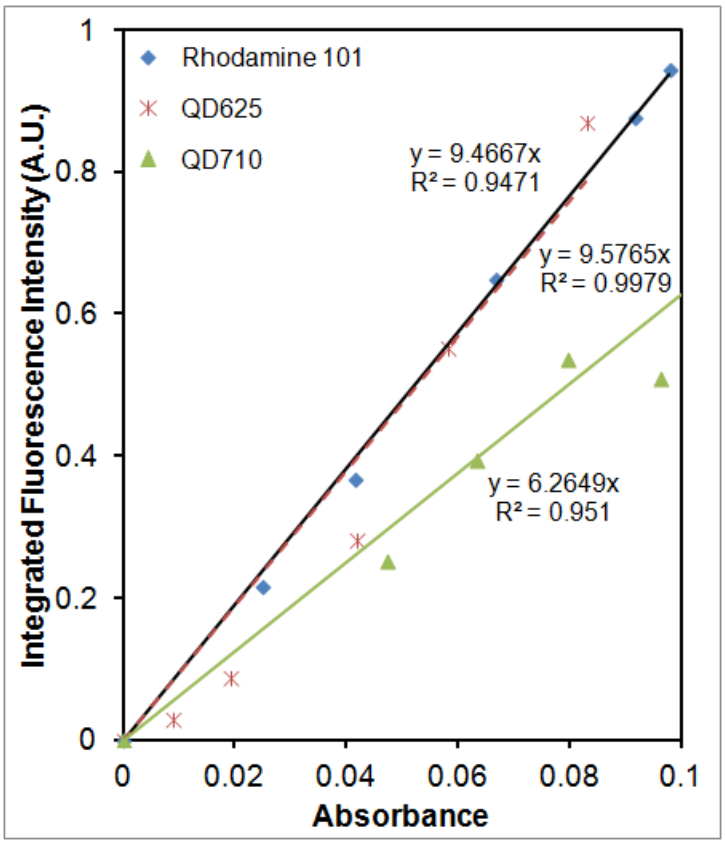

Figure 18. Plots of fluorescence intensities vs absorbance of rhodamine 101, QD625 and QD710.

Table 5. Quantum Yield (Φ) of silver-doped ZnSe samples

Sample	QY (%)
QD515	35.0
QD625	47.4
QD710	20.9

n_{PBS} = 1.333, $n_{ethanol}$ = 1.361 and n_{NaOH} = 1.3576 (Weber 2003).

3.4 Conclusion

In summary, we have developed an aqueous strategy to synthesize water-soluble, near-infrared emitting, silver-doped ZnSe QDs stabilized by a biomolecule, L-glutathione. Their emission ranged from 515 to 710 nm with 20-47 % QY. Compared to conventional synthetic methods, our approach is mild, inexpensive and environmentally friendly. We believe our strategy will be an alternative for preparing biocompatible QDs for wide range of biological applications.

Chapter 4

Biological Evaluation of Water-Soluble, Silver-Doped Zinc Selenide Quantum Dots

4.1 Background

Engineered nanomaterials are envisaged to have many exciting impacts in biomedical research], but progress is impeded by a lack of understanding of how these materials interact with biological environments. Among all the nanomaterials, quantum dots (Nabiev *et al.*) are most widely studied. A prime issue related to QDs is their toxicity. For any newly designed QDs it is crucial that these nanomaterials would not have any adverse effects upon interaction with the cells. However, not all nanomaterials are inherently benign. Studies have shown nanomaterials do affect biological systems at cellular, subcellular and protein levels (Colvin 2004; Donaldson *et. al*. 2001). To assess their utility in biological systems it is important to scrutinize the behavior of QDs both at *in vitro* and *in vivo*.

Though *in vitro* studies require less stringent toxicological characterization than *in vivo*, however, *in vitro* experiments have less ethical issues, less expensive to run, are easier to control and reproduce and could provide preliminary ideas how a material will respond in the body. Many *in vitro* studies have suggested that nanomaterials could induce toxic reaction, triggering nanomaterials to degrade, thus releasing toxic metals (Kirchner *et al.* 2005; Hardman *et. al*. 2006) and producing reactive oxygen species (Lovric *et al.*

2005). In addition, surface chemistry of nanomaterials has been shown to affect toxicity *in vitro* (Lovric *et al.* 2005).

However, due to the fact that different cell types have different responses to nanomaterials, different intracellular fates are likely to affect the toxicity study outcomes. Furthermore, most toxicity data derived from *in vitro* studies might not truly reflect complexity arising from *in vivo* environments. For instance, diversity in the toxicity results is seen in the evaluation of carbon nanotubes (CNTs). Study by Manna *et. al.* (Manna *et al.* 2005) have found CNTs exhibits toxicity *in vitro*, while *in vivo* findings by Schipper et. al. (Schipper *et al.* 2008) did not display significant toxicity. Likewise, toxicology results for fullerenes by Sayes *et. al*. (Sayes *et al.* 2007) indicated the outcomes *from in vivo* evaluation were very different from *in vitro* data. Hence, it is preferred to include *in vivo* study for toxicological evaluation of a novel nanomaterial.

The objective of this study is to evaluate the toxicity of our novel heavy-metal free, near-infrared emitting QDs with *in vitro* protocol. After establishing preliminary find for *in vitro* study we will continue to conduct *in vivo* testing to understand the biodistribution of the QDs in mice. These *in vitro* and *in vivo* assessments could provide meaningfully evaluation of the potential safety of our novel QDs for biological applications.

4.2 Experimental Details

4.2.1 Materials

Minimum essential medium-α (MEM-α), Dulbecco's Modified Eagle Medium (DMEM), penicillin/streptomycin, and L-glutamine were purchased from Life Technologies (Rockville, MD). Fetal bovine serum was supplied by Atlanta Biologicals. Polyethylenimine, branched (M_w ~25 K) (PEI), hematoxylin and eosin y were obtained from Sigma-Aldrich (St. Louis, MO), Citrosol and Cytoseal were from Fisher Scientific and Thermo Scientific respectively.

4.2.2 Human mesenchymal stem cell (hMSCs) maintenance

Bone marrow-derived *h*MSCs provided by Tulane University Health Sciences Center were cultured MEM-α supplemented with 20% FBS, 1% penicillin/streptomycin, and 1 % L-glutamine. The cells were maintained at 37 °C, 5 % CO_2 environment. Subculture was performed at 1:5 to avoid exceeding 85 % cell confluence. *h*MSCs used in the experiments were between passages 6-9.

4.2.3 Murine macrophage cell line (RAW 264.7) maintenance

RAW 264.7 cells (ATCC, Manassas, VA) were cultured in DMEM supplemented with 10% FBS, 1% penicillin/streptomycin, and 2 mM L-glutamine. Subculture was performed at 1:5 to avoid exceeding 85 % cell confluence. RAW 264.7 used in the experiments were between passages 9-12.

4.2.4 QDs treatment for hMSC and RAW 264.7

*h*MSC and RAW 264.7 were separately seeded in 96 well plates (20,000 cells/well) in 100 μL MEM-α and DMEM respectively. After 24 h of incubation, the medium was refreshed with 100 μL of medium containing the silver-doped ZnSe and polyethlenimine (PEI) (Sigma, 25 kD) at various concentrations. Cells were incubated for 24 h before cell viability assays were performed.

4.2.5 MTS cell viability assay

Cellular viability of the quantum dots were determined by [3-(4,5-dimethylthiazol-2-yl)-5-(3-carboxymethoxyphenyl)-2-(4-sulfophenyl)-2H-tetrazolium, inner salt] (MTS) assay (Promega, Fitchburg WI) in comparison with PEI. Following 24 h of incubation with the silver-doped ZnSe nanocrystals and PEI, medium was removed from the wells and replaced with 100 μL of fresh culture medium. 20 μL of MTS stock solution was added to each well and the plate was subsequently incubated at 37 °C for 2 h before taking the absorbance on a microplate reader (BMG Labtech Fluostar Optima, Durham, NC) at 490 nm. Controls were cells that were incubated with culture medium.

4.2.6. In vivo and ex vivo imaging

The biodistribution of QD710 in live animals and collected tissues were visualized a Perkin Elmer IVIS Spectrum *in vivo* imaging system. The QDs was excited at 675 nm and its emission detected using 820 nm filter.

4.2.7 In vivo biodistribution analysis

Animal use protocols were reviewed and approved by the Institutional Animal Care and Use Committee of Duke University. 4 weeks old male nude mice were purchased Charles River Laboratories and allowed to acclimate to the animal facility for at least 48 h. Thereafter, the animals were placed on adjusted vitamins diet (Harlan Laboratories, Madison, WI) 1 week prior to experimentation to eliminate fluorescent material usually found in standard rodent chow. For *in vivo* imaging, mice were anesthetized with isoflurane (2 % in oxygen) delivered from a precision vaporizer. QD710 was dissolved in PBS at a concentration of 50 mg/mL, Qdot800 ITK Amino (PEG) (Life Technologies) was diluted to 0.16 μM with PBS. Typical volumes injected were 50 or 100 μL for footpad and intravenous injection respectively. After each study, anesthetized mice were euthanized and major organs were collected for *ex vivo* imaging and histology analysis.

4.2.8 Hematoxylin and eosin (H&E) staining of frozen sections

Frozen sections were first fixed in 10 % buffered formaldehyde for 20 min and washed in water for 5 min. The sections were then immersed in hematoxylin solution (Sigma-Aldrich, St. Louis, MO) to stain the nuclei for 1 min, washed in water for 5 min, and briefly immersed in 95 % ethanol. Staining of cytoplasms were carried out by immersing in eosin for 2 min and dipped once quickly in water. Dehydrations were performed next by immersing the sections in 95 % ethanol for 1 min, and then three times in 100 % ethanol for 10 dips each. The

sections were washed three times in Citrosol for 2 min each. Lastly, the slides were mounted with Cytoseal and sealed with #1.5 coverslip.

4.2.9 Microscopic analysis

After 24 h of incubation with QD710, medium was removed from the wells and the cells were washed three times with warm PBS and viewed under a fluorescent microscope excited at λ_{ex} = 485 nm with λ_{em} = 650 nm captured by a CCD camera (CoolSnap HQ, Roper Scientific).

Confocal images were taken on a Zeiss LSM 510 inverted confocal microscope with a 40x/1.3 oil lens. For Hoescht 33426 staining, 405 nm diode laser was used for excitation and DAPI emission filter for signal readout. For QD710 binding assessment, 561 nm diode laser was used as excitation source and Red emission filter to capture the signal.

H & E stained samples were visualized on Zeiss Axio Imager widefield fluorescence microscope equipped with QImaging MicroPublisher 5.0 MP colour camera and 20x/0.50 DIC lens.

4.3 Results and Discussion

4.3.1 Toxicity assay and microscopic analysis

MTS is a colorimetric method for determination of number of viable cells in proliferation. MTS is bioreduced by viable cells to formazan product (Figure 19) that is soluble culture medium (Barltrop *et al.* 1991). Metabolically active cells contain dehydrogenase enzymes that convert MTS into aqueous, soluble formazan. Absorbance at 490 nm corresponds to quantity of formazan produced and is directly proportional to number of viable cells in culture.

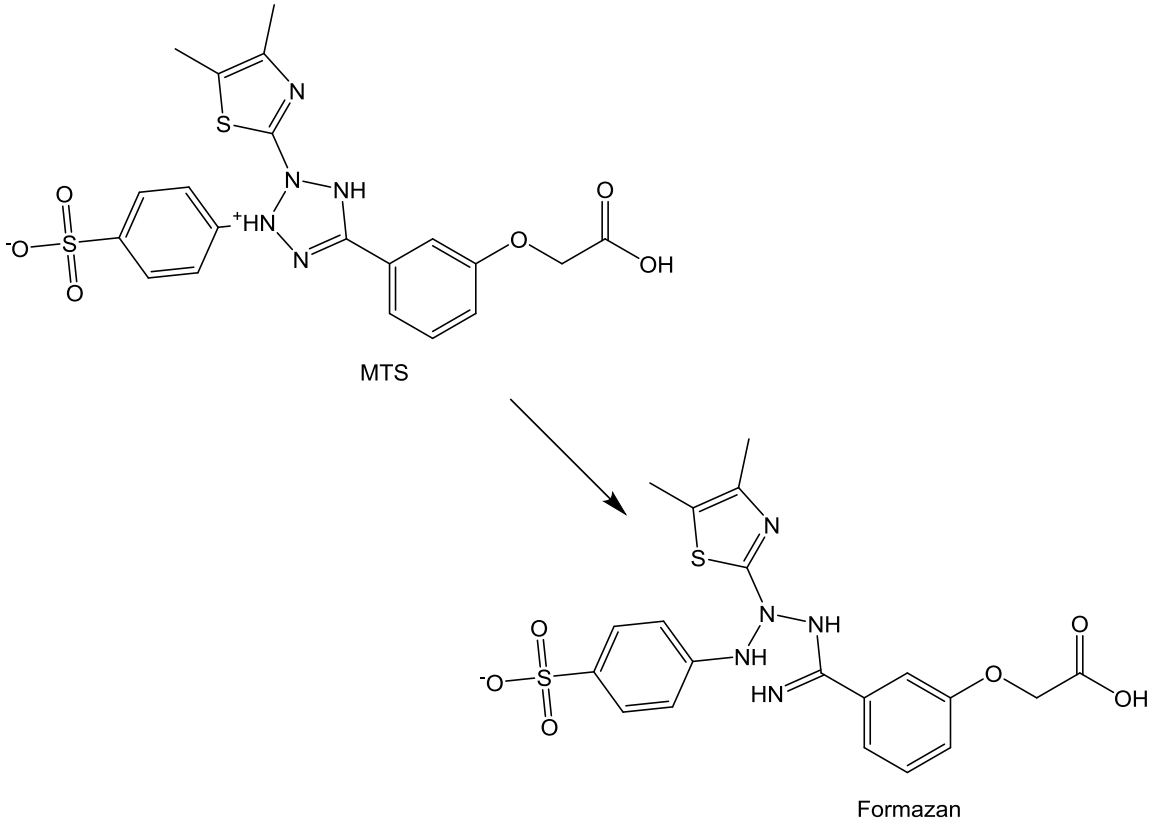

Figure 19. Structures of MTS tetrazolium salt and its formazan product.

In the toxicity study, QDs with different emission were evaluated in two different cell lines. Branched PEI, a commonly used polymeric carrier for transfection of plasmid DNA into target cells, was included as control. PEI has shown cytotoxicity in a range of cell lines. The cytotoxicity arises from two different mechanisms: (1) the disruption of the cell membrane leading to necrosis; (2) the disruption of the mitochondrial membrane post-internalization leading to apoptosis (Hunter 2006). As shown in Figure 20, at higher concentration of 100 μg/mL there was a slight drop in the viability in the RAW 264.7 cells treated with QDs. On contrary, minimal change of viability in *h*MSC (Figure 21) was observed. The insensitivity of *h*MSC towards the treatment of QDs could possibly be attributed to the high serum contents in the medium provide buffering effect towards toxicants (Gartlon *et al.* 2006). In addition, slightly higher viability was observed in *h*MSC treated with QD510 across the concentration range. This could possibly be due the stimulation of the cells in the presence of QD510 (Thayer *et al.* 2005).

Microscopic analysis of RAW 264.7 cells and *h*MSC are shown in (Figure 22) and (Figure 23) respectively. The results indicated that QD710 readily bind nonspecifically with both RAW 264.7 cells and *h*MSC. In addition, regardless of the cells type, when treated with the negatively charged QD710, the QDs could escape from endosomes, release in the cytoplasm and accumulate near the nuclear pore complexes. This observation is in agreement to the results by Nabiev et. al. (Nabiev *et al.* 2007)

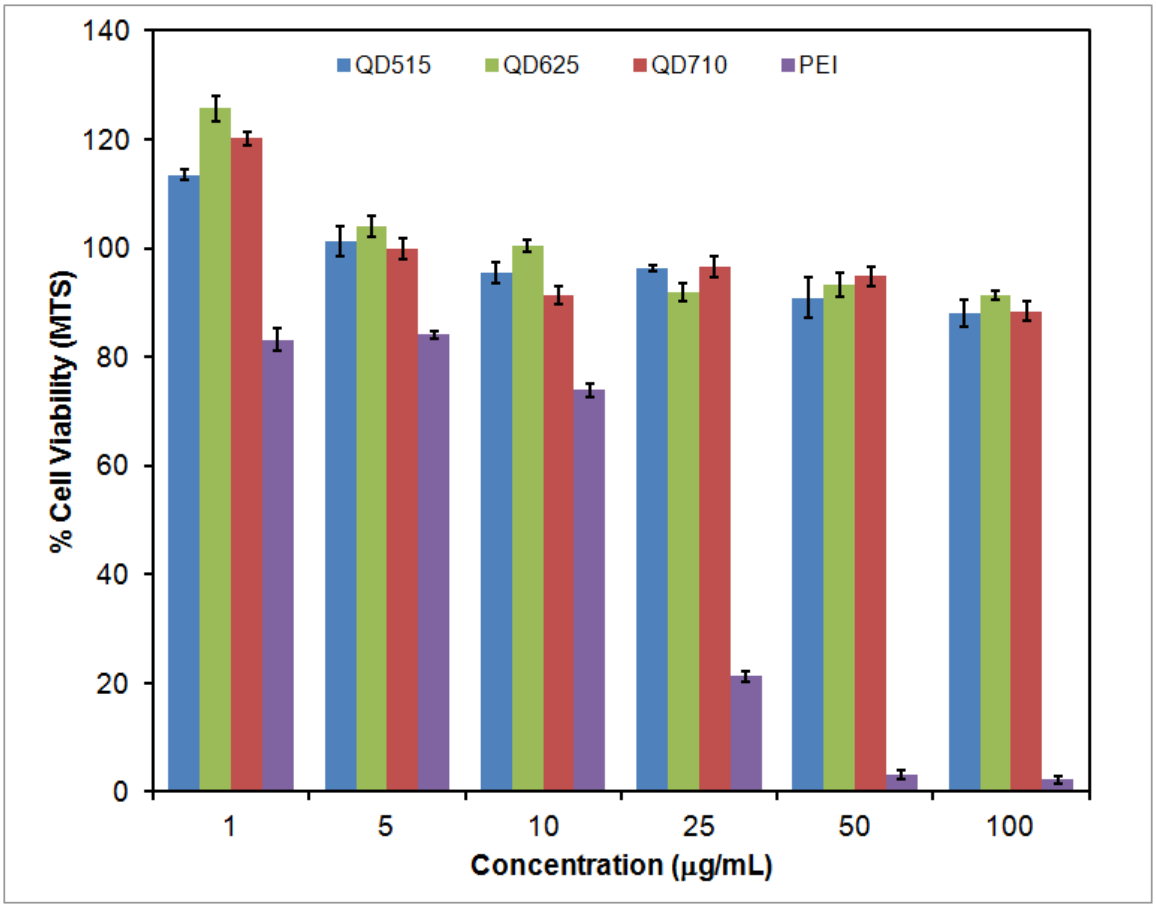

Figure 20. MTS cell viability of RAW 264.7 cells following 24 h of incubation with QD515, QD625, QD710 and PEI. Values are the mean ± standard error of the data (N = 8).

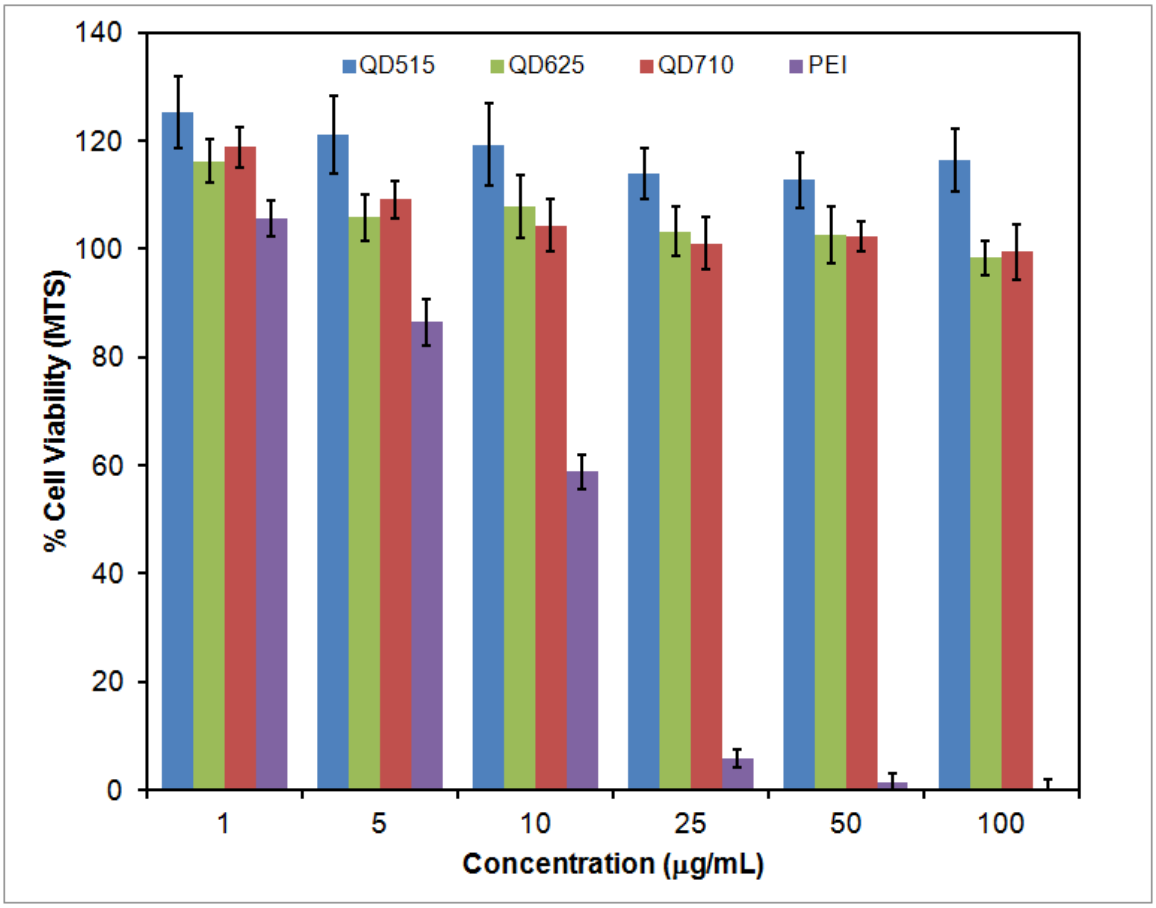

Figure 21. MTS cell viability of *h*MSC following 24 h of incubation with QD515, QD625, QD710 and PEI. Values are the mean ± standard error of the data (N = 8).

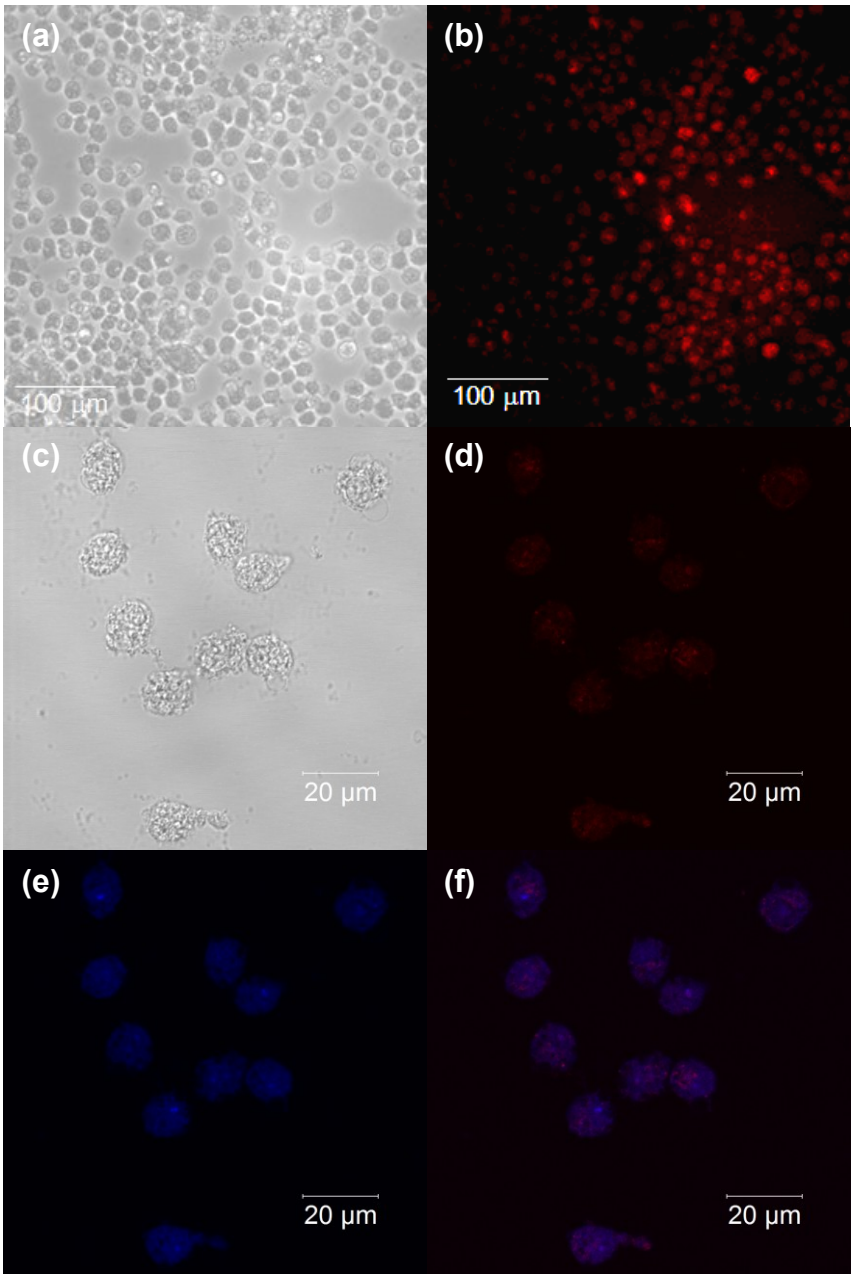

Figure 22. Fluorescent and confocal microscopy imaging of RAW 264.7 cells. (a) Brightfield image. (b) Fluorescent image with λ_{ex} = 485 nm, λ_{em} = 650 nm (c) Brightfield image. (d) Image with 561 nm excitation source and observed with red filter. (e) Nuclei staining with Hoescht 33346, excitation at 405 nm and observed with DAPI filter. (f) Overlap of two images.

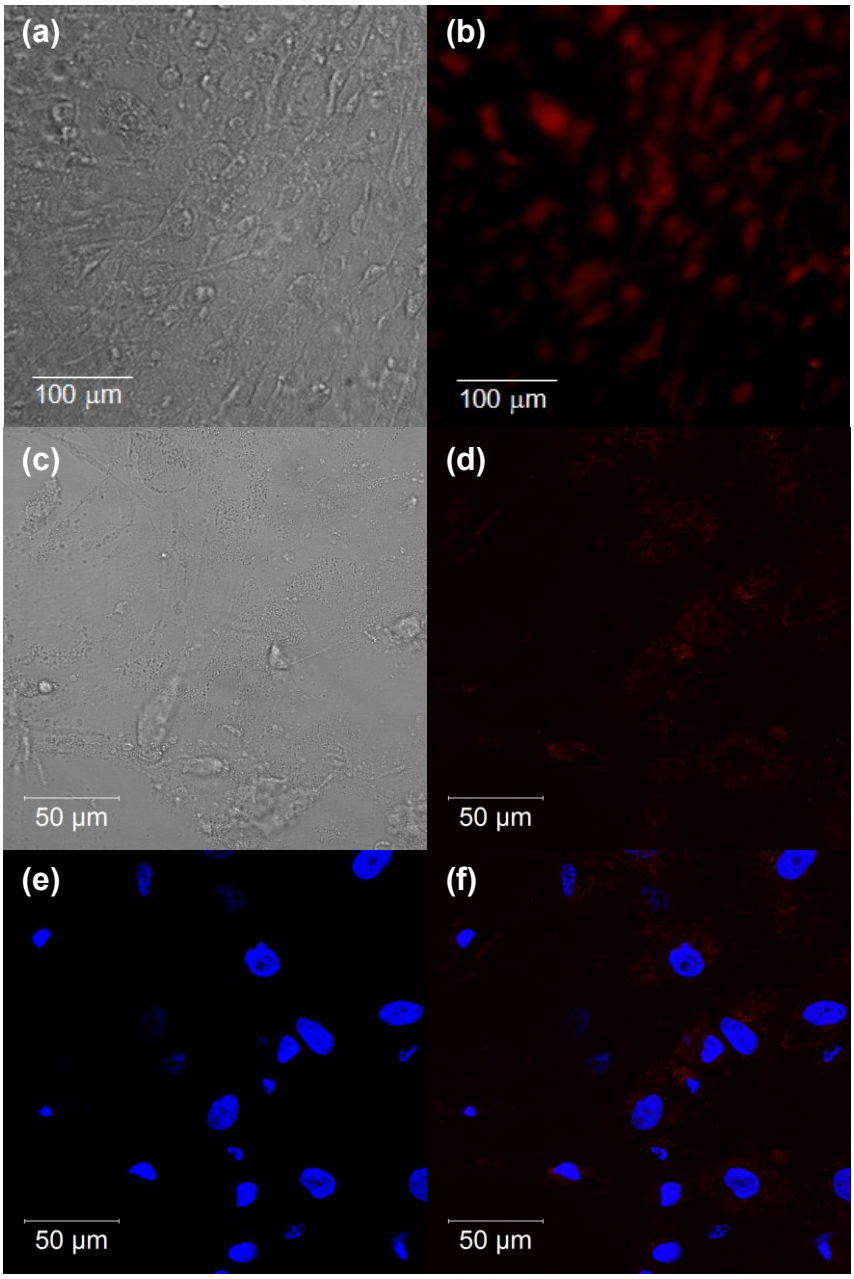

Figure 23. Fluorescent and confocal microscopy imaging of *h*MSC. (a) Brightfield image. (b) Fluorescent image with λ_{ex} = 485 nm, λ_{em} = 650 nm (c) Brightfield image. (d) Image with 561 nm excitation source and observed with red filter. (e) Nuclei staining with Hoescht 33346, excitation at 405 nm and observed with DAPI filter. (f) Overlap of two images.

4.3.2 In vivo biodistribution

Imaging in small animals is a challenge due to absorbance and scattering, and autofluorescence in tissues. This can be overcome when imaging is done in the near-infrared region where absorbance and scattering is minimal (Lim *et al.* 2003; Frangioni *et. al*. 2003). In addition, Bawendi and Frangioni have demonstrated selective sentinel lymph nodes mapping with subdermally administered NIR QDs in rodent and pig models in which QD fluorescence was observable up to 1 cm deep through the skin of the animals (Kim *et al.* 2004; Kim *et al.* 2005).

We have developed a procedure for the synthesis of water-soluble, near-infrared emitting, silver-doped ZnSe QDs with diameters < 8 nm. We were able to tune the final peak emission wavelength to 710 nm (QD710) that is ideal for *in vivo* applications. We were able to conduct *in vivo* biodistribution studies along with commercial QD800-NH_2 that we acquired from Life Technologies. The QDs were administered into the footpads of nude mice. The difference in migration of the two types of QDS was observed immediately. In the case of QD800-NH_2, migration into the lymphatic system and staining of the popiteal lymph node required ~40 min after injection. In contrast, instead of entering the lymphatic vessels, we saw QD710 enter the systemic circulation and accumulate in the stomach of the mouse ~5 h after injection (Figure 24). This observation is in agreement with the report by Nune *et. al*. which suggested that particles < 10 nm, when administered subcutaneously, will be absorbed by the capillary network that eventually got drained into systemic circulation (Nune *et al.* 2011). The

signal of QD710 in stomach increased after 24 h probably due to the slowness in the migration in the systemic circulation. Interestingly, the signal of QD710 in the stomach was detectable up to at least 7 days. When the QDs were administered to the tail vein, QD800-NH_2 QDs was found to traverse through the lymphatic vessels and accumulated at the linguinal lymph nodes 5 h-24 h post treatment (Figure 25). The observations for QD800-NH_2 are in agreement with results by Soltesz, *et. al*. that particles larger than 10 nm will enter lymphatic system and become sequestered in the lymph node (Soltesz *et al.* 2006). However, for the case of QD710, we saw the QDs were accumulated in the stomach. The size of QD710 is < 8 nm, as so it probably could not efficiently filter by the kidney or concentrated in the bladder since the threshold for renal filtration is < 6m (Dellian *et al.* 2000). Since Zn^{2+} has a major role in regulating acidity in the secretory compartments of gastric gland, this could possibly account for the preferred accumulation of QD710 circulated near the stomach region (Liu *et al.* 2011).

4.3.3 Histology analysis

Histological assessment of the tissues was conducted to identify the existence of QDs in the samples and to determine whether tissue damage or inflammation occur. Directly after cryo-section, tissues were evaluated by confocal microscopy to search for QD710. A total of 50 sections were evaluated and only slices with fluorescent signals are shown in Figure 26 and Appendix I. Presented in Figure 26a is a confocal image of a cryo-section of the gastric mucosa that was found to contain QD710, and its representative histology result

is shown in Figure 26c. Overall, there were no apparent histopathological abnormalities to stomach of the treated mouse. QD710 was found in the whole section and not limited to specific section.

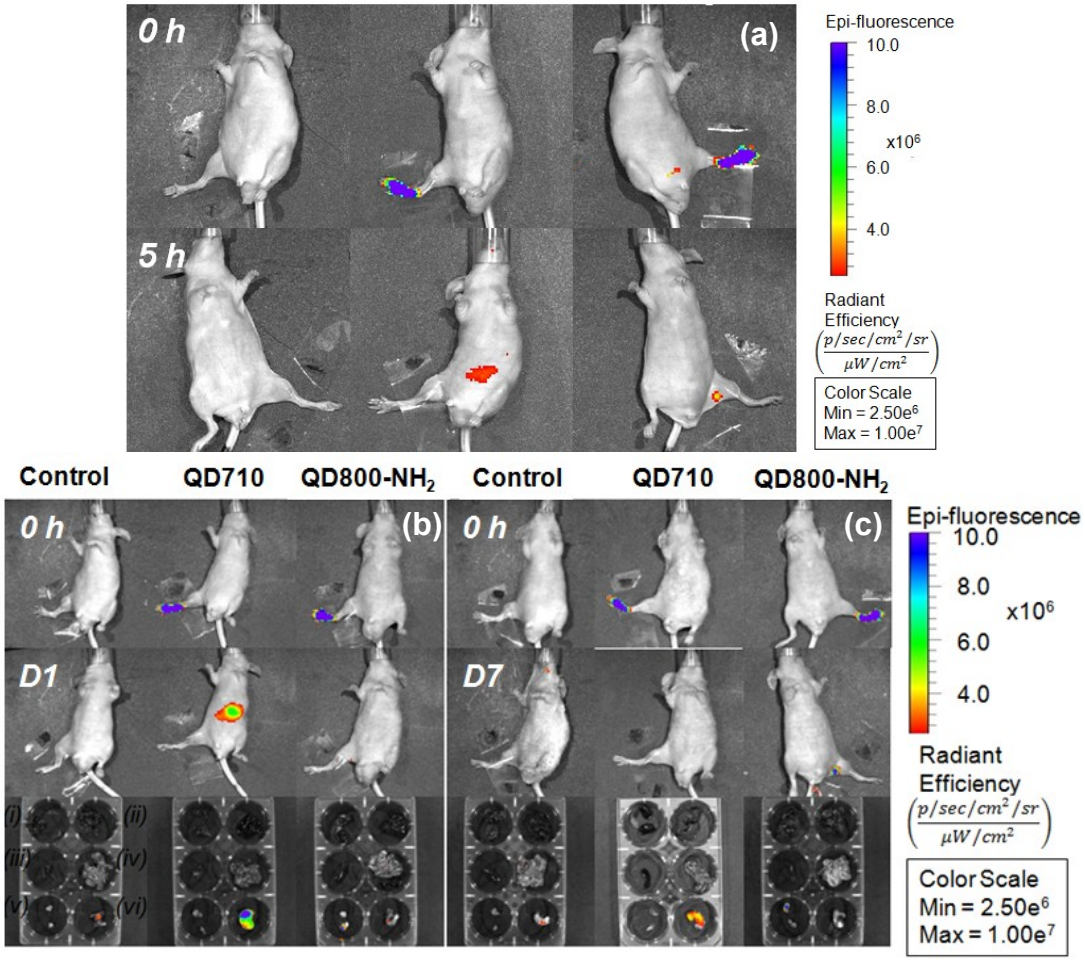

Figure 24. *In vivo* imaging of Ag-doped ZnSe QDs (ZSA710) and Qdot 800 ITK amino (PEG) quantum dots (Invitrogen) (QD800-NH_2) after footpad injections in Nu/Nu mice. The mice were anesthetized, injected with PBS (50 μL) as control, ZSA710 (50 μL, 50 mg/mL) or QD800-NH_2 (50 μL, 0.16 μM) and the fluorescence was measured with the IVIS Spectrum using filter sets 675/820 (Ex/Em). The fluorescence pattern was analyzed at different time interval post-injection, (a) 5 hr, (b) 1 day, and (c) 7 days. The mice were sacrificed; the organs were harvested and imaged. (i) Kidneys, (ii) liver, (iii) spleen, (iv) intestines, (v) popiteal lymph nodes, and (vi) stomach. Fluorescence signals were observable up to 7 days post treatment for both type of QDs. QD800-NH_2 QDs traversed through the lymphatic vessels and accumulated at the popiteal lymph nodes (LN) 5 h-7 days post treatment. In contrast, ZSA710 QDs were circulated through systemic route post-injection and accumulated in the stomach for as long as 7 days. At least three animals were treated with PBS, ZSA710 or QD800-NH_2 for each condition.

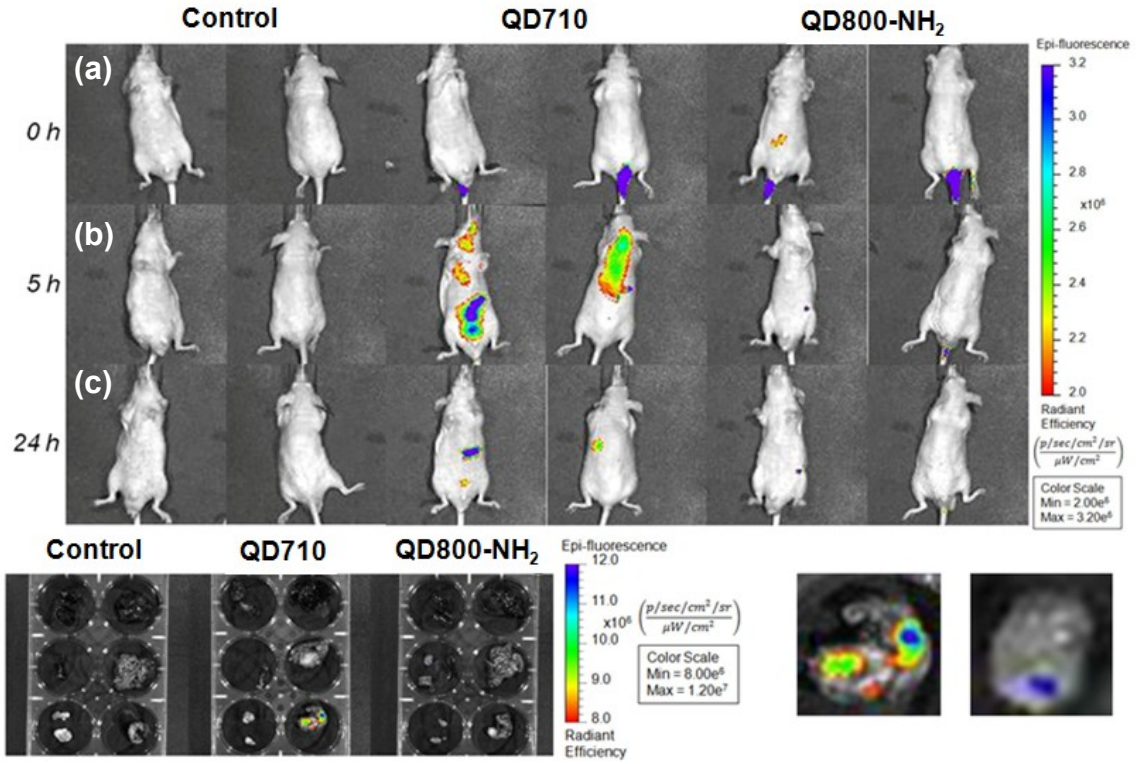

Figure 25. *In vivo* imaging of Ag-doped ZnSe QDs (ZSA710) and Qdot 800 ITK amino (PEG) quantum dots (Invitrogen) (QD800-NH_2) after tail vein injection in Nu/Nu mice. The mice were anesthetized, injected with PBS (50 μL) as control, ZSA710 (50 μL, 50 mg/mL) or QD800-NH_2 (50 μL, 0.16 μM) and the fluorescence was measured with the IVIS Spectrum using filter sets 675/820 (Ex/Em). The fluorescence pattern was analyzed at different time interval post-injection, (a) 0 hr, (b) 5 hr, and (c) 1 day. QD800-NH_2 QDs traversed through the lymphatic vessels and accumulated at the linguinal lymph nodes 5 h-24 h post treatment. In contrast, ZSA710 QDs were circulated through systemic route post-injection and accumulated in the stomach.

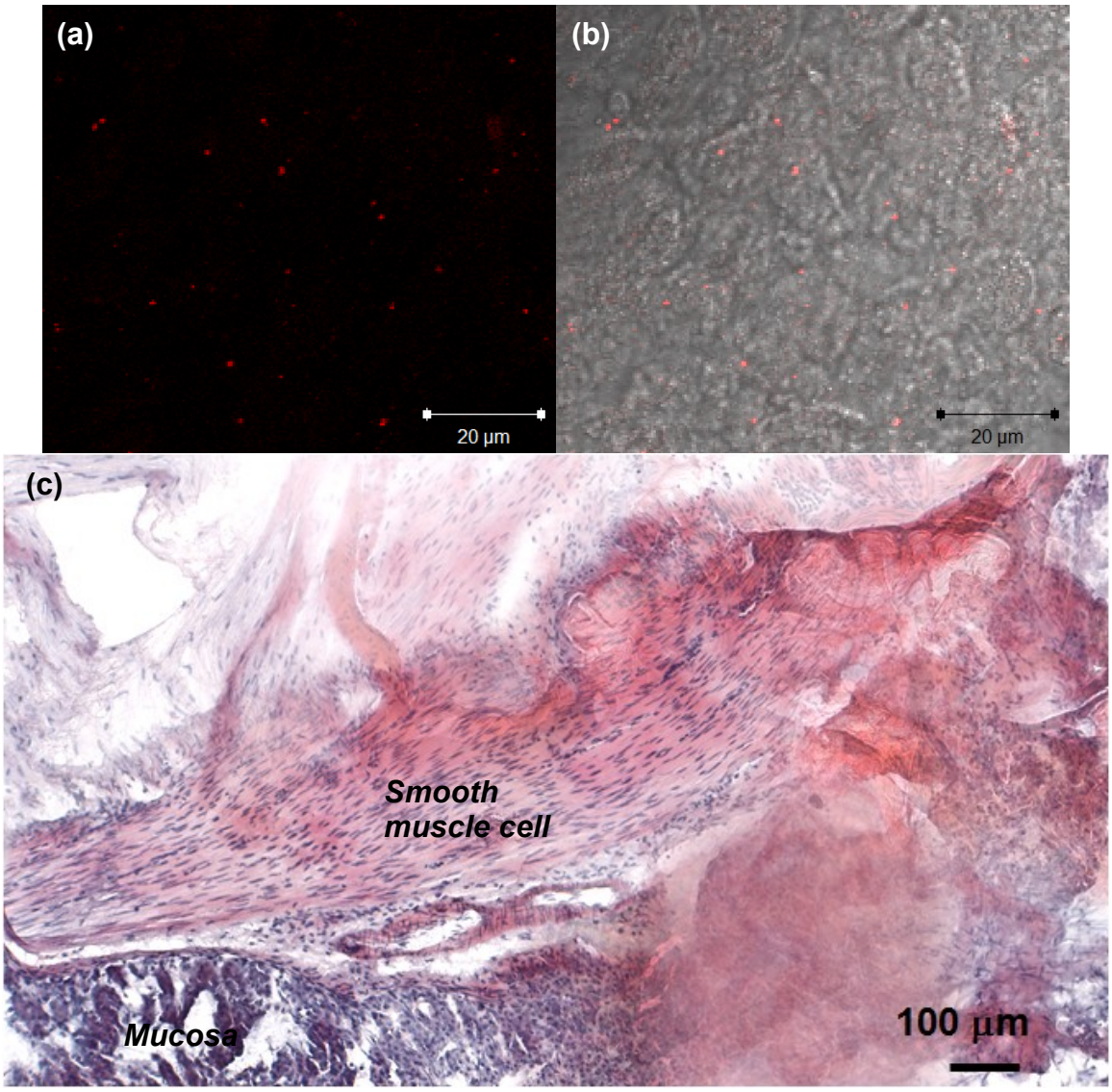

Figure 26. Histology for a cryo-section of gastric mucosa. (a) Confocal image with 561 nm excitation source and observed with red filter. (b) Overlaps of brightfield and red filter. (C) Hematoxylin and eosin staining.

4.4 Conclusion

We have successful developed a series of water-soluble, silver-doped ZnSe QDs with emission in the near-infrared range. These QDs exhibited minimal toxicity to RAW 264.7 cells and hMSC. When tested in animal QD710 was found to behave differently from conventional QDs. The underlying mechanism of QDs accumulating in the stomach is still unknown and further studies are required to address this observation. Overall, we have shown that silver-doped ZnSe QDs has the potential for biological applications.

Chapter 5

Biofunctional Quantum Dots for Cell-Specific Targeting

5.1 Background

Gastric cancer is the second leading cancer-related death in the world (Zhang *et al.* 2012). Typically, early stages of gastric cancer do not show any symptom, and patients diagnosed with gastric cancer are already in advanced-stage with a poor prognosis. When early gastric cancer is left untreated, it will progressively become gastric carcinoma that metastasizes aggressively; and along with the high resilience of the gastric cancer cells, this is attributed to the very poor survival rates of gastric cancer patients. The overall 5-year relative survival rate of all people with gastric cancer in the United States is about 28% (Tan *et al.* 2011). However, it has been shown that gastric cancer can be cured if it is diagnosed at an early stage (Tan *et al.* 2012).

Functionalized quantum dots (QDs) are of great potential for biomedical research. With unique optical properties including broad absorption, spectra narrow emission spectra, high resistance to photobleaching and high photostability, QDs are excellent for candidates for cell-labeling studies. Since QDs has a large surface area, they can be readily modified to incorporate bioactive moieties. For cancer cell targeting studies, QDs are typically antibodies, ligands or peptides. In general, antibodies are most commonly used targeting moieties due to its high availability and specificity.

CD44 is a major cell surface receptor for hyaluronate, and is implicated in several cellular mechanism such as cell-cell interactions, cell adhesion and migration. Recently study has shown that some CD44 variants are associated with malignant transformation (Tao *et al.* 2011). Particularly, CD44v6 isoform is overexpressed in the process of malignant transformation of gastric mucosa. The objective of this study is to take the advantage of the functional groups on L-glutathione capped QDs to append bioactive moiety, thus producing QDs for cell-specific targeting applications. Active targeting will be augmented by a primary monoclonal Mouse anti-Human CD44v6 antibody on QDs to bind with the receptors on human gastric adenocarcinoma cell line (AGS).Human small intestine cells (FHs 74 Int) was used as control for the cellular study. The targeting specificity and cellular internalization of the antibody-labeled QDs will be visualized by confocal microscopy.

5.2 Experimental details

5.2.1 Materials

CD44v6 Mouse Monoclonal Antibody (clone MA54), DMEM, Ham's F-12K (Kaighn's) Medium, penicillin/streptomycin, Hoescht 33342 were obtained from Life Technologies (Rockville, MD). Fetal bovine serum was supplied by Atlanta Biologicals. Polyethylenimine, branched (M_w ~25 K) (PEI), sodium *meta*-periodate, epithelial growth factor (EGF) were purchased from Sigma Aldrich (St Louis, MO). Sodium cyanoborohydride ($NaCNBH_3$), and Zeba spin desalting column were supplied by Pierce Biotechnology (Rockford, IL).

5.2.2 Preparation of CD44v6-QDs conjugate

CD44v6-QDs was prepared by first activation of monoclonal mouse CD44v6 antibody. 10 μL of sodium *meta*-periodate (0.2 M) in sodium acetate buffer (0.1 M) was added to 200 μL of CD44v6 (0.5 mg/mL) in an amber bottle and incubated at room temperature for 50 min. The reaction mixture was purified through a Zeba spin column. The collected filtrate was added to a bottle containing 50 mg of QD710 in 2 mL of PBS and 10 μL of 5 M $NaCNBH_3$ that was pre-dissolved in 1 M NaOH. The reaction was allowed to proceed overnight at 4 °C. The reaction was purified by ultrafiltration with 100 K MWCO membrane, added with PBS to a final volume of 200 μL and stored at -20 °C. Absorption and fluorescence spectra of CD44v6-QDs in PBS were obtained with Shimadzu UV2501PC spectrophotometer and Cary Eclipse Fluorescence Spectrophotometer equipped with a xenon flash lamp excited at 450 nm and 5 nm bandpass respectively.

5.2.3 Human gastric adenocarcinoma cell line (AGS) maintenance

AGS was acquired from ATCC (Manassas, VA) Center were cultured in DMEM supplemented with 10% FBS, 1% penicillin/streptomycin. Subculture was performed at 1:5 to avoid exceeding 85 % cell confluence. AGS used in the experiments were between passages 49-52.

5.2.4. Human small intestine cell line (FHs 74 Int) maintenance

FHs 74 Int was acquired from ATCC (Manassas, VA) Center were cultured in Ham's F-12K (Kaighn's) medium supplemented with 10% FBS, 1% penicillin/streptomycin, and 30 ng/mL of EGF. Subculture was performed at 1:5 to avoid exceeding 85 % cell confluence. FHs 74 Int used in the experiments were between passages 6-8.

5.2.5 MTS cell viability assay

Cellular viability of the quantum dots were determined by [3-(4,5-dimethylthiazol-2-yl)-5-(3-carboxymethoxyphenyl)-2-(4-sulfophenyl)-2H-tetrazolium, inner salt] (MTS) assay (Promega, Fitchburg WI) in comparison with PEI. Following 24 h of incubation with the silver-doped ZnSe nanocrystals and PEI, medium was removed from the wells and replaced with 100 μL of fresh culture medium. 20 μL of MTS stock solution was added to each well and the plate was subsequently incubated at 37 °C for 2 h before taking the absorbance on a microplate reader (BMG Labtech Fluostar Optima, Durham, NC) at 490 nm. Controls were cells that were incubated with culture medium.

5.2.6 Immunofluorescent imaging

AGS and FHs 74 Int were separately seeded with 10,000 cells/well in 8-well Nunc™ Lab-Tek™ chambered coverglass (Fisher Scientific) in 400 μL DMEM and Ham's F-12K respectively. After 24 h of incubation, the culture media removed and the cells were washed three times with PBS (5 min per wash). The cells were fixed with 4 % paraformaldehyde for 15 min, followed by three washes, 5 min each with PBS. The cells were then blocked in 10 % FBS for 30 min followed by three washes with PBS. Subsequently, 200 μL each of QD710 (100 μg/mL) and CD44v6-QDs (diluted to 1:200) in PBS were added in the wells. After 2 h of incubation at 37 °C, the cells were subjected to nuclear staining with Hoescht 33342 (2 ug/mL) for 5 min and washed three times with PBS (5 min each). In a separate experiment, cells were directly incubated with 200 μL of QD710 (100 μg/mL) in culture media. After 2 h of incubation, the culture media removed and the cells were washed three times with PBS (5 min per wash). The cells were staining with Hoescht 33342 (2 ug/mL) for 5 min and washed three times with PBS (5 min each). The cells were visualized with a Zeiss LSM 510 inverted confocal microscope with a 40x/1.3 oil lens. A 405 nm diode laser for excitation and DAPI emission filter were used for Hoescht 33426 signals, and a 561 nm diode laser and red emission filter were used for QDs readout.

5.3 Results and Discussion

5.3.1 Preparation of CD44v6-QDs conjugate

The reaction scheme of CD44v6-QDs conjugation is depicted in Figure 27. Aldehyde activation route was chosen over the conventional 1-ethyl-3-(3-dimethylaminopropyl)carbodiimide (EDC) and N-hydroxysuccinimide (NHS) conjugated antibodies to QD so as to ensure that the antigen-binding domains will not be adversely affected. Activation of the activate the polysaccharides located in the Fc region of the Ab was achieved using a mild oxidant, sodium *meta*-periodate, to create two aldehyde groups that are spontaneously reactive to amine- and hydrazine-containing reagents. In the current conjugation, the generated aldehydes coupled with primary amines on L-glutathione to form Schiff bases intermediates that were in equilibrium with their free forms. Reductive amination was carried out with the addition of sodium cyanoborohydride to complete the reduction of the labile Schiff base intermediate to form a chemically stable, secondary amine linkage between CD44v6 and QD710. The absorption and fluorescence spectra of CD44v6-QDs are illustrated in Figure 28. The measurement revealed that CD44v6-QDs maintained the desired optical properties. Since the size of antibody and QDs are similar (Figure 10), the conjugation reaction possibly results in several CD44v6 antibodies reside on the surface of QDs as depicted in Figure 27. The optical properties of QDs are size-dependent; a shift in emission peak could be due to the increase in overall size of the conjugate as compared to the primary QD710.

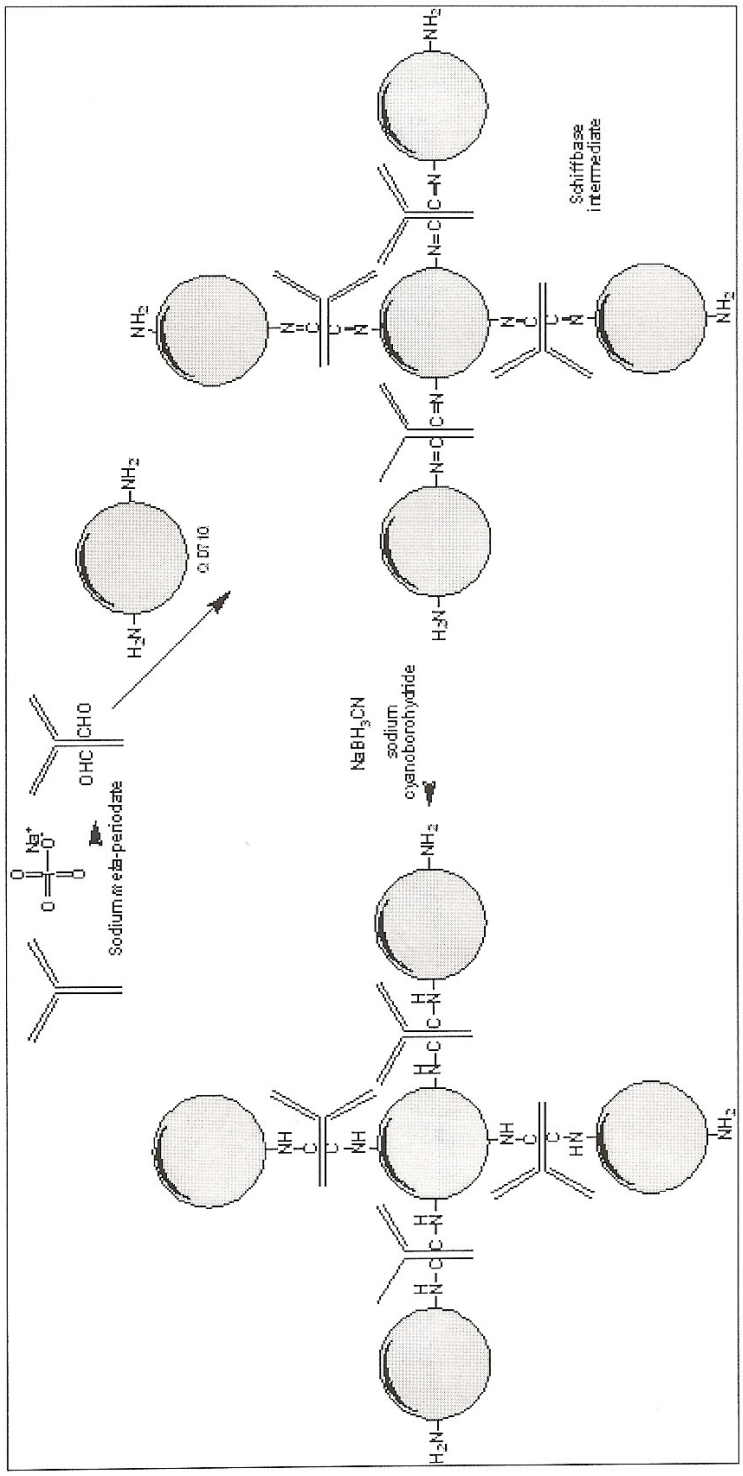

Figure 27. Schematic of conjugation of antibody to quantum dots via glycosalation site on antibody.

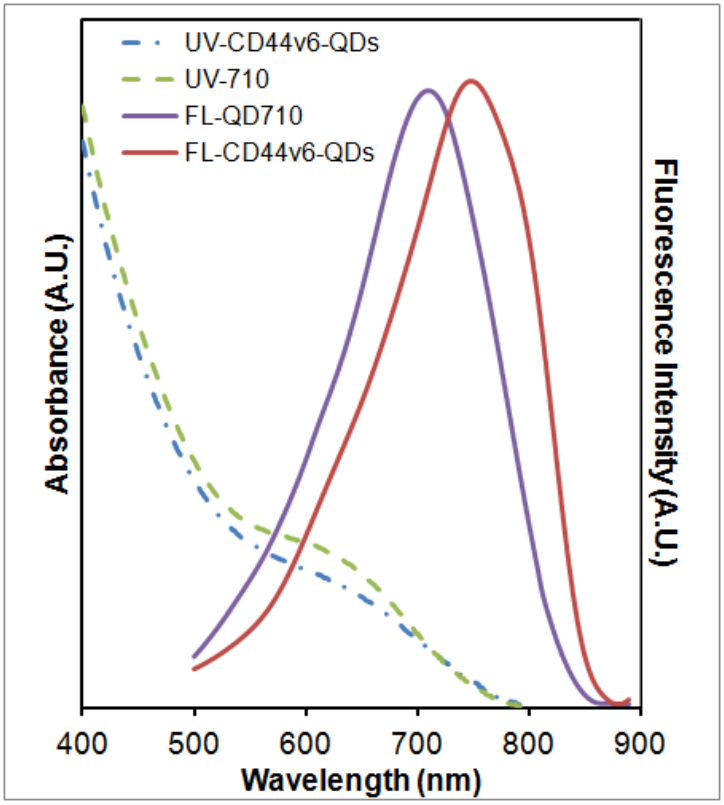

Figure 28. Absorption (⋯) and fluorescence (—) spectra of QD710 and CD44v6-QDs.

5.3.2 Cytotoxicity assay

To evaluate the cytotoxic effects of our water soluble, silver-doped ZnSe QDs, the viability of AGS and FHs 74 Int cells were determined using a standard MTS assay. AGS and FHs 74 Int cells were incubated with QD515, QD625, QD710 and PEI at different concentrations for 24 h. As shown in Figures 29 and 30, cells treated with QDs did not exhibit any significant drop in viability over the range of concentrations. Interestingly, the viabilities of AGS treated with QD625 over the concentration range of 1-50 μg/mL were slightly higher than the other two QDs. This could possibly be attributed to the stimulation effect of the cells in the presence of QD510 (Gartlon *et al.* 2006).

5.3.3 Immunofluorescent Imaging

The immunofluorescent imaging were conducted with three different conditions: (1) direct treatment of non-fixed cells with QD710; (2) fixed cells without bovine serum blocking were incubated with QD710; (3) fixed cells subjected to bovine serum blocking were incubated with CD44v6-QDs. Figure 31 and 32 are images of cells directly treated with QD710. Without fixation and blocking, nonspecific binding was observed. In a passive uptake study by Nabiev et. al. (Nabiev *et al.* 2007), they have shown that negatively charged thiolglycolic acid-capped CdTe QDs could escape from endosomes, release in the cytoplasm and associate near nuclear pore complexes (NPC). Our results agree with those reported by Nabiev *et. al*., in that the negatively charged QD710 was seen in the NPC of AGS and FHs 74 Int. As a result of blocking with bovine serum nonspecific binding of the QDs can be eliminated to avoid false-positive results (Figure 33 and 34). The most superior property of the CD44v6-QDs is the precise recognition of the receptors on AGS cell. Due to this specificity, we achieved cell-specific binding of AGS cells as shown in Figure 35. Our study clearly validated that in the absence of the receptors, CD44v6-QDs will not bind with FHs 74 Int cells (Figure 36).

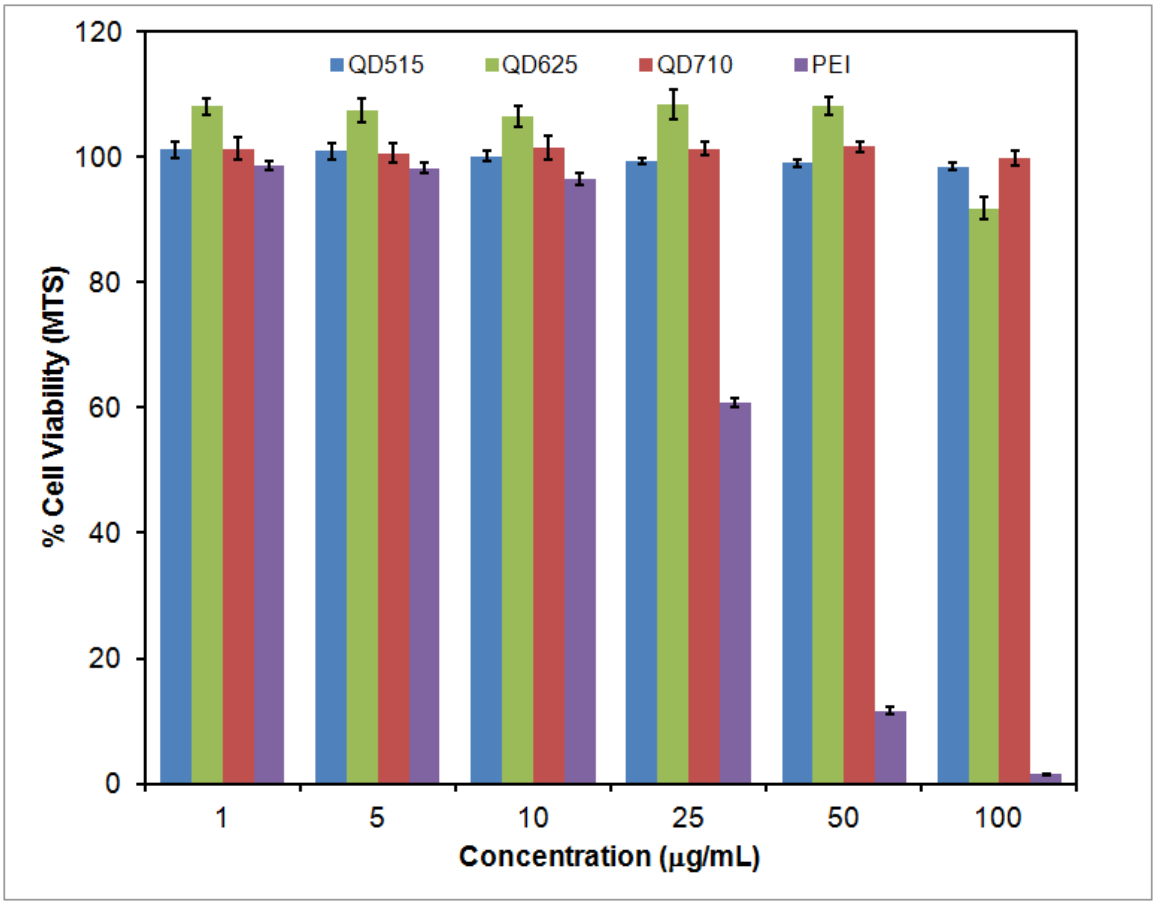

Figure 29. MTS cell viability of AGS following 24 h of incubation with QD515, QD625, QD710 and PEI. Values are the mean ± standard error of the data (N = 8).

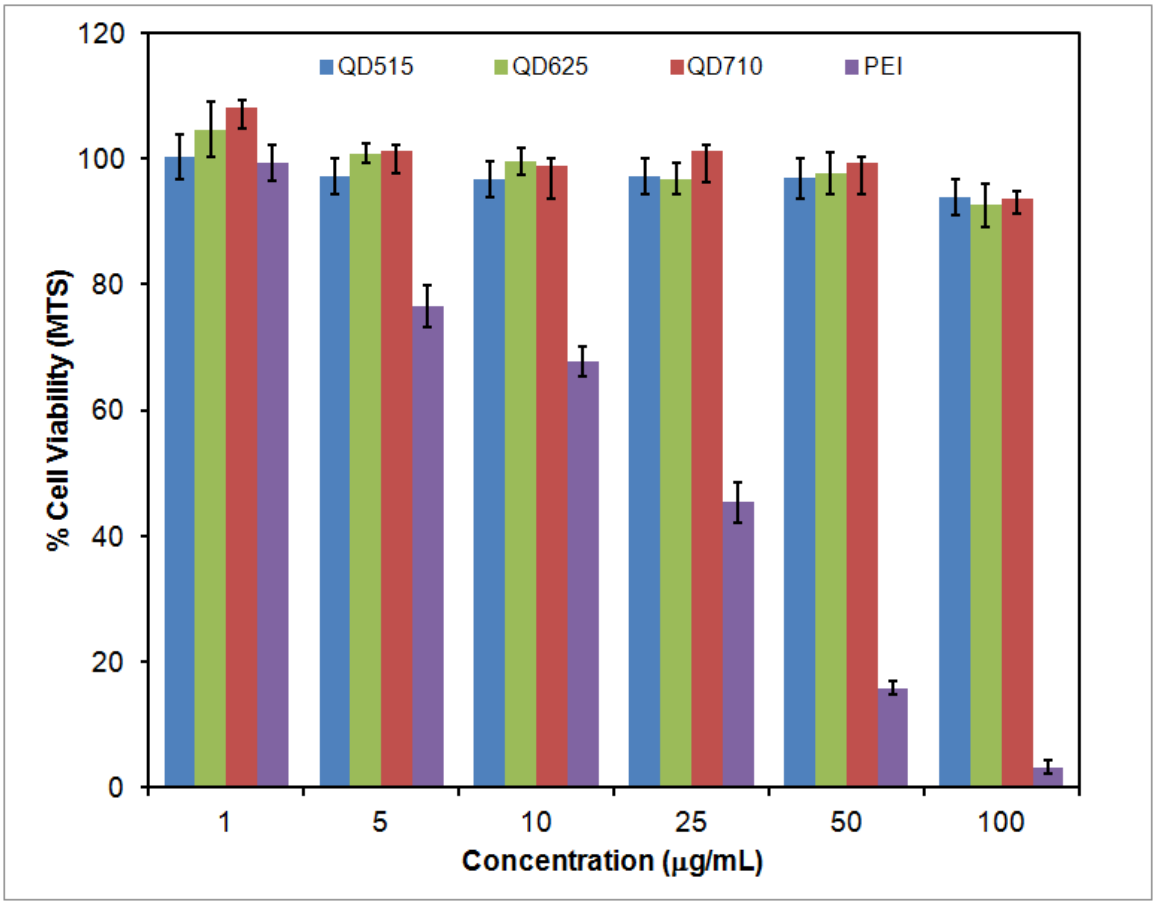

Figure 30. MTS cell viability of FHs 74 Int following 24 h of incubation with QD515, QD625, QD710 and PEI. Values are the mean ± standard error of the data (N = 8).

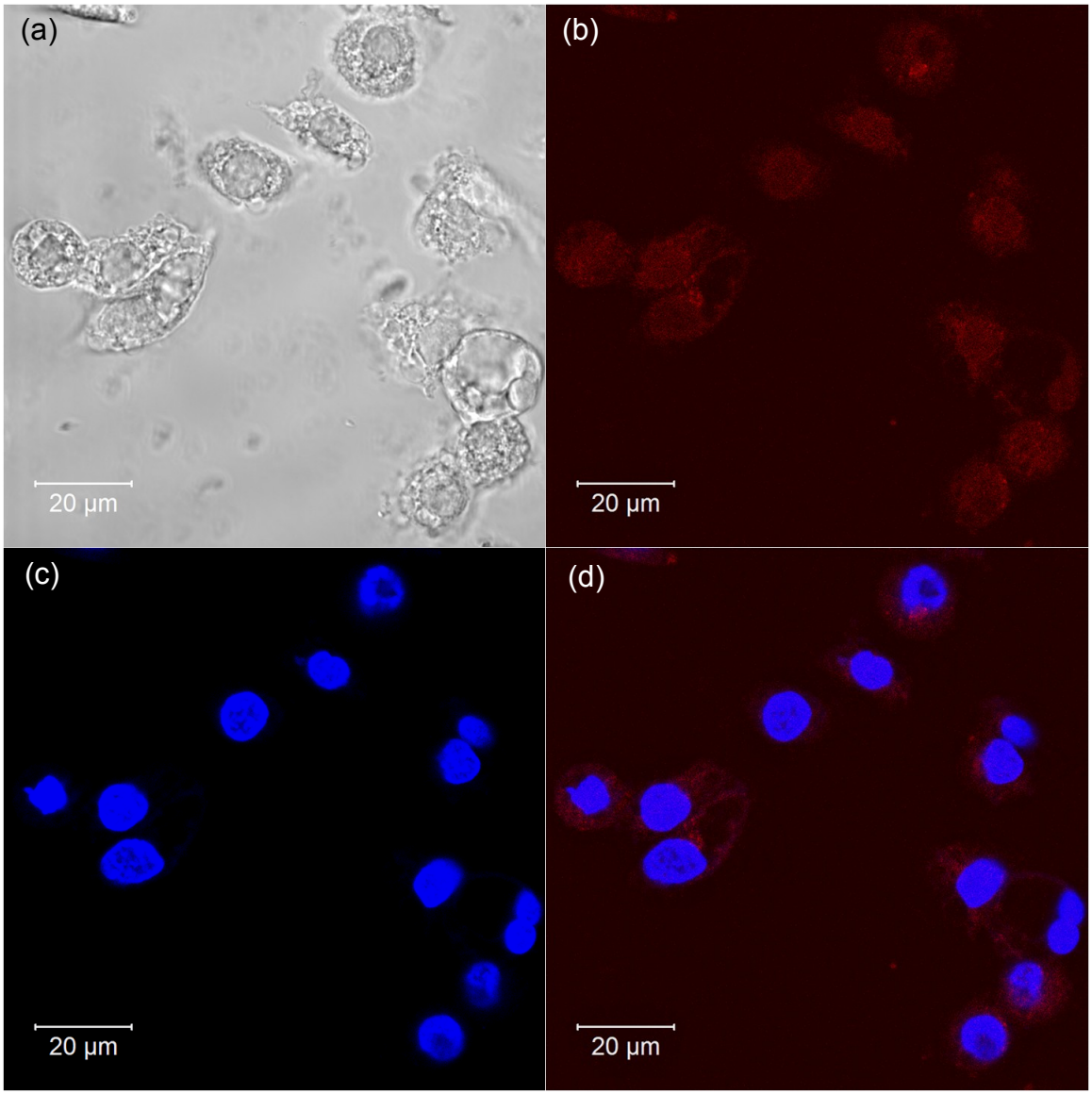

Figure 31. Confocal microscopy imaging of AGS cells. Cells were directly treated with QD710 for 2 h at 37 °C. (a) Brightfield image. (b) Image with 561 nm excitation source and observed with red filter. (c) Nuclei staining with Hoescht 33346, excitation at 405 nm and observed with DAPI filter. (d) Overlap of two images.

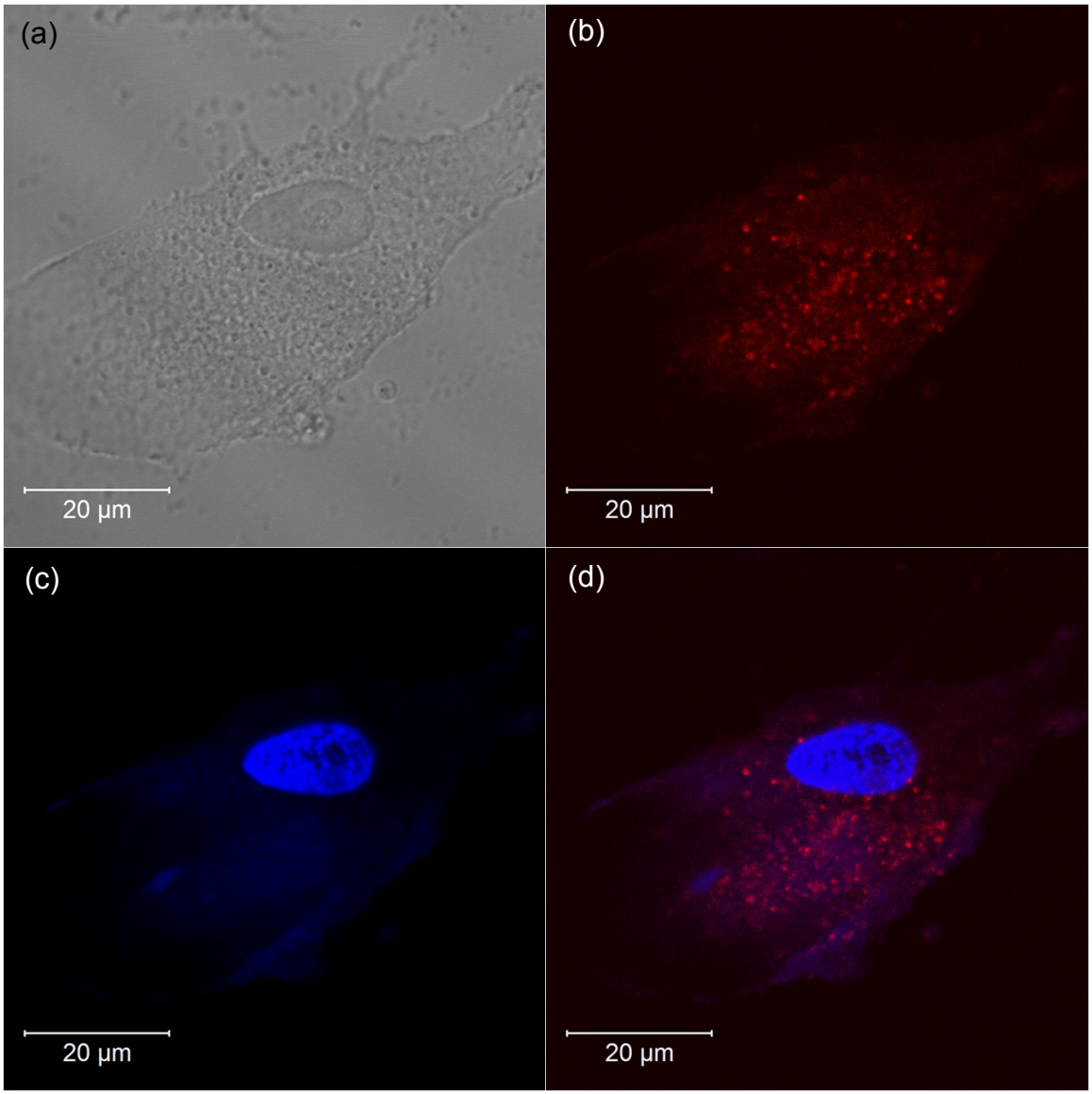

Figure 32. Confocal microscopy imaging of FHs 74 Int cells. Cells were directly treated with QD710 for 2 h at 37 °C. (a) Brightfield image. (b) Image with 561 nm excitation source and observed with red filter. (c) Nuclei staining with Hoescht 33346, excitation at 405 nm and observed with DAPI filter. (d) Overlap of two images.

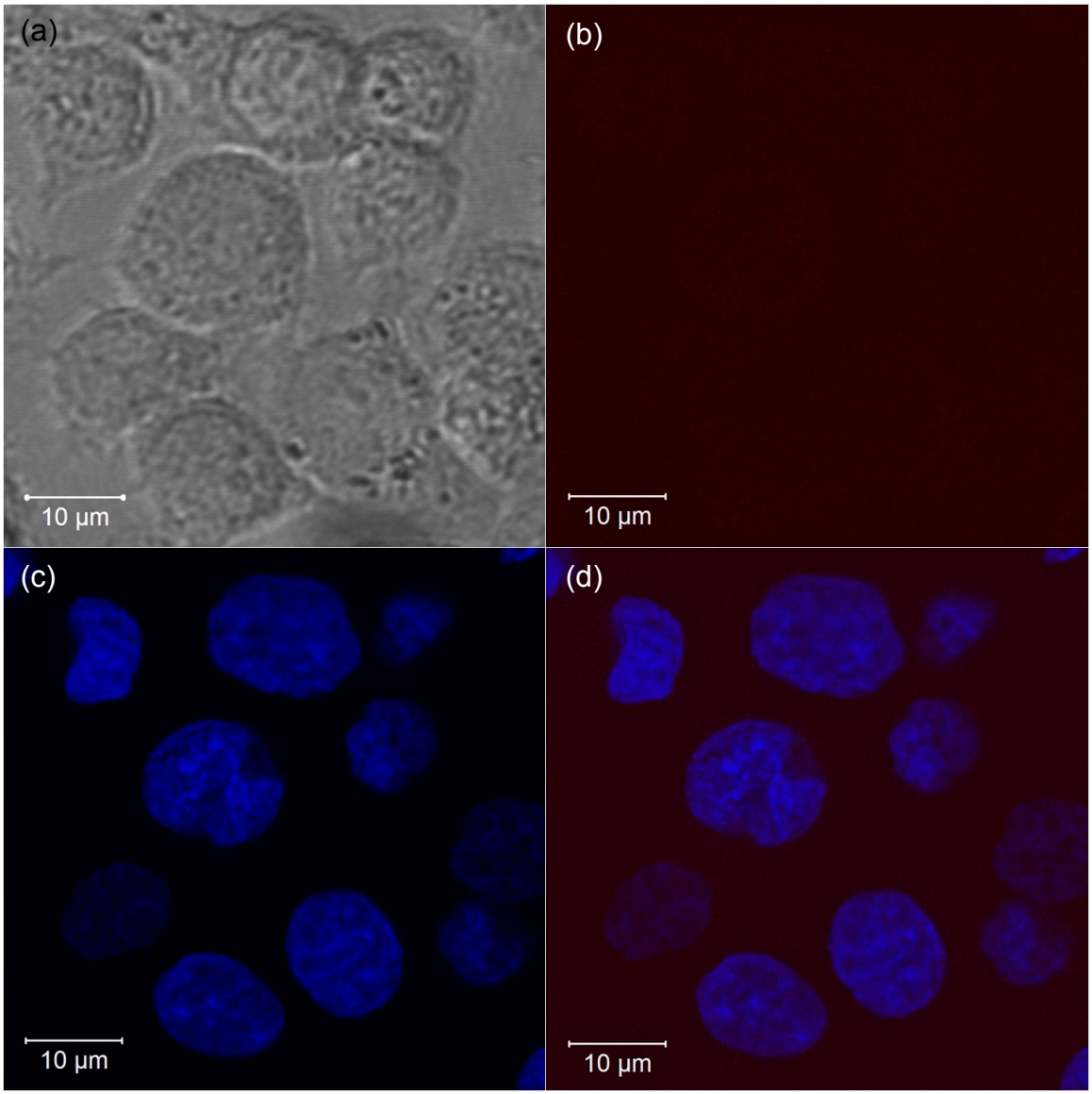

Figure 33. Confocal microscopy imaging of AGS cells. Cells were fixed and blocked with bovine serum prior to incubation with QD710 for 2 h at 37 °C. (a) Brightfield image. (b) Image with 561 nm excitation source and observed with red filter. (c) Nuclei staining with Hoescht 33346, excitation at 405 nm and observed with DAPI filter. (d) Overlap of two images.

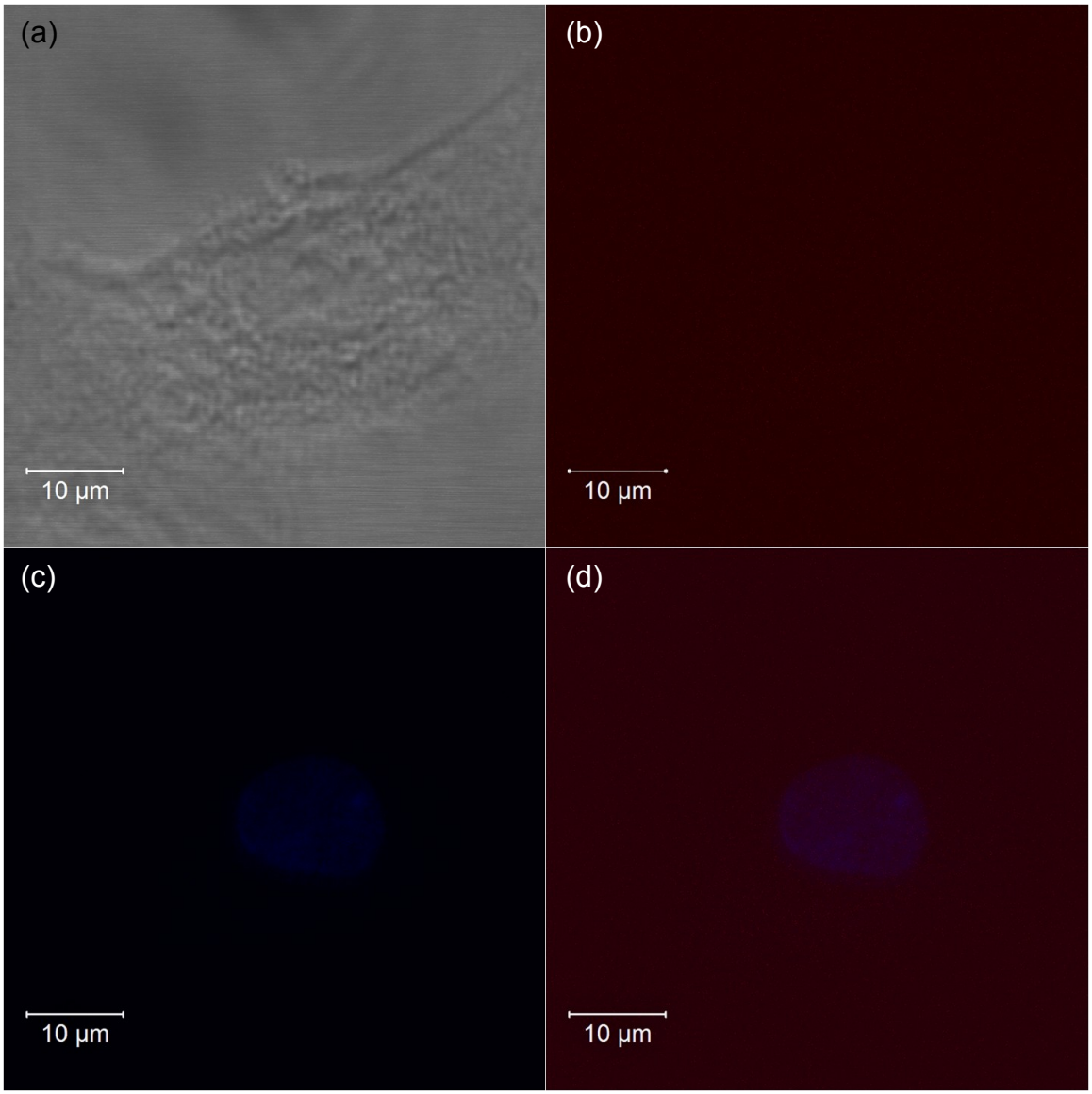

Figure 34. Confocal microscopy imaging of FHs 74 Int cells. Cells were fixed and blocked with bovine serum prior to incubation with QD710 for 2 h at 37 °C. (a) Brightfield image. (b) Image with 561 nm excitation source and observed with red filter. (c) Nuclei staining with Hoescht 33346, excitation at 405 nm and observed with DAPI filter. (d) Overlap of two images.

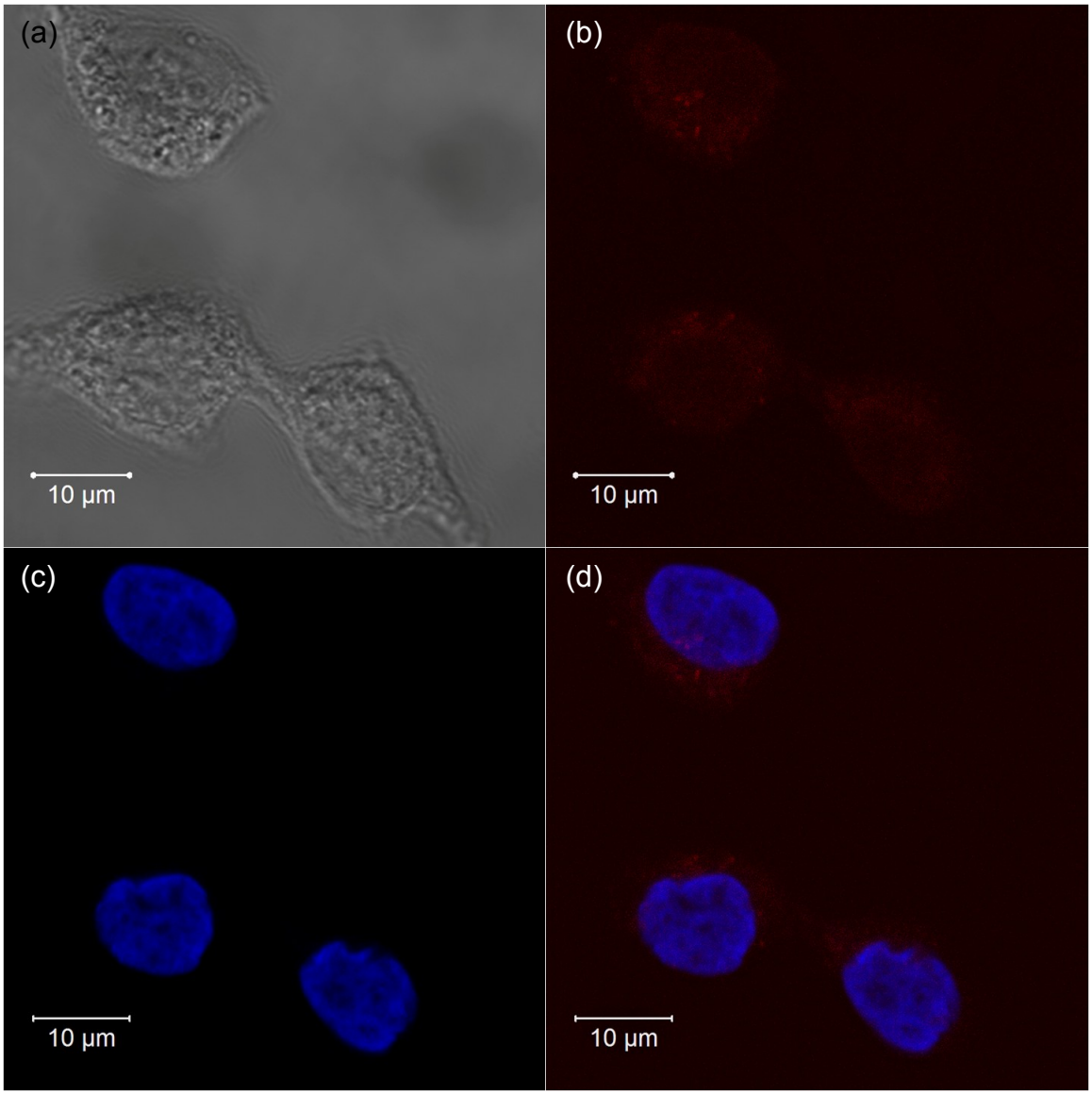

Figure 35. Confocal microscopy imaging of AGS cells. Cells were fixed and blocked with bovine serum prior to incubation with CD44v6-QDs for 2 h at 37 °C. (a) Brightfield image. (b) Image with 561 nm excitation source and observed with red filter. (c) Nuclei staining with Hoescht 33346, excitation at 405 nm and observed with DAPI filter. (d) Overlap of two images.

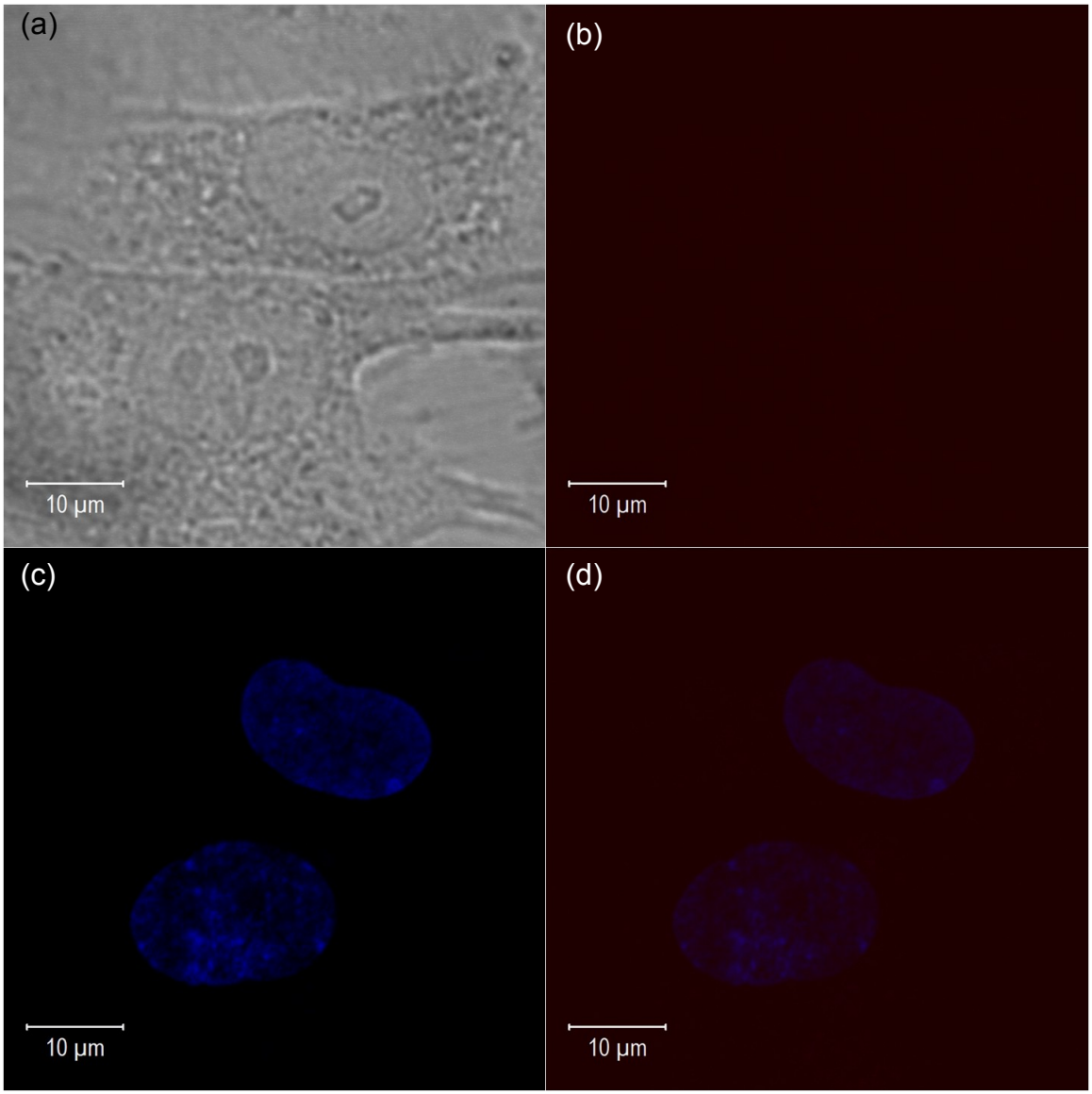

Figure 36. Confocal microscopy imaging of FHs 74 Int cells. Cells were fixed and blocked with bovine serum prior to incubation with CD44v6-QDs for 2 h at 37 °C. (a) Brightfield image. (b) Image with 561 nm excitation source and observed with red filter. (c) Nuclei staining with Hoescht 33346, excitation at 405 nm and observed with DAPI filter. (d) Overlap of two images.

5.4 Conclusion

We have tested the series of water soluble, silver-doped ZnSe QDs, stabilized with L-glutathione and showed that they have minimal toxicity towards AGS and FHs 74 Int cells. We have demonstrated the feasibility of chemical modification on the surface with L-glutathione capped QDs to incorporate bioactive moiety for cell-specific targeting purposes. The available carboxylate and amine groups on L-glutathione could be used for conjugation with various bioactive moieties and thus this series of QDs could potentially be used for a wide range of specific targeting applications.

Chapter 6

Near-Infrared Emitting, Silver-Doped Zinc Selenide Quantum Dots As Nanoprobe For Delivery To Draining Lymph Nodes

6.1 Background

In any drug discovery and development, the challenge to translate from preclinical to clinical phases depends on the efficacy and safety of the drug. A more effective way to screen for drugs to move into clinical phases is to conduct preclinical animal testing to provide reliable insight into potential efficiency and indication of safety for use in humans (Contag 2002). As so, the ability to conduct real-time *in vivo* analysis of molecular events, assessment of therapeutic efficacy of test compound will definitely be a valuable technique for any drug development.

In vivo fluorescent imaging is a relatively safe imaging modality as it utilizes, nonionizing light as excitation source. *In vivo* fluorescent imaging is especially challenging due to fluorescent signal attenuation varies according to the emission wavelength, type and depth of tissues (Frangioni 2003). Tissues tend to absorb and scatter photons and generate strong autofluorescence when illuminated with light source in the range of 450-600 nm but are biologically transparent in the NIR range (650-950 nm). Most fluorescent proteins have emission peaks in the visible spectrum, several organic dyes emitting in the NIR are being developed as alternative imaging reagents to conjugate to

biomolecules. However, organic dyes are susceptible to photobleaching, and aggregation in aqueous media (Quek *et. al*. 2012). As such, it is justifiable that with its improved photostability, quantum dots are increasingly being used for labeling and *in vivo* imaging. The objective of this study is to explore the feasibility of using our near-infrared emitting, silver-doped ZnSe QDs as a nanoprobe to elucidate the delivery of encapsulated cytokine to the draining lymph nodes.

Draining lymph nodes (DLN) are dynamic lymphoid structures where B, T and other immunity cells could be found. They act as filters or traps for foreign particles and maintain the proper functioning of immunity (Soderberg *et al.* 2005; McLachlan *et. al*. 2003). During infection, mast cells release stable heparin-based particles containing tumor necrosis factor (Kunder *et al.* 2009; Abraham *et al.* 2010; St John *et al.* 2012) that are delivered to the DLN. However, how these molecules could remain intact during the delivery process is pending to be addressed. Here we demonstrate the labeling of heparin with silver-doped ZnSe QDs, use it as a nanoprobe to form nanocomplexes chitosan, a biopolymeric cation, and track the delivery of encapsulated recombinant tumor necrosis factor to popiteal lymph nodes.

6.2 Experimental Details

6.2.1 Materials

Gold (IIII) chloride trihydrate ($HAuCl_4 \cdot 3H_2O$), citric acid trisodium salt ($Na_3C_6H_5O_7$), sodium sulfite were obtained from Sigma-Aldrich(St Louis, MO). Dibromodecane and thiourea were bought from Alfa Aesar. 1-Ethyl-3-(3-dimethylaminopropyl) carbodiimide hydrochloride (EDC), *N*-hydroxysulfosuccinimide (NHS); 2-(*N*-morpholino)ethanesulfonic acid **(**MES) buffer were from Pierce Biotechnology (Rockford, IL). Chitosan of Mw ~470 K was purchased from Novamatrix and heparin of Mw ~15 K was from EMD Millipore. Recombinant tumor necrosis factor alpha (TNF-α) was acquired from R & D Systems

6.2.2 Synthesis of 10-mercaptodecanesulfonate sodium salt (MDS)

10-Bromodecanesulfonic acid sodium salt

The synthesis of MDS was performed with slight modification from a method reported by Fiurasek, *et. al*. (Fiurasek *et al.* 2007). Dibromodecane (85.44 g, 0.284 mol) was added to a round bottom flask containing 120 mL of ethanol and 40 mL of water, and the mixture was heated to reflux with continuous stirring. Sodium sulfite (7.13 g, 0.057 mol) dissolved in 80 mL of water was gradually introduced into the reaction flask with a dropping funnel over a period of 3 hours to facilitate the reaction on only one end of the dibromodecane. After an additional 4 hours of refluxing, the reaction flask was cooled to allow excess dibromodecane to separate from the reaction mixture. The aqueous layer was washed three times with 50 mL of petroleum ether to remove any trace of

unreacted dibromodecane. The purified aqueous layer was concentrated on a rotary evaporator to remove ethanol. The remaining solution was cooled at 4 °C to allow 10-bromodecanesulfonic acid sodium salt to crystallize. The resultant crystals were isolated by filtration and vacuum dried overnight. The dried product was verified by proton NMR.

10-S-thiouronium decanesulfonate

10-bromodecanesulfonic acid sodium salt (11.51 g, mol) and thiourea (2.71 g, 0.036 mol) were dissolved in a mixture of 125 mL of ethanol and 40 mL of water. After 6 hours of refluxed with stirring, ethanol was removed by rotary evaporation. The resulting solution was allowed to cool at 4 °C for crystallization of the product to occur. The dried product was verified by proton NMR.

10-mercaptodecanesulfonate sodium salt

10-S-thiouronium decanesulfonate (6.31 g, mol) was dissolved in 72 mL of 2 M sodium hydroxide and the reaction flask was refluxed under argon gas for 3 hours to bring about base hydrolysis to cleave the C-S bond thus releasing alkylthiol and urea. The reaction flask was removed from heating and kept under argon atmosphere and allowed to cool to room temperature. Concentrated sulfuric acid was slowly added to the reaction mixture to adjust the pH of the solution to 7 in order to facilitate protonation of the thiol functional group. The solution was then cooled in ice for crystallization to take place. The purified product was dried under vacuum and evaluated by NMR.

6.2.3 Gold nanoparticle synthesis

Gold nanoparticle was prepared according to the method reported by (Turkevich *et al.* 1951, Frens, 1973 #8). 0.1534 g of $HAuCl_4 \cdot 3H_2O$ was dissolved in 15.34 mL of Millipore water to make up 1 wt % stock solution. 0.2052 g of $Na_3C_6H_5O_7$ was added to 20.52 mL of water to make 1 wt % sodium citrate stock solution. 10 mL of sodium citrate was added to a flask containing 4 mL of gold stock solution and 400 mL of boiling water under reflux. After 10 min the reaction flask was removed from heating and allowed to cool to room temperature. The gold nanoparticle was filtered with 0.45 μm cellulose acetate membrane and kept at 4 °C for long term storage.

6.2.4 Functionalization of gold nanoparticle

50 mg of 10-mercaptodecanesulfonate sodium salt was sonicated in 5 mL of a 50:50 ethanol/water mixture and added to 25 mL of gold nanoparticle solution. The functionalization was allowed to proceed at room temperature for 3 days. Unbound thiol ligand was removed in the supernatant fraction after centrifugation at 15,000 rpm for 20 min. The gold nanoparticles were redispersed in Millipore water and the washing was repeated twice.

6.2.5 Labeling of chitosan with Alexa Fluor 790

4 mL of 0.5 wt % chitosan (0.5 wt % in 0.1 M NaAc) and 50 uL AF790 in DMSO were placed in an amber sample vial and allowed to react with stirring at room temperature for 3 h. Thereafter, the product was purified by ultrafiltration with a 100 K MWCO membrane. The product was washed twice with water followed by freeze drying. The final product was validated on ^{1}H-NMR and

spectrofluorometer. The dried polymer was stored at -20 °C for long term storage.

6.2.6 Conjugation of QDs to Heparin

0.0262 g EDC, 0.0390 g NHS, 0.2 g of heparin were allowed to react in MES buffer for 20 min. The mixture was then purified in Zeba desalting spin column to remove any excess reagents. The collected filtrate was added to a vial containing 0.4 g of QD710 in PBS. The reaction proceeded at room temperature for 2 h. The product was purified by ultrafiltration with a 10 K MWCO membrane, washed twice with water and freeze-dried. The final product was examined on a spectrofluorometer. The purified product was kept at 4 °C prior to use.

6.2.7 Layer-by-layer depositon on gold nanoparticle

TNF-α (10 μg/mL), chitosan (0.5 wt % in 0.1 M sodium acetate buffer) and heparin (1 wt % in water) were used as stock solutions for deposition. 5 μL of TNF-α was added to 1 mL of thiol-funtctionalized gold nanoparticles suspended in 10 mM NaCl. After 20 h adsorption, excess TNF--α in supernatant of centrifugation was removed. The nanocomplexes were redispersed in water and washing process repeated twice. 10 mM NaCl was then added to the nanocomplexes and the adsorption process was with the addition of 100 μL chitosan solution, followed by heparin, chitosan, and so on until a total of eight depositions were achieved. Each of the deposition steps was evaluated on the uv-visible spectrophotometer, zetasizer, and TEM.

6.2.8 WEHI 164 clone 13 fibrosarcoma *cell line (WEHI-13VAR) maintenance*

WEHI-13VAR was acquired from ATCC (Manassas, VA) were cultured in RPMI-1640 supplemented with 10% FBS, 1% penicillin/streptomycin. Subculture was performed at 1:5 to avoid exceeding 85 % cell confluence. AGS used in the experiments were between passages 6-8.

6.2.9 MTS cell viability assay

Cellular viability of the quantum dots were determined by [3-(4,5-dimethylthiazol-2-yl)-5-(3-carboxymethoxyphenyl)-2-(4-sulfophenyl)-2H-tetrazolium, inner salt] (MTS) assay (Promega, Fitchburg WI). WEHI-13VAR was seeded in 96-well plate at 20,000 cells per well and incubated overnight. On the day of testing, nanocomplexes containing rTNF-α were dispersed in RPMI-1640 containing 25 mM HEPES, 3 % FBS, and 0.5 μg/mL actinomycin (Sigma-Aldrich) were loaded into each well. After 20 h of incubation, culture media were removed from the wells and replaced with 100 μL of fresh culture medium. 20 μL of MTS stock solution was added to each well and the plate was subsequently incubated at 37 °C for 2 h before taking the absorbance on a microplate reader (BMG Labtech Fluostar Optima, Durham, NC) at 490 nm. Controls were cells that were incubated with culture medium.

6.2.10 Nanocomplexes characterization

Ultraviolet-visible spectra were measured by a double monochromator Shimadzu UV2501PC spectrophotometer equipped with a 50W halogen lamp and a D_2

lamp and using a 1.0 cm path length quartz cell. Zeta potential measurement was recorded on a Malvern Nano ZS Zetasizer. The size of the nanocomplexs were characterized using transmission electron microscope (TEM, FEI Tecnai G² Twin). Samples for TEM were prepared by putting a drop of suspension on carbon/formvar coated, 300-mesh copper grid.

6.2.11 Animal study

Animal use protocols were reviewed and approved by the Institutional Animal Care and Use Committee of Duke University. 4 weeks old female nude mice were purchased Charles River Laboratories and allowed to acclimate to the animal facility for at least 48 h. Thereafter, the animals were placed on adjusted vitamins diet (Harlan Laboratories, Madison, WI) 1 week prior to experimentation to eliminate fluorescent material usually found in standard rodent chow. For *in vivo* imaging, mice were anesthetized with isoflurane (2 % in oxygen) delivered from a precision vaporizer. 1 mL of nanocomplexes were concentrated by centrifugation and dispersed in 50 μL PBS. 20 μL of the nanocomplexes were administered in footpad. After each study, anesthetized mice were euthanized and the popiteal lymph nodes were collected for *ex vivo* imaging.

6.3 Results and Discussion

6.3.1 Synthesis of 10-mercaptodecanesulfonate sodium salt.

The reaction scheme for synthesis of 10-mercaptodecanesulfonate sodium salt is shown in Figure 37. In the first step of the reaction, the compound was verified by ^{1}H-NMR (Figure 38) and was confirmed to be 10-bromodecanesulfonic acid sodium salt (Yield = 11.51 g). The product from second step reaction was validated on ^{1}H-NMR (Figure 39) and was shown to be 10-S-thiouronium decanesulfonate (Yield = 6.32 g). The ^{1}H-NMR of the product from final step is depicted in Figure 40 and verified as 10-mercaptodecanesulfonate sodium salt (Yield = 5.83 g).

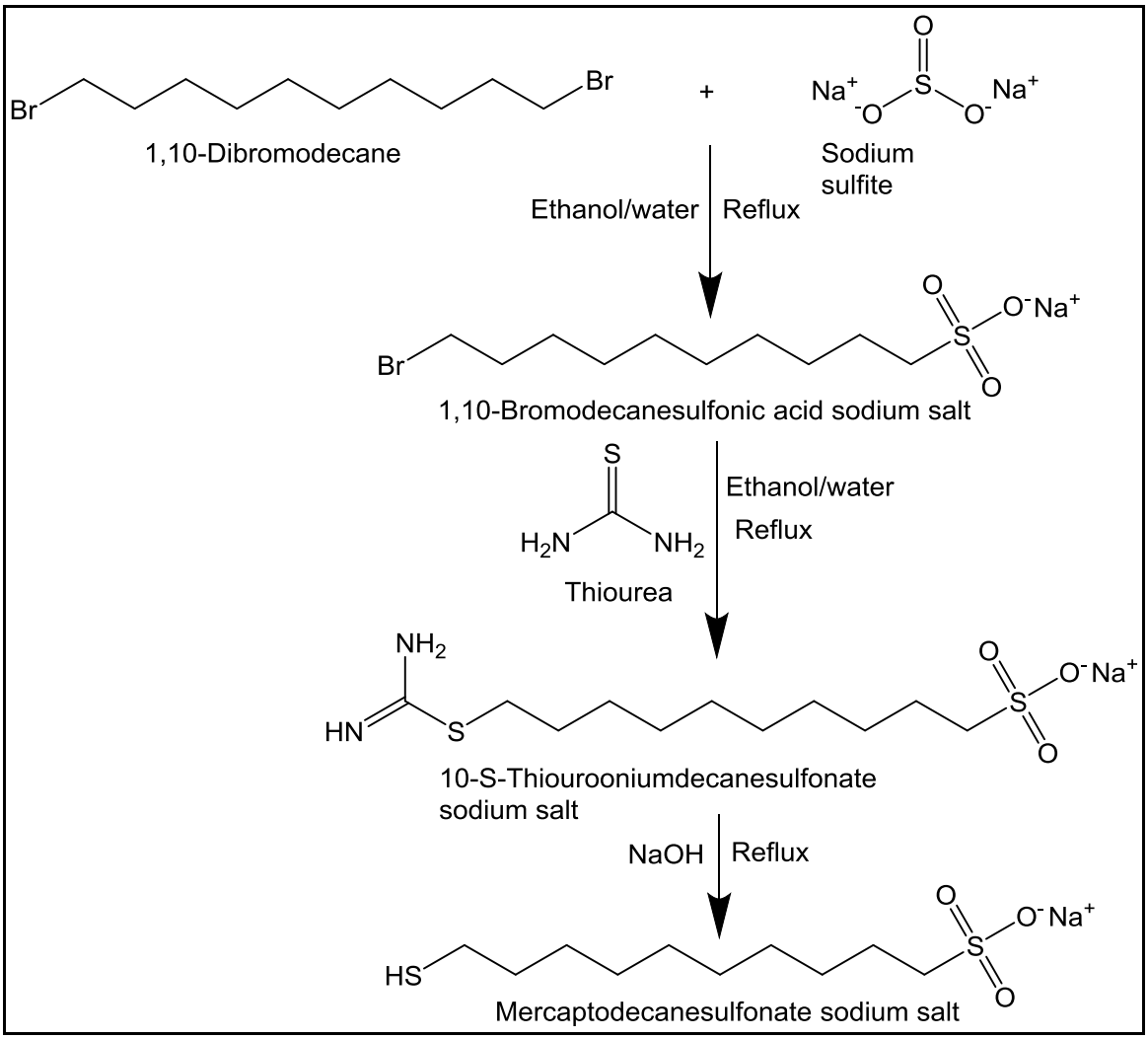

Figure 37. Reaction scheme for synthesis of 10-mercaptodecanesulfonate sodium salt.

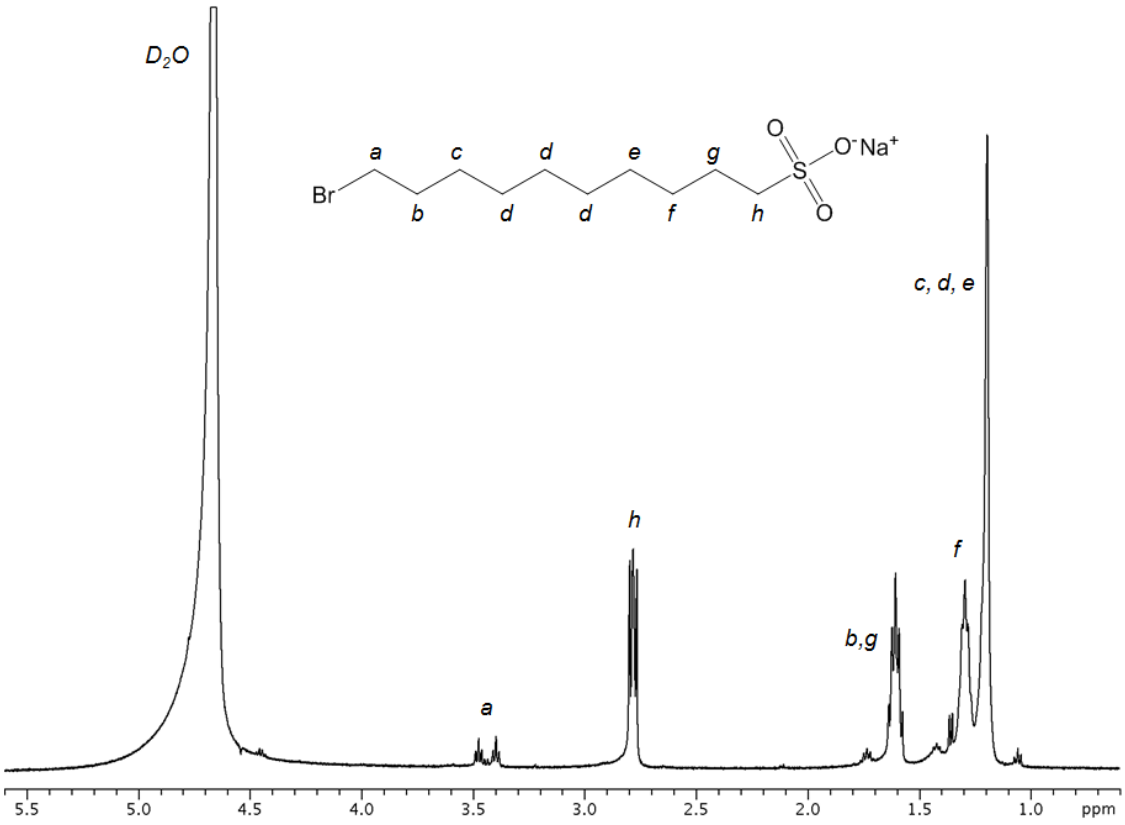

Figure 38. ^{1}H-NMR of 10-bromodecanesulfonic acid sodium salt.

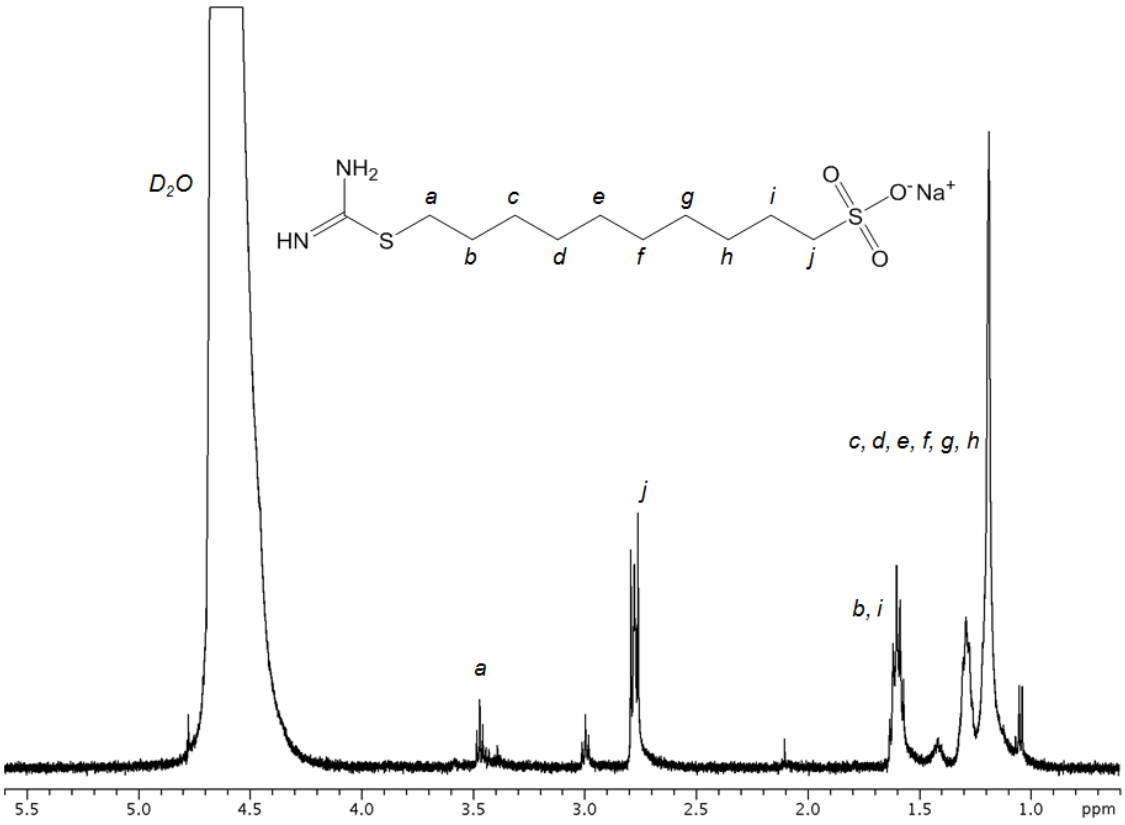

Figure 39. ^{1}H-NMR of 10-S-thiouronium decanesulfonate.

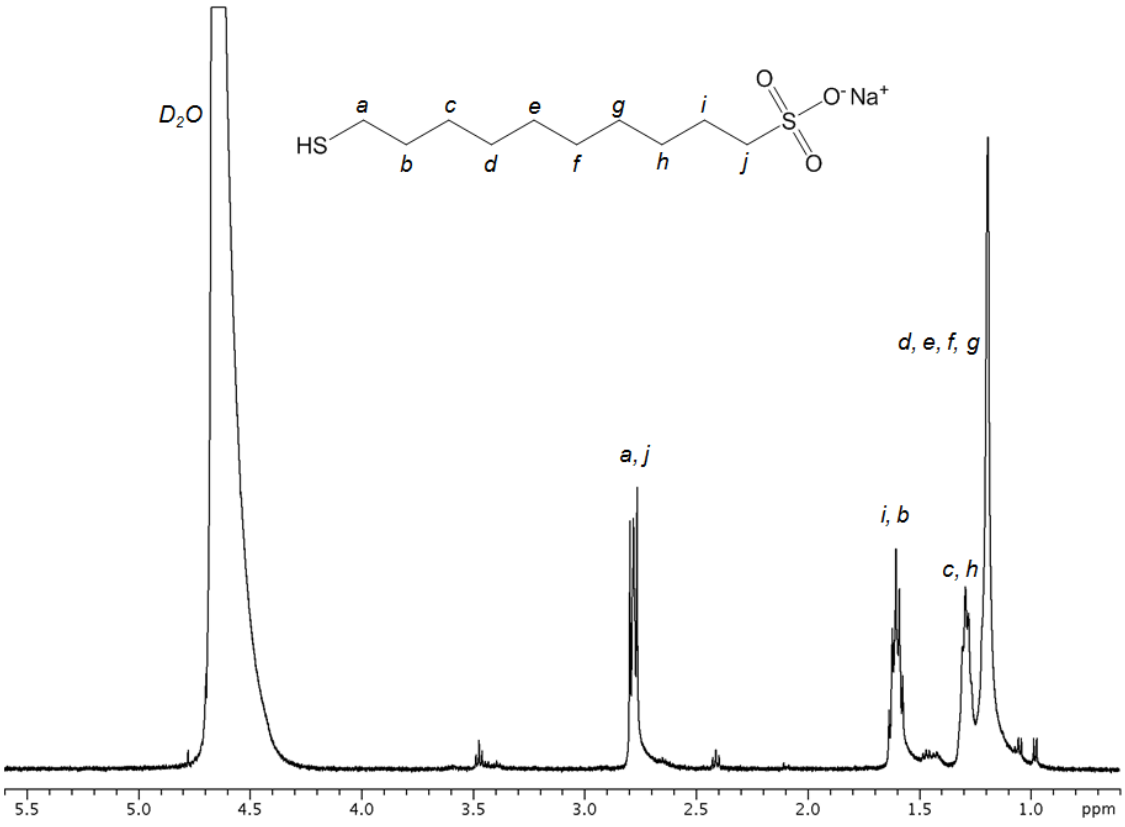

Figure 40. ^{1}H-NMR of 10-mercaptodecanesulfonate sodium salt.

6.3.2 Labeling of chitosan with Alexa Fluor 790

The reaction scheme for the conjugation of AlexaFluo 790 to chitosan is depicted in Figure 41. The exact chemical structure of AF790 is undisclosed by supplier; the only information provided is that it contains a succinimidyl ester readily react with primary amine group to form stable amide linkage. Figure 42 is ^{1}H-NMR of chitosan, which showed the peaks between 1-4.5 ppm corresponding to the proton on the sugar rings of chitosan. A close examination of the ^{1}H-NMR of AlexaFluo 790 (Figure 43) indicated that the dye contains several aromatic proton clearly in the range of 6.5-9 ppm. From the ^{1}H-NMR of chitosan-AlexaFluo 790 (Figure 44), we could find some peaks appearing in 6.5-9 ppm, clearly showing the inclusion of AlexaFluo 790 in chitosan. The absorbance and fluorescent spectra of AlexaFluo 790 and chitosan-AlexaFluo 790 are shown in Figure 45 and 46 respectively. There was no significant shift in the emission peak in the chitosan-AlexaFluo 790 sample, indicating there was no aggregation of the dye that would result in the quenching of the fluorescent signal.

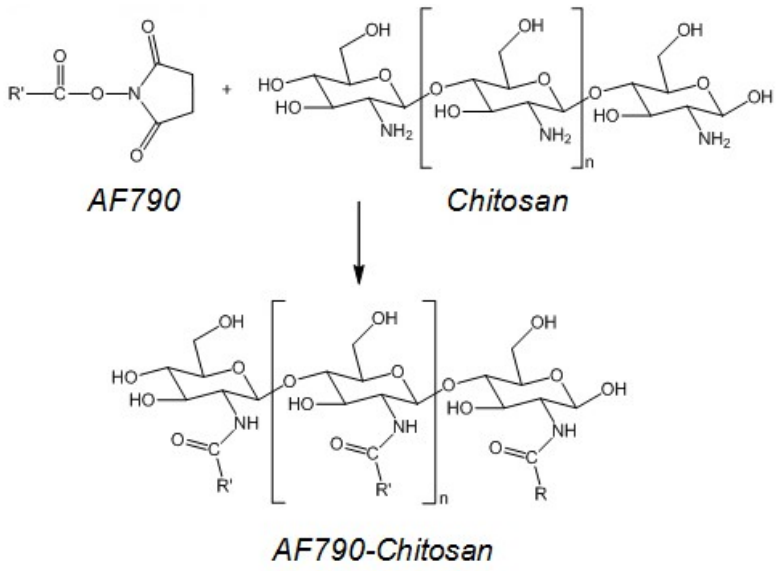

Figure 41. Schematic of comjugation of Alexa Fluor dye to chitosan via succinimidyl ester linkage to amine functional group.

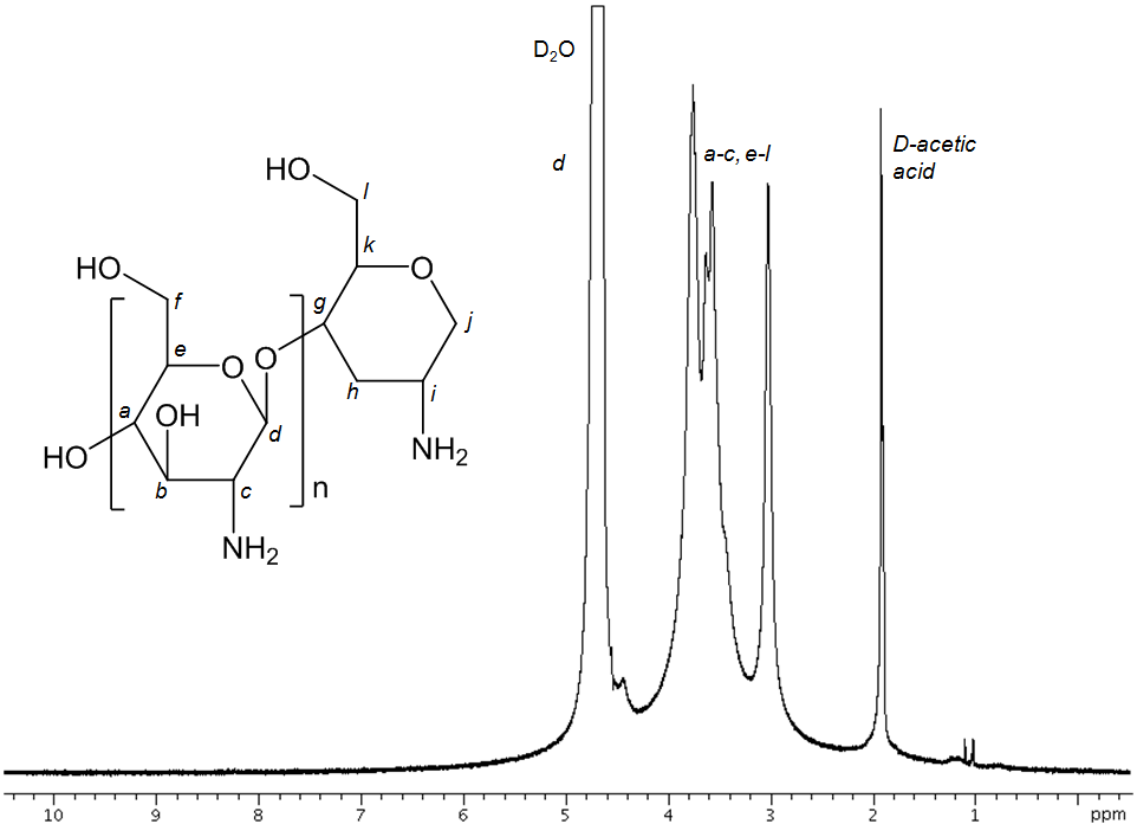

Figure 42. ^{1}H-NMR of chitosan.

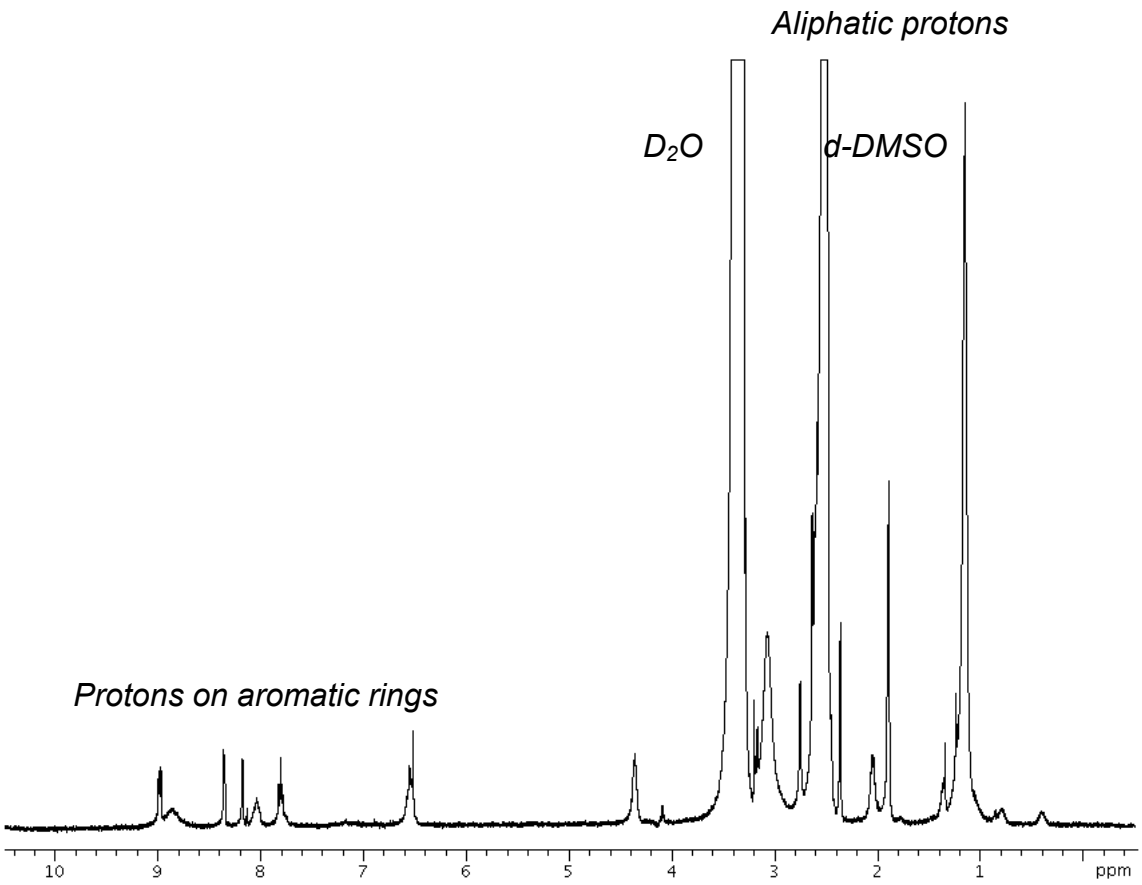

Figure 43. ^{1}H-NMR of AlexaFluo790.

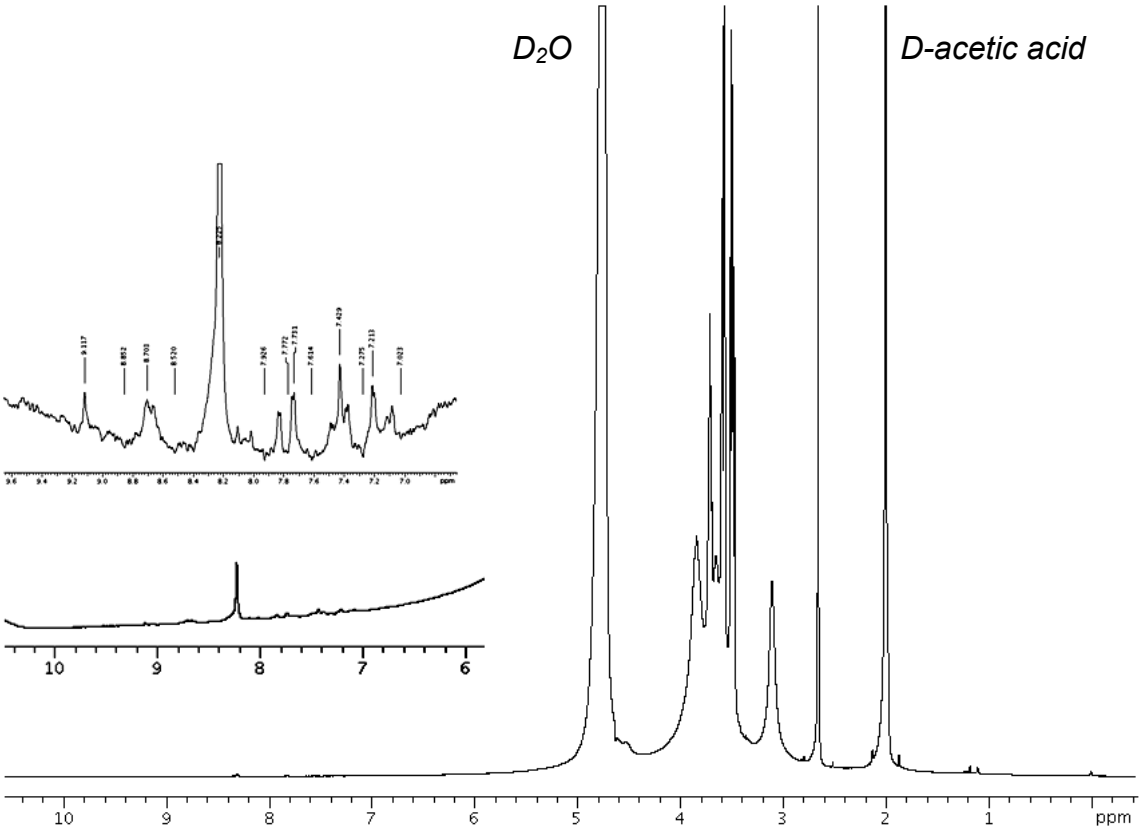

Figure 44. ^{1}H-NMR of chitosan-AlexaFluo790.

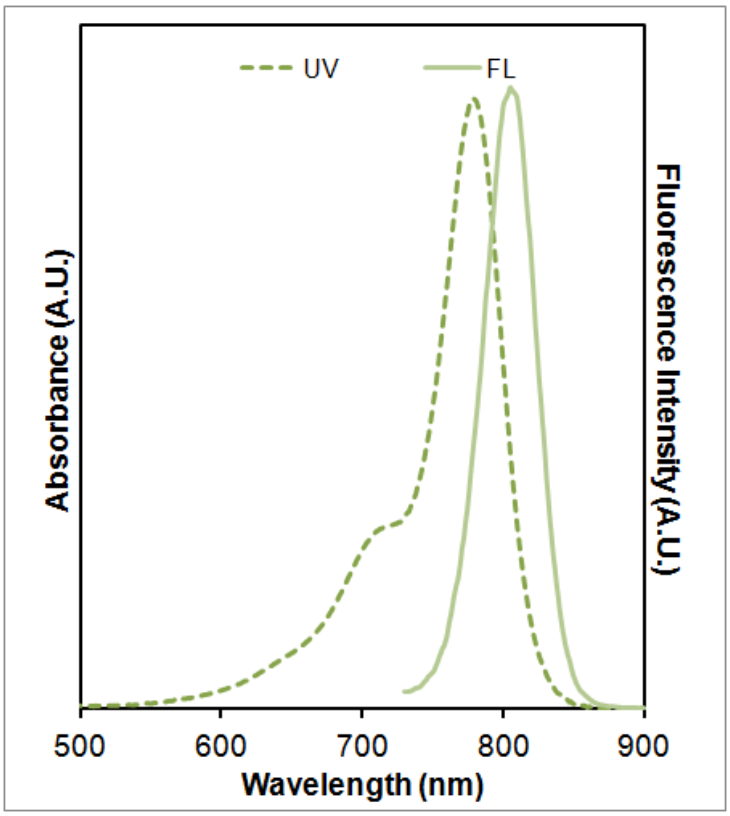

Figure 45. Absorption (⋯) and fluorescence (—) spectra of AlexaFluo 790 (λ_{ex} = 710 nm).

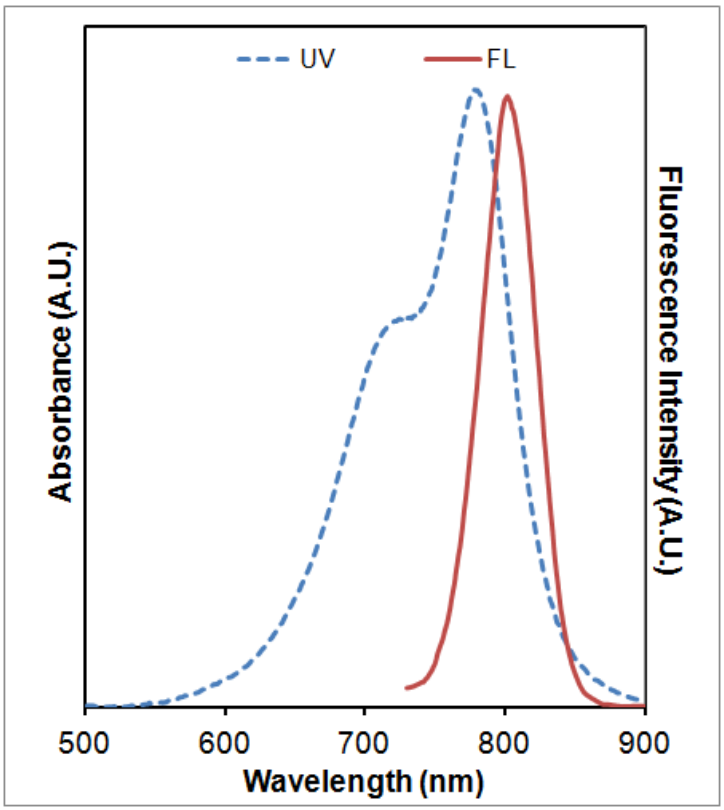

Figure 46. Absorption (⋯) and fluorescence (—) spectra of chitosan-AlexaFluo 790 (λ_{ex} = 710 nm).

6.3.3 Conjugation of QD710 to heparin

Conjugation of QD710 to heparin was perform via via two-step carbodiimide crosslinking procedures. (EDC) first activated carboxyl group on heparin to form an amine-reactive *O*-acylisourea intermediate. Since the reaction was performed at a pH of 5.5 in 2-(*N*-morpholino)ethanesulfonic acid **(**MES) buffer, the intermediate will be susceptible to hydrolysis, making it unstable and short-lived in aqueous solution (Staros *et al.* 1986). To improve the efficiency of the EDC coupling reaction, NHS was incorporated to react with the amine-reactive intermediate to form an amine-reactive-NHS ester. Thereafter, QD710

was introduced into the reaction to allow the amine functional group on glutathione to react to form the stable amide linkage between QD710 and heparin (Figure 47). The fluorescence spectrum of heparin was shown in Figure 48. Since the length of heparin is ~ 9 nm (Murugesan *et al.* 2008), multiple heparin molecules could possibly attached to the surface of QDs. The observed shift in the emission spectrum might be the result of several heparin molecules conjugated to QDs thus leading to an increase in the overall size of the QDs.

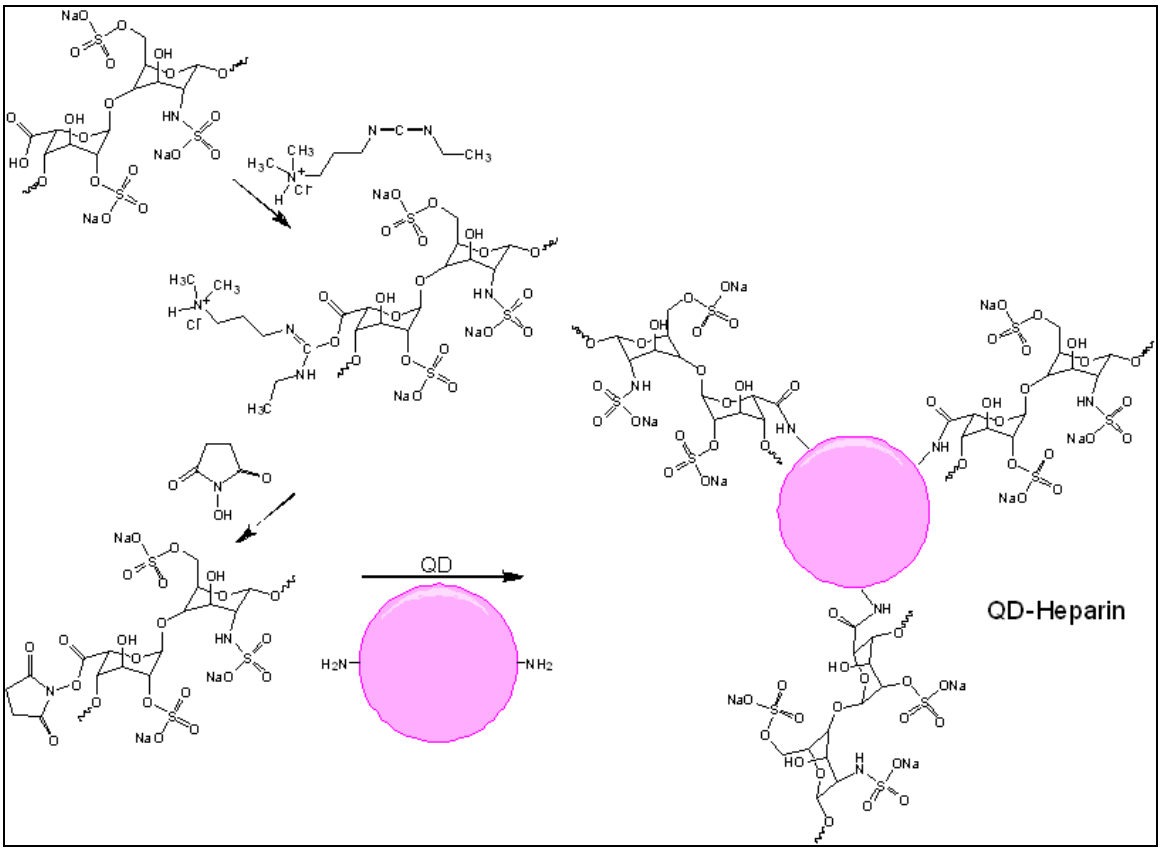

Figure 47. Schematic of conjugation of quantum dots to heparin via a two-step carbodiimide reaction.

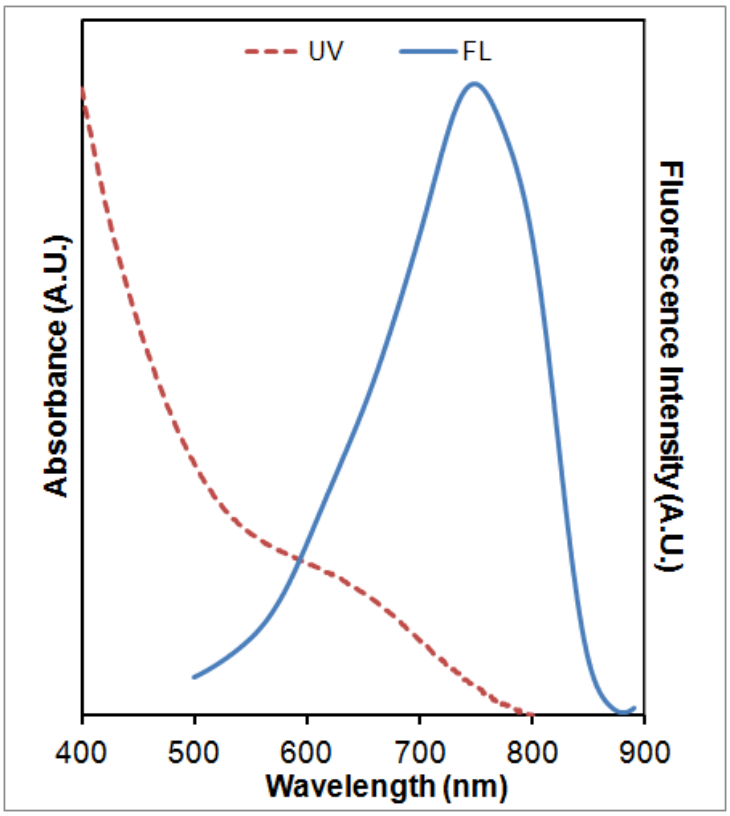

Figure 48. Absorption (⋯) and fluorescence (—) spectra of QD710-Heparin.

6.3.4 Layer-by-layer depositon on gold nanoparticle (Au NP)

The creation and design of nanocarriers for drug delivery are of great interest because of their possible clinical applications. With optimized formulation, therapeutic nanocarriers could effectively deliver cargos to targeted cells and tissues, potentially reducing side effects and drug dose to achieve therapeutic benefits. One method of preparation of encapsulated nanocarriers is by random self-assembled aggregates of polyelectrolytes with therapeutic agents, resulting in large particles of heterogenous sizes (> 100 nm) (Neu *et al.* 2005; Pozharski *et al.* 2007). For lymphatic delivery purposes the ideal particle size is 10-80 nm, particles > 100 nm will remain largely at the injection site (Nune

et al. 2011). Alternative method that could circumvent the limitations of previous system is a layer-by-layer (LbL) approach that makes use of monodisperse gold nanoparticles (Au NPs) as template for assembly and delivery of cargos.

LbL sequential deposition of oppositely charged polyelectrolytes is a well-established technique for thin films formation on flat surfaces and microparticles (Gittins *et al.* 2001). Its application to nanoparticles of diameter < 100 nm is limited because of issues such as aggregation arising from the crosslinking of the particles by the polyelectrolyte chains and removal of unbound polyelectrolytes from the coating (Mayya *et al.* 2003; Schneider *et al.* 2008).

We present here a simple approach to optimizing the experimental parameters for depositions of TNF-α and with QD-labeled polyanions on 20 nm Au NPs for *in vivo* delivery to the draining lymph nodes. The schematic for layer-by-layer deposition on gold nanoparticles is depicted in Figure 49 (Elbakry *et al.* 2009). Direct complexation on citrate-stabilized Au NPs was unstable due to that the citrate ions are only physical bound to the surface of Au and the polymer will eventually desorbed from the Au NPs surface. In order to successfully introduce coating on Au, a thiol ligand has to be used to replace the citrate ion to form stable chemical bond with Au. At the same time, the free end on the thiol group must contain ionic functionality for interaction with polyelectrolytes. 10-mercaptodecanesulfonic acid sodium salt (MDS) was used for the ligand exchange step. After the ligand exchange, polyelectrolytes of opposite charge were introduced and so on. We first investigated the optimized conditions for the coating by studying the effect of the concentration of MDS (Figure 50).

Absorbance spectra were collected as an indication to the change of the coated surface. The plasmonic absorption peaks are summarized in Table 6. From this experiment we found that 10 mg of MDS added to 1 mL of Au NPs would cause 2 nm shift in the band peak, higher MDS will cause larger shift. Subsequent coating Au NPs with MDS was kept at 10 mg/mL.

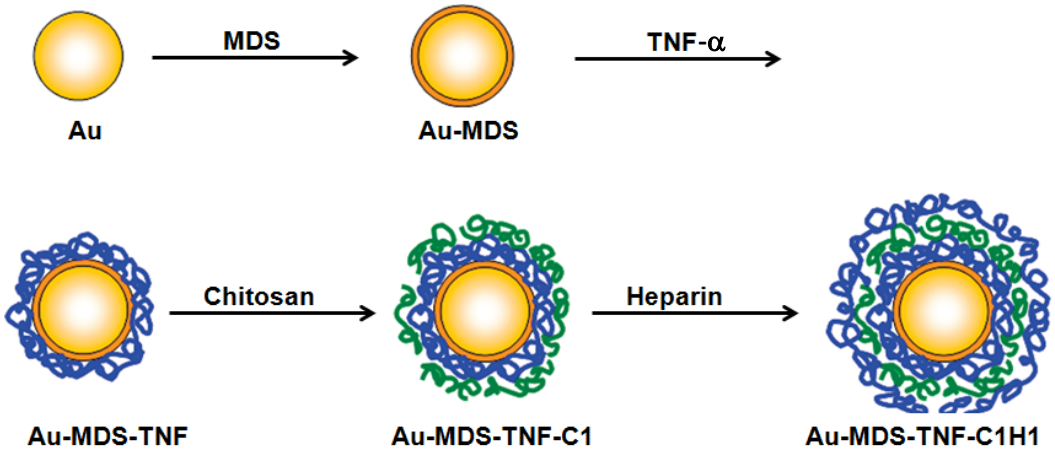

Figure 49. Schematic of layer-by-layer coating on Au nanoparticles.

Next, we continued to explore the concentration of salt that will cause minimal aggregation in the system. Figure 51 is the absorbance spectra and Table 7 is the summary of the Plasmon band peak of Au in various NaCl concentration. From the results we found that 10 mM of NaCl would be ideal to avoid inducing aggregation of the Au NPs. In our study, we have included zeta potential measurement as indicators to polyelectrolyes interaction. A reversal of the zeta potential after completion of each coating signified the deposition of each polyelectrolyte. The zeta potential measurements for each layer of coating are presented in Appendix J, the results are summarized in Table 8 and a plot is

provided as illustration of inversion of surface charge after each successive coating (Figure 52). The UV plasmon band shift was recorded and summarized in Figure 53. It is shown that coating with TNF-α did not cause an increase in overall size of the Au NP which is in agreement with what we observed in the TEM (Figure 53). In fact, coating with TNF-α provided spatial separation in the NPs. However, once first layer chitosan coating was introduced, we saw a shift of ~25 nm in the uv plasmon band, indicating there was probably an increase in particle size or aggregation of the particles. We validated on TEM and concluded that the coating layer caused an overall increase in size of the nanocomplexes by ~4 nm and at the same time induced some aggregation in the system. Subsequent coating with heparin further shifted the plasmon band by ~5 nm but we did not see any drastic increase in overall size of nanocomplexes (Figure 54). From the TEM, we observed the particles started to aggregate slightly that probably was the reason for the plasmon band shift. We next introduced another layer of chitosan coating to the particles and observed that second layer of chitosan coating only caused 1 nm shift in plasmon band. Again, we did not observe any increase in overall size of the Au NPs. However, we did see similar aggregation patterns as in the heparin coating. As so, the coating was stopped after second layer of chitosan was introduced on the nanocomplexes. These nanocomplexes formulation was used for the cell viability assessment and animal testing experiments.

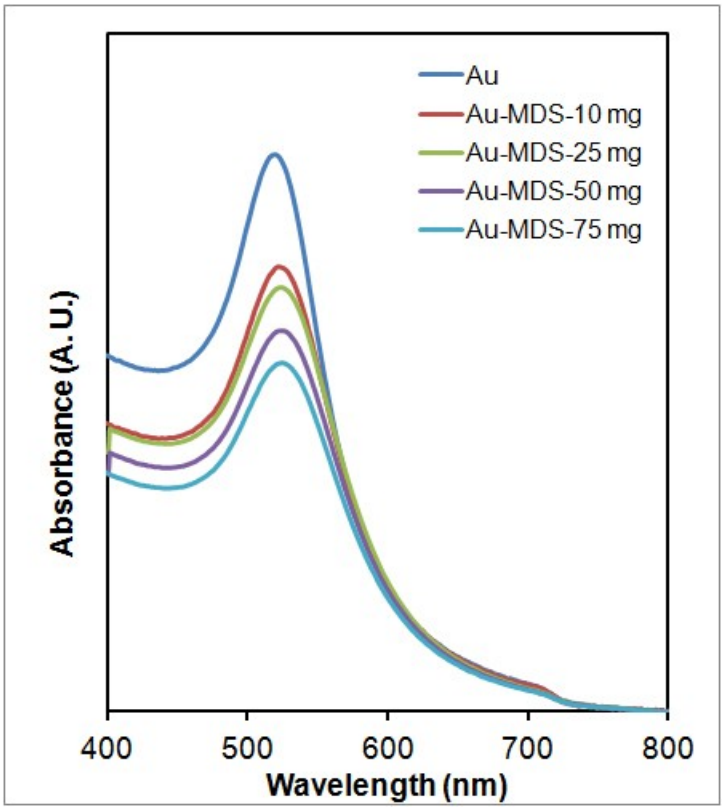

Figure 50. Absorbance spectra of Au NP coated with different concentration of MDS.

Table 6. Plasmon band peak of MDS Coating

Sample	Plasmon band peak absorption (nm)
Au	520
Au-MDS-10 mg	522
Au-MDS-25 mg	525
Au-MDS-50 mg	525
Au-MDS-75 mg	525

Table 7. Plasmon band peak with varying concentration of NaCl

Sample	Abs (nm)
Au	520
Au-MDS-10 mg	522
Au-MDS-1 mM NaCl	522
Au-MDS-10 mM NaCl	522
Au-MDS-25 mM NaCl	522
Au-MDS-50 mM NaCl	522
Au-MDS-75 mM NaCl	526
Au-MDS-100 mM NaCl	530

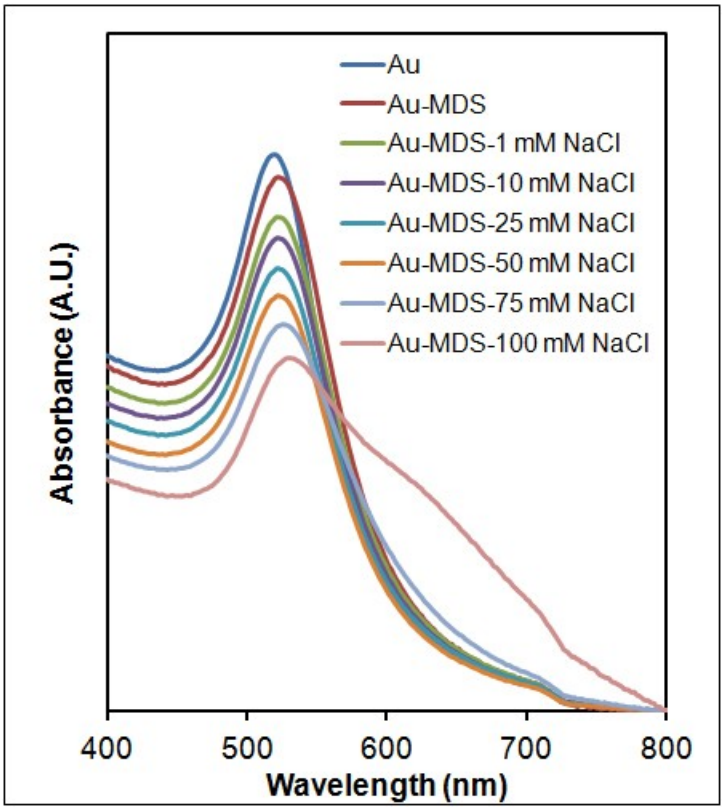

Figure 51. Absorbance spectra of Au NP in different concentration of NaCl.

Table 8. Summary of zeta potential and plasmon band peak of each layer of coating

Sample	Zeta Potential (mV)	Abs (nm)
Au NP		520
Au-MDS	-53.00 ± 1.37	522
Au-MDS-TNF	-20.60 ± 1.42	524
Au-MDS-TNF-C1	+44.24 ± 0.81	549
Au-MDS-TNF-C1H1	-44.18 ± 0.48	554
Au-MDS-TNF-C2H1	+48.80 ± 0.77	555
Au-MDS-TNF-C1Heparin-QD710	-25.08 ± 0.78	-
Au-MDS-TNF-C2Heparin-QD710	+31.84 ± 1.35	-

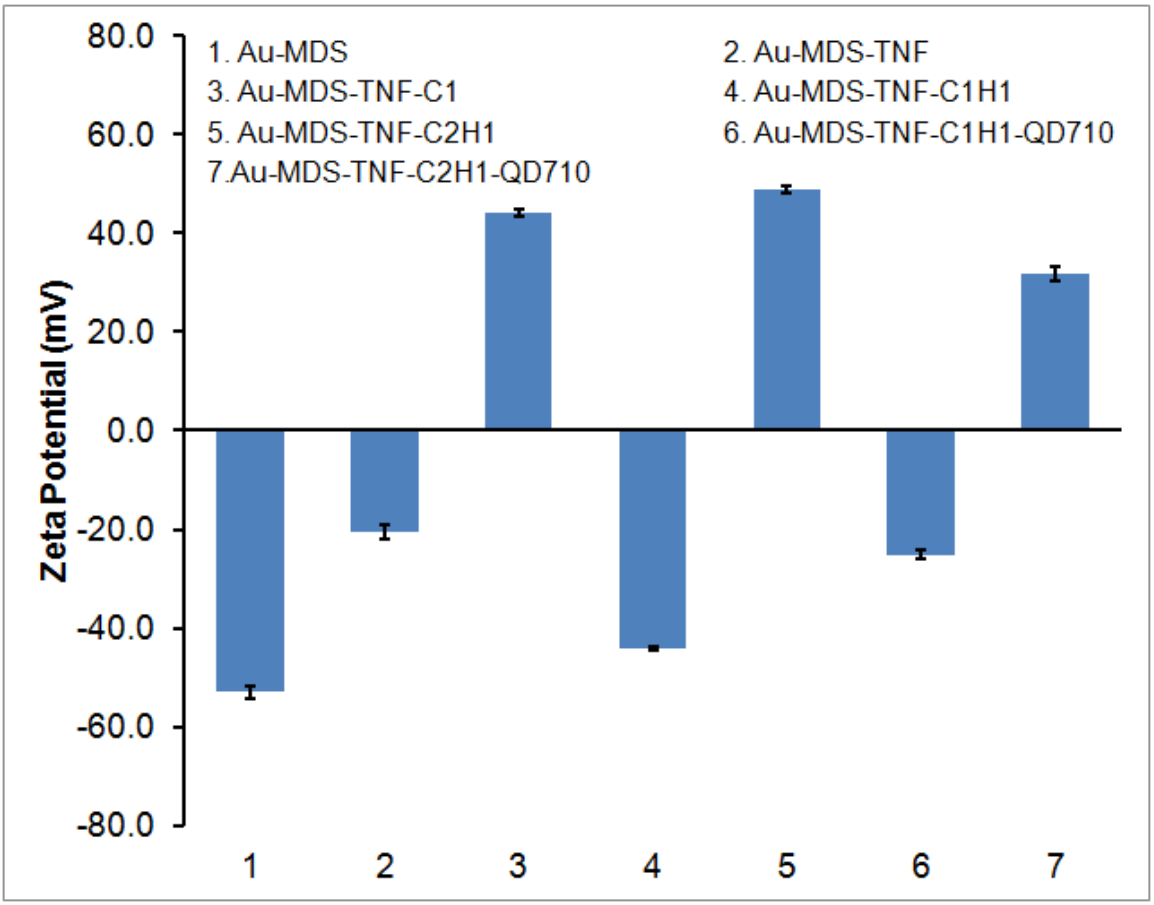

Figure 52. Zeta potential measurement of layer-by-layer nanocomplexes.

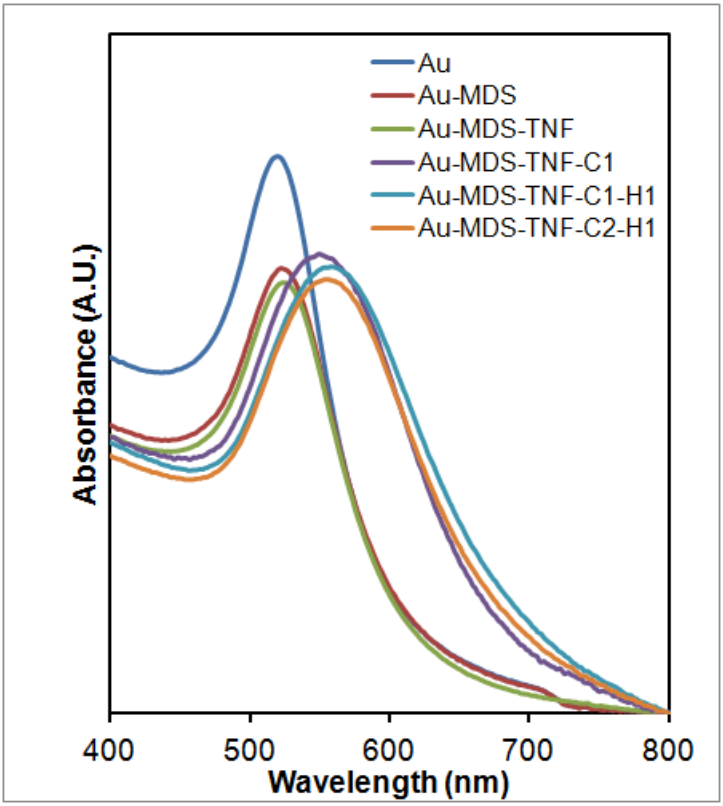

Figure 53. Absorbance spectra of Au NP coated with chitosan and heparin.

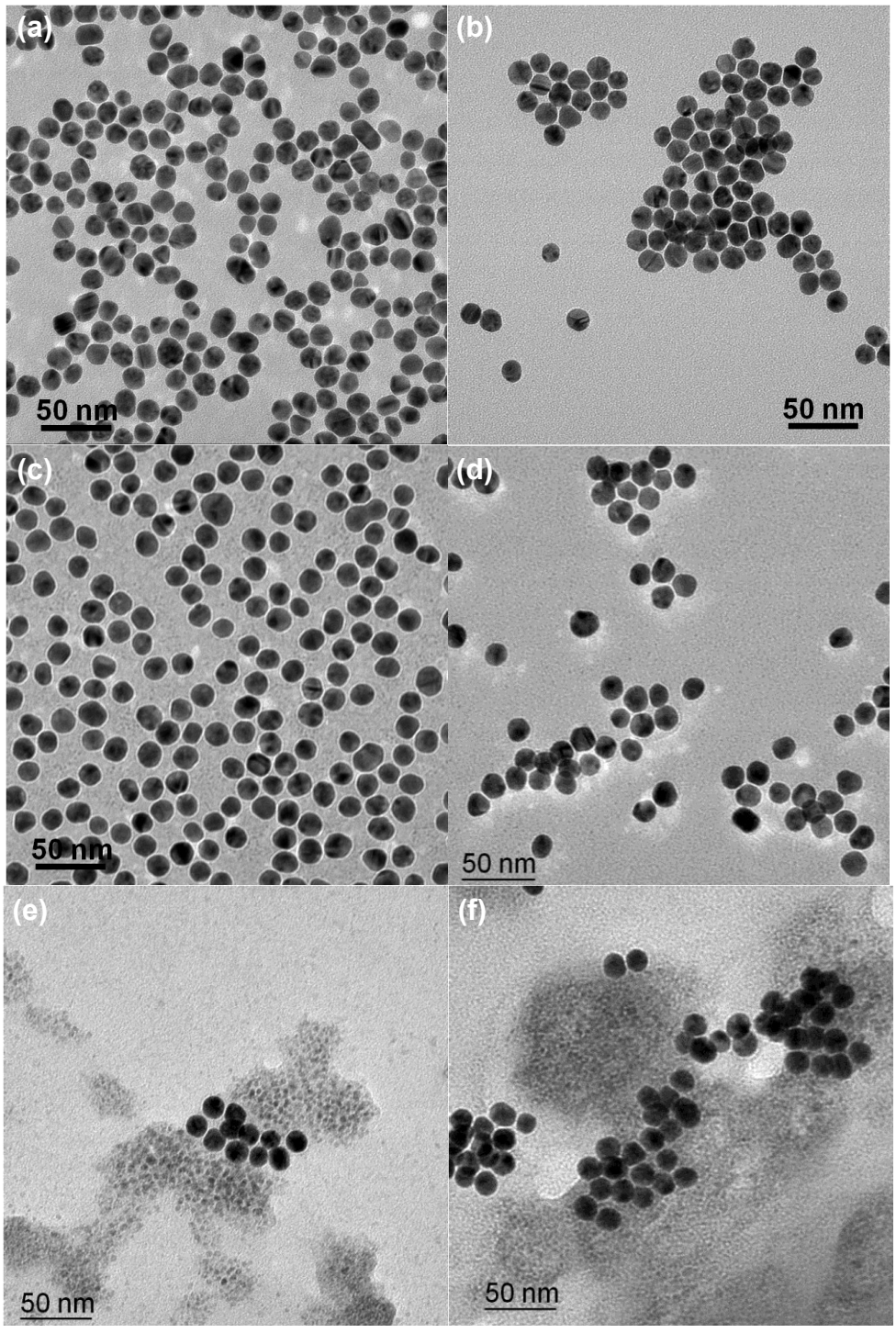

Figure 54. TEM of (a) Au NP; (b) Au-MDS; (c) Au-MDS-TNF; (d) Au-MDS-TNF-C1. (e) Au-MDS-TNF-C1H1. (f) Au-MDS-TNF-C2H1.

6.3.5. Cell viability and animal testing

WEHI-13VAR is a stable variant of WEHI 164 clone 13 fibrosarcoma that is sensitive towards TNF-α (Espevik *et al.* 1986,Khabar, 1995 #11). Here, we used WEHI-13VAR for our cytotoxicity analysis of the encapsulated TNF-α in the nanocomplexes. We first generated a calibration curve for a series of TNF-α concentration. We performed MTS assay to assess the amount of TNF-α coated on Au NPs against the standard curve (Figure 55). From Figure 56, we found that the amount of TNF-α coated on Au-MDS-TNF was about 0.1 % of the feed concentration regardless of the feed concentrations (Table 9). This could possibly be due to the limitation of the surface area and surface ligand available for the TNF-α complexation to take place. We further conducted the evaluation of the release of TNF-α from the nanocomplexes with different layers of coating (Figure 57). We saw an increase inhibition of the release of TNF-α as the number of layers of coating increases. The polyelectrolytes layers could partially prevent the release of TNF-α but not totally inhibiting the crossing out from the nanocomplexes. When Au-MDS-TNF-C2H1 nanocomplexes were subjected to incubation with chitosanse at a concentration of 2 U/mL for 2 h, the nanocomplexes degraded and release all the TNF-α coated on the Au NPs. At the same time, we did a control test to treat the WEHI-13VAR cells with 2 U/mL of chitosanase and found that it has no toxicity effect on the cells. Similarly, no toxicity effect was also detected for cells treated with Au-MDS.

We next conducted a preliminary testing by administering Au-MDS-TNF, Au-MDS-TNF-C1 and Au-MDS-TNF-C1H1 nanocomplexes in the footpad of nude mice and isolated the popiteal lymph node 24 h post injection. We found that we could only visualize the red color of the Au nanocomplexes with the series of mice treated with Au-MDS-TNF but not with the other nanocomplexes (Figure 58). On the contrary, brightfield images of the cryo-sectioned of the lymph nodes further indicated that Au-MDS-TNF nanocomplexes were densely observed in the sinusoids of the lymph nodes (Figure 59b) but only traces of the particles can be found the samples treated with Au-MDS and Au-MDS-TNF-C1 (Figure 59 a and c). The absence of Au-MDS-TNF-C1H1 in the lymph nodes probably mean that the nanocomplexes either could not reach the lymph nodes or they were totally dispersed in the lymph nodes such that they were too sparse to be detected here. Interestingly, we did not notice any significant enlargement in the treated lymph nodes (Table 10).

Prior to conducting the *in vivo* imaging we performed a screening of the QD710-labeled heparin and also AlexaFluo 790-labeled chitosan to evaluate the fluorescent signals with various filters available on the IVIS system. As illustrated in Figure 60, it was shown QD-labeled heparin can be excited with 570-710 nm source and the signal can be recorded using with Cy5.5 and ICG filters. On the other hand, AlexaFluo 790-chitosan can only be excited using 640-710 nm source and the signal can only be captured with ICG filter.

Subsequently we continued to *in vivo* testing on the IVIS system to track the fluorescent signals of series nanocomplexes. We injected nanocomplexes

that were coated with QD-labeled heparin (Au-MDS-TNF-C2-HepQD710) and AlexaFluo 790-labled chitosan (Au-MDS-TNF-C1-HepQD710-ChitAF790). We included commercial QD800-NH_2 in this study as positive control (Figure 61). We monitored the animals are different time points and the images are as in Figure 62 and 63. We first started to observe fluorescent signal of QD800-NH_2 in the popiteal lymph node region at 40 min but not for the animals tested with nanocomplexes. At 90 min post-injection we started to see a decrease in the fluorescent signal by almost half in the footpad for the mice treated with nanocomplexes. However, we did not see any signal near the popiteal lymph nodes region and we no longer can detect any signal 24 h post-injection. We isolated the popiteal lymph nodes and did an *ex vivo* imaging on it. We found slight traces of fluorescent signal but it was very much lower than the signal at the start of the experiment. We speculate that some of the nanocomplexes traversed through the lymphatic vessels and accumulated at the popiteal lymph nodes 24 h post treatment. However, since nude mice lack of T-cells we are unclear if this could attribute to dictate the route of delivery of these nanocomplexes. Other possible explanations could be that the nanocomplexes might have being degraded by heparinase present in the body of the mice when the nanocomplexes traverse to the lymph nodes or the nanocomplexes have traveled further to other lymph nodes and we could detect the signal due to dilution.

In addition, to address if the nanocomplexes remained intact while being delivered to the lymph nodes, we carried out an *ex vivo* fluorescence resonance

energy transfer (FRET) analysis on the lymph nodes that were isolated from mice treated with Au-MDS-TNF-C1-HepQD710-ChitAF790 nanocomplexes. FRET is a distance-dependent interaction between the excited states of two fluorescent molecules whereby excitation from donor molecule is transferred to acceptor molecule without emission of a photon. In our current study, QD710 and AlexFluo 790 are the donor and acceptor molecules respectively. As depicted in Figure 64, if the nanocomplexes are stable while being delivered to the lymph nodes, we will expect to be able to record the fluorescent signal of AlexaFluo 790 only with ICG filter when excited with 570 or 605 nm source. When excited with 570 or 605 nm source fluorescent signal from QD710 can be detected using either Cy5.5 or ICG filter if the nanocomplexes degraded. Presented in Figure 65 are the results of the analysis of the lymph nodes using different excitation/emission filter sets. As shown (a) and (c), traces of fluorescent signals were observed with both 605/ICG and 570/ICG filters but no fluorescent signal was recorded on 605/Cy5.5 and 570/Cy5.5 filters. This probably suggests that the nanocomplexes still remain intact 24 h post-injection and were delivered to the lymph nodes. Nevertheless, the signal recorded after 24 h was lower than at the start of the experiment, more detailed experiments are needed to determine the fraction of nanocomplexes were delivered and also to address if it is possible that the nanocomplexes have traversed to other lymph nodes.

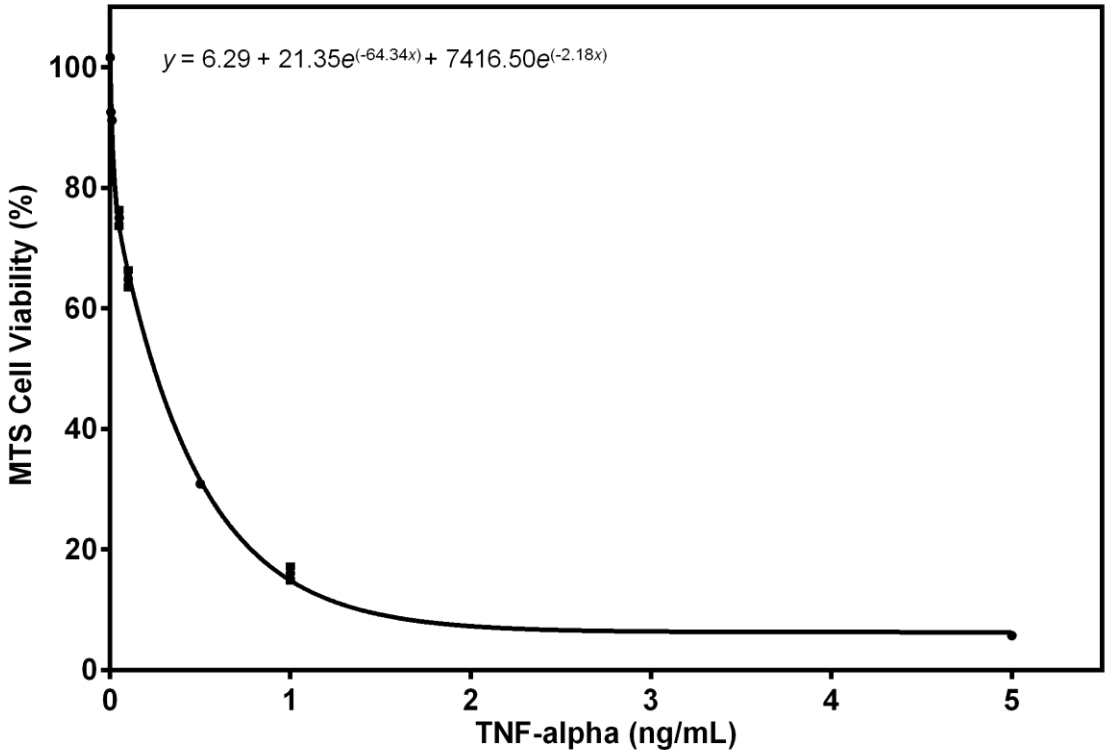

Figure 55. Standard calibration curve of cell viability of WEHI-13VAR cells with dose of TNF-α.

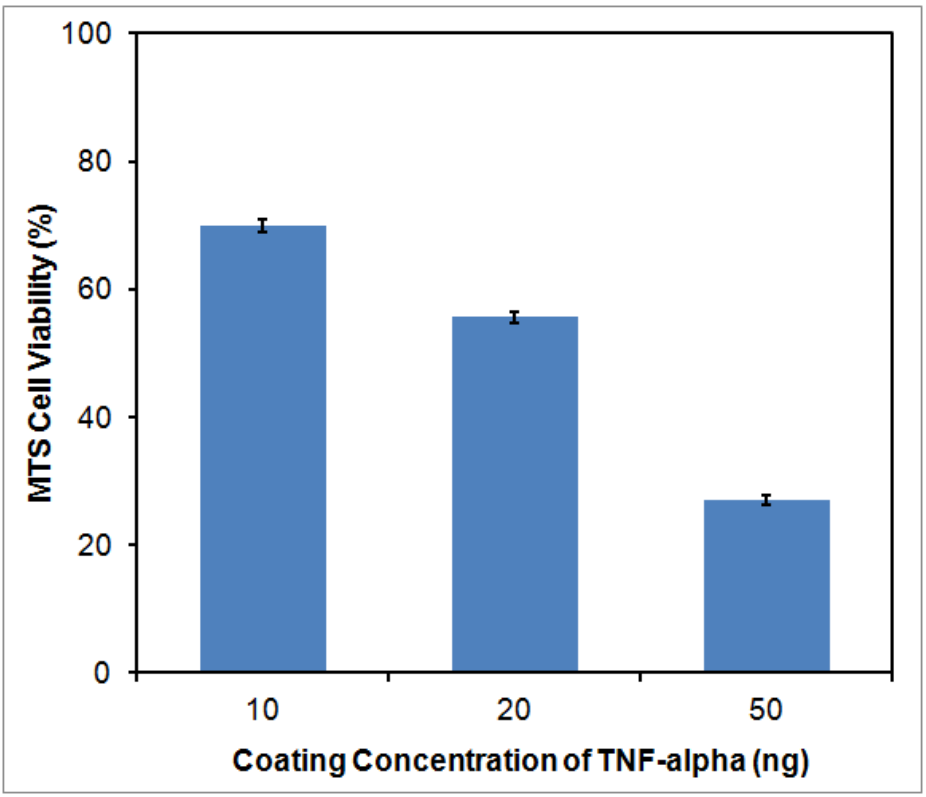

Figure 56. MTS cell viability of Au-MDS coated with different amount of TNF-α.

Table 9. Estimated amount of coating of TNF-α on 1 mL of Au NPs

Feed Coating Concentration (ng)	Calculated Coating Concentration (ng)
10	0.062
20	0.064
50	0.069

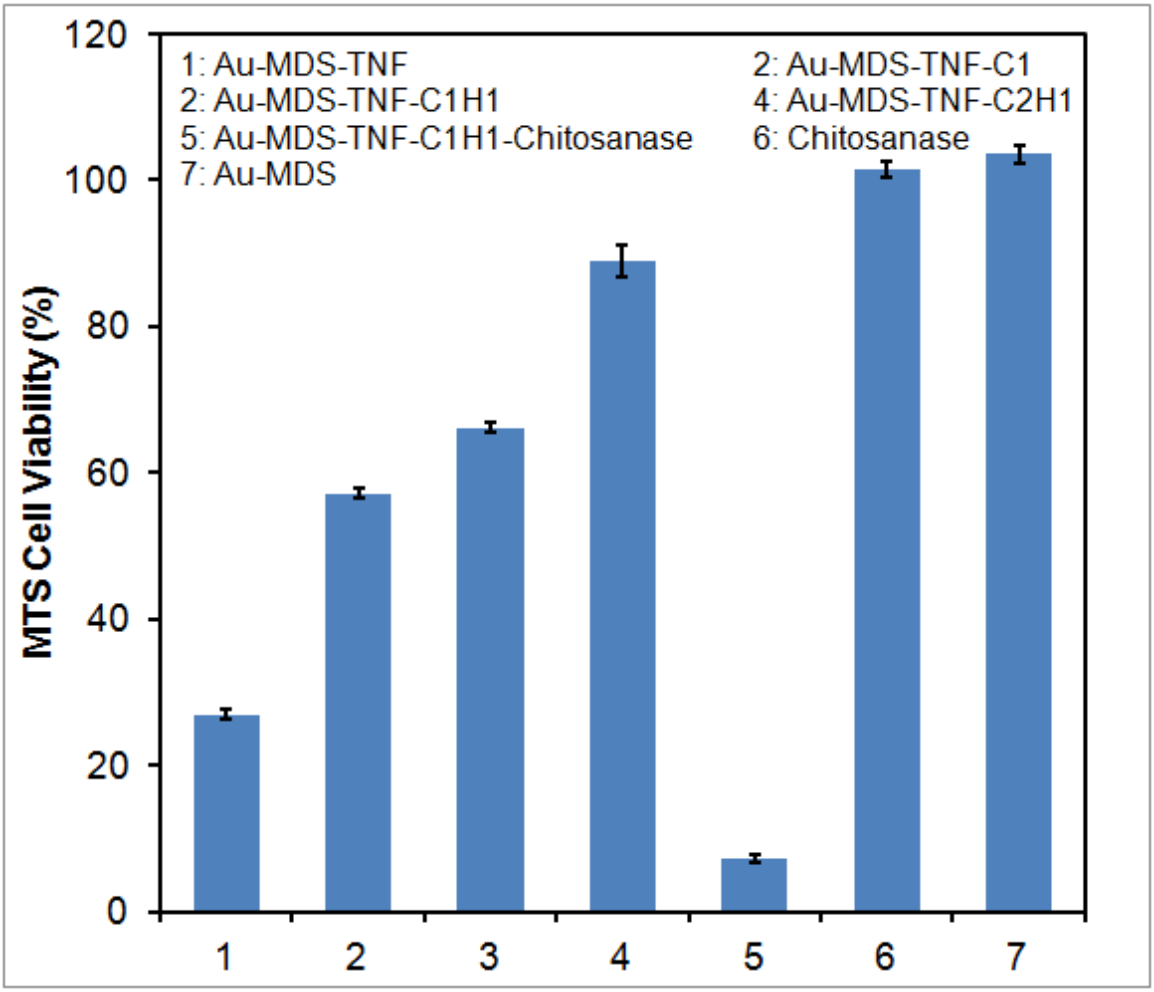

Figure 57. MTS cell viability of WEHI-13VAR cells treated with nanocomplexes with different coating.

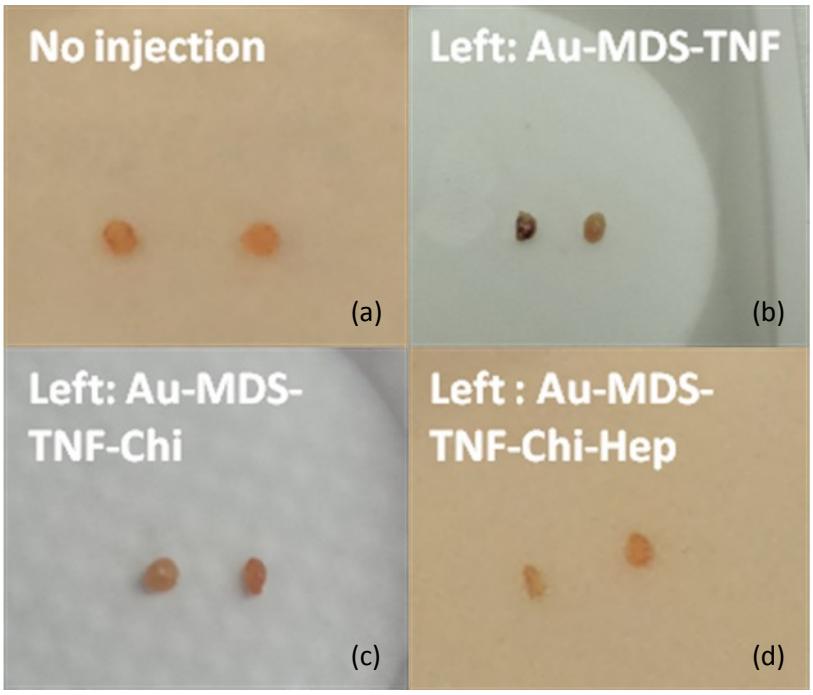

Figure 58. Popiteal lymph nodes of mice treated with nanocomplexes. (a) Control. (b) Au-MDS-TNF. (c) Au-MDS-TNF-C1. (d) Au-MDS-TNF-C1H1.

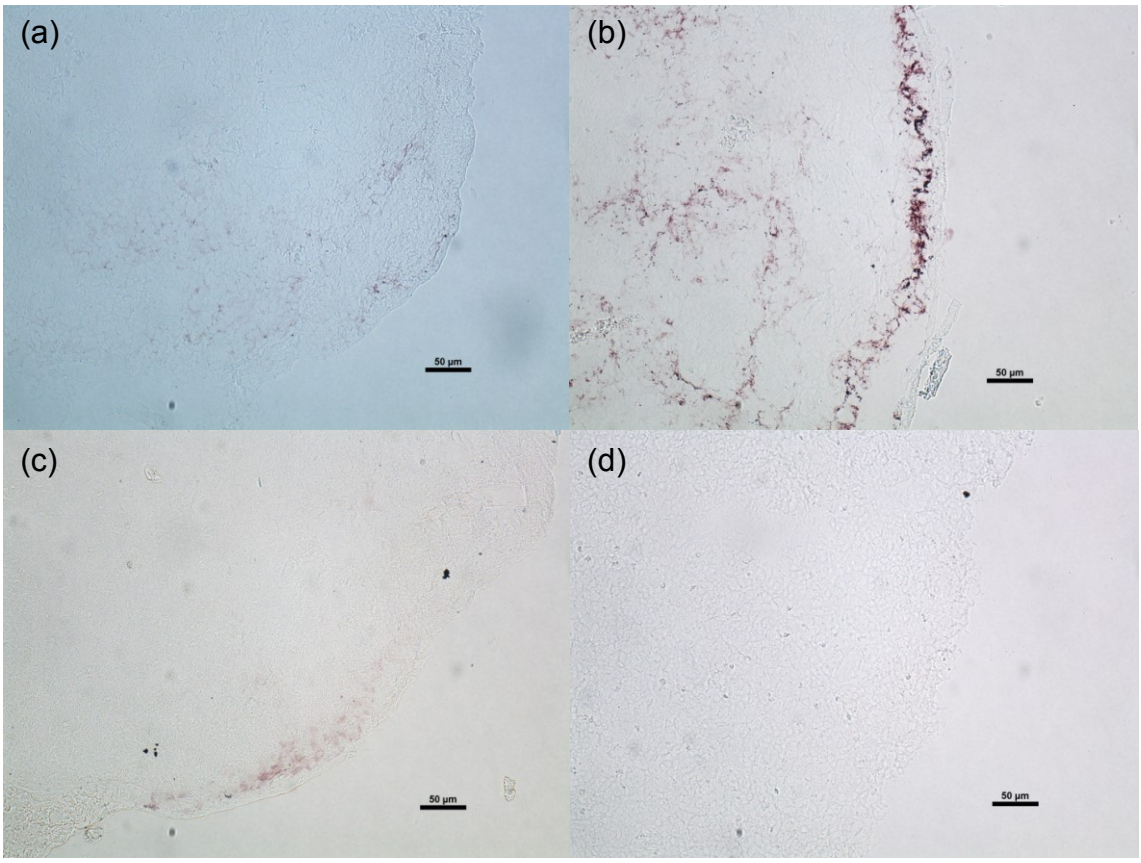

Figure 59. Brightfield images of cryo-sectioned of popiteal lymph nodes of mice treated with nanocomplexes. (a) Au-MDS. (b) Au-MDS-TNF. (c) Au-MDS-TNF-C1. (d) Au-MDS-TNF-C1H1.

Table 10. Mass of lymph nodes treated with nanocomplexes

Sample	Treated (mg)	Untreated (mg)
No injection	2.1	2.3
Au-MDS	2.0	2.1
Au-MDS-TNF-1	2.6	3.1
Au-MDS-TNF-2	3.2	2.3
Au-MDS-TNF-3	2.1	1.4
Au-MDS-TNF-Chitosan-1	2.8	2.7
Au-MDS-TNF-Chitosan-2	3.6	2.1
Au-MDS-TNF-Chitosan-Heparin-1	1.3	1.6
Au-MDS-TNF-Chitosan-Heparin-2	1.5	1.1
Au-MDS-TNF-Chitosan-Heparin-3	2.2	2.3

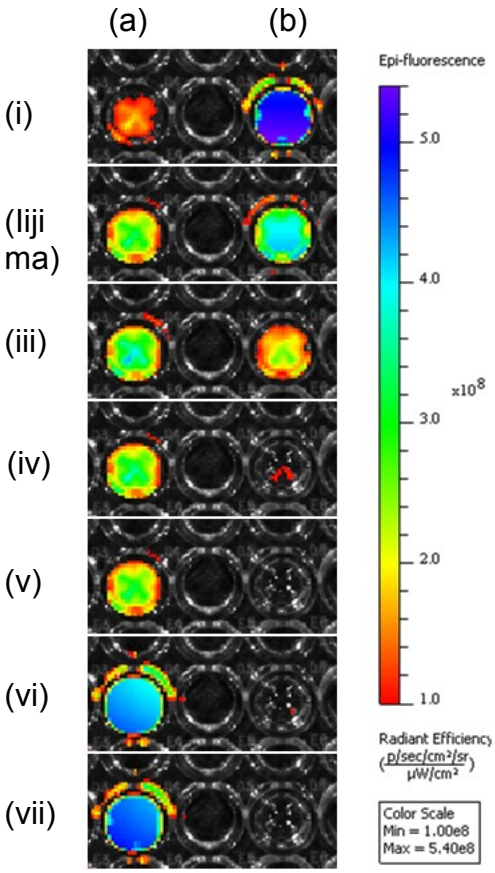

Figure 60. Imaging of (a) QD710-heparin and (b) AlexaFluo790-chitisan with different excitation/emission filter. (i) 710/ICG; (ii) 675/ICG; (iii) 640/ICG; (iv) 605/ICG; (v) 570/ICG; (vi) 605/Cy5.5; (vii) 570/Cy5.5.

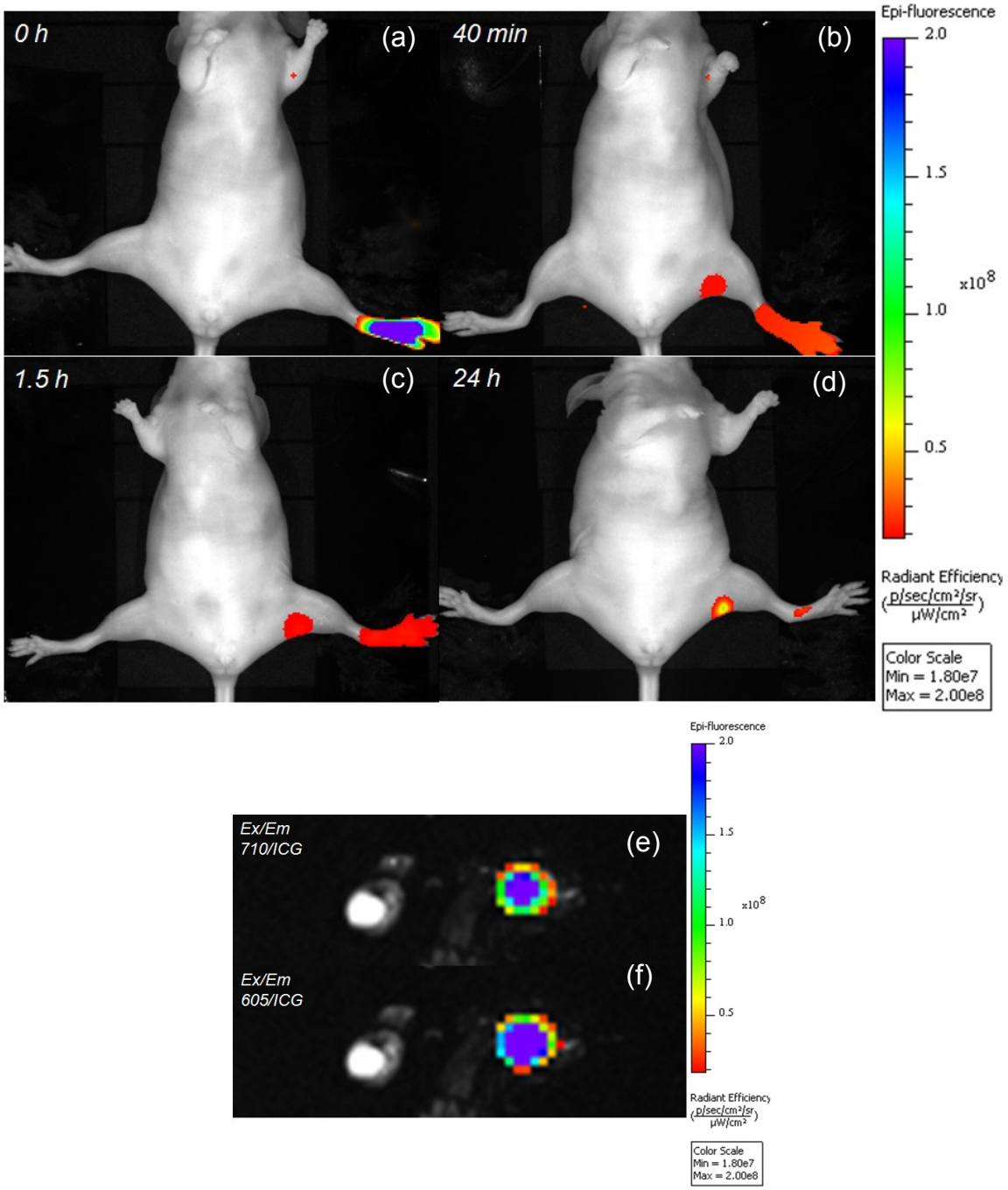

Figure 61. *In vivo* imaging of commercial QD800-NH_2 after footpad injection. The mice were anesthetized, injected with 20 μL of 0.16 μM of QDs and the fluorescence was measured with the IVIS Kinetic using filter sets 710/820 (Ex/Em). The fluorescence pattern was analyzed at different time interval post-injection, (a) 0 hr, (b) 40 min, (c) 90 min, (d) 24 h, (e) popiteal lymph nodes, (f) popiteal lymph nodes imaged with 605/ICG filters.

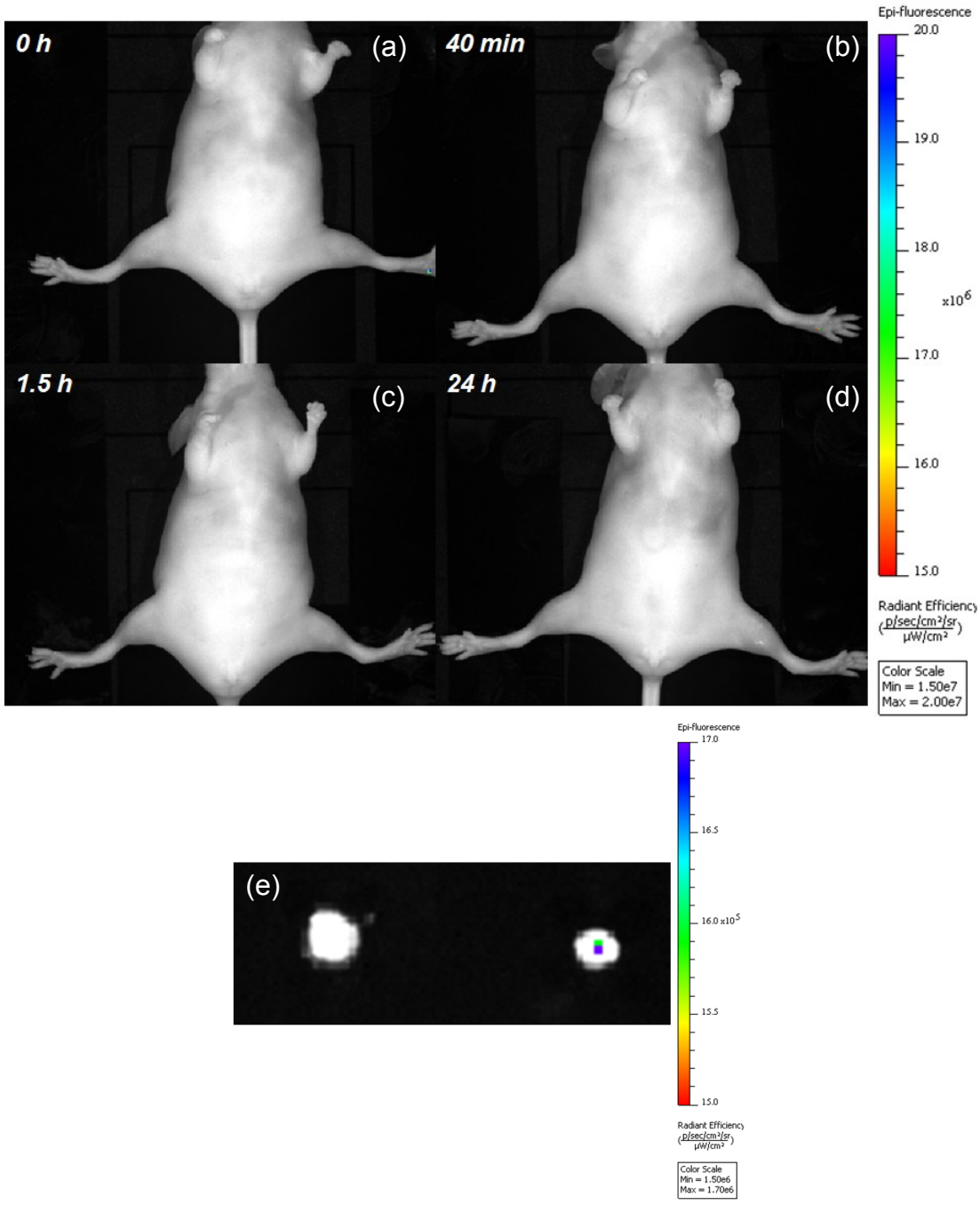

Figure 62. *In vivo* imaging of Au-MDS-TNF-C2-HepQD710 nanocomplexes after footpad injection. The mice were anesthetized, injected with 20 μL of nanocomplexes and the fluorescence was measured with the IVIS Kinetic using filter sets 710/820 (Ex/Em). The fluorescence pattern was analyzed at different time interval post-injection, (a) 0 hr, (b) 40 min, (c) 90 min, (d) 24 h, (e) popiteal lymph nodes.

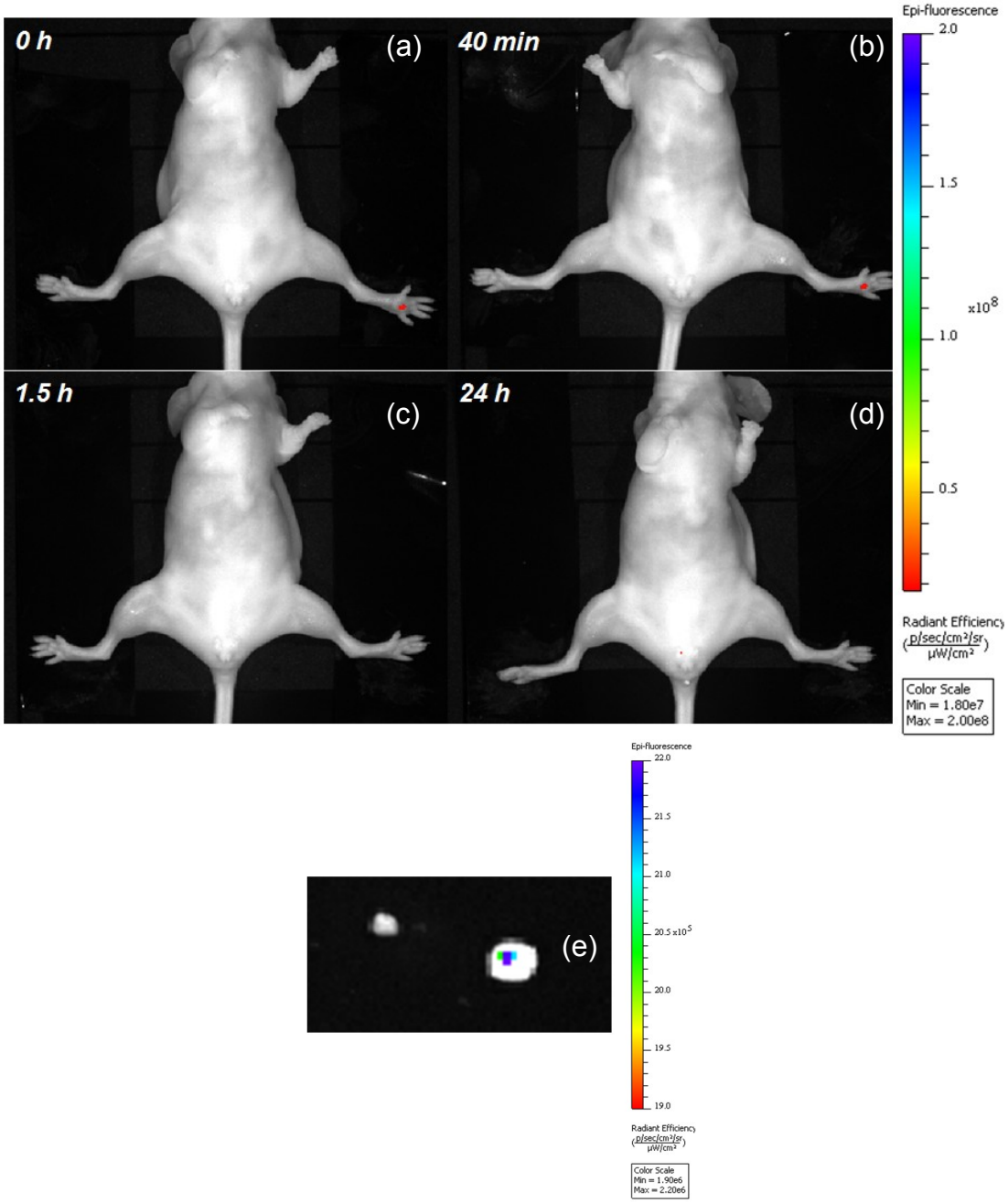

Figure 63. *In vivo* imaging of Au-MDS-TNF-C2-HepQD710-ChitAF790 nanocomplexes after footpad injection. The mice were anesthetized, injected with 20 μL of nanocomplexes and the fluorescence was measured with the IVIS Kinetic using filter sets 710/820 (Ex/Em). The fluorescence pattern was analyzed at different time interval post-injection, (a) 0 hr, (b) 90 min, (c) 24 h, (c) popiteal lymph nodes.

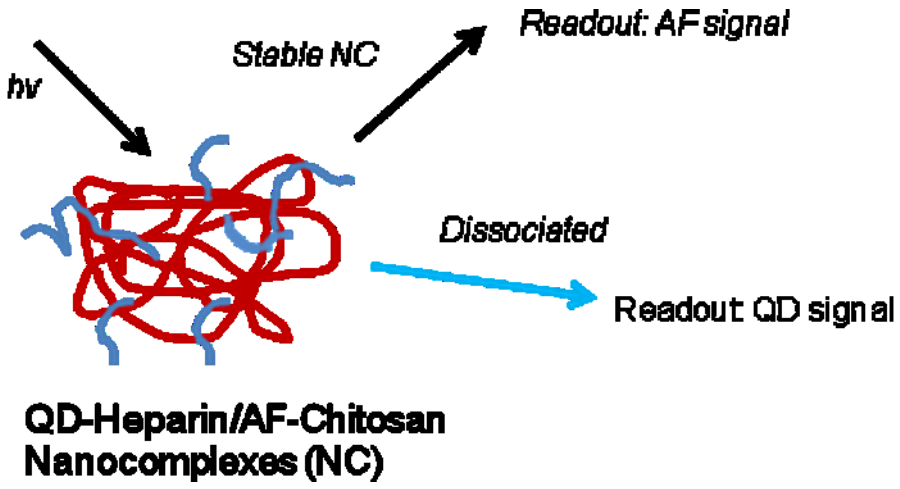

Figure 64. Schematic of QD-FRET analysis.

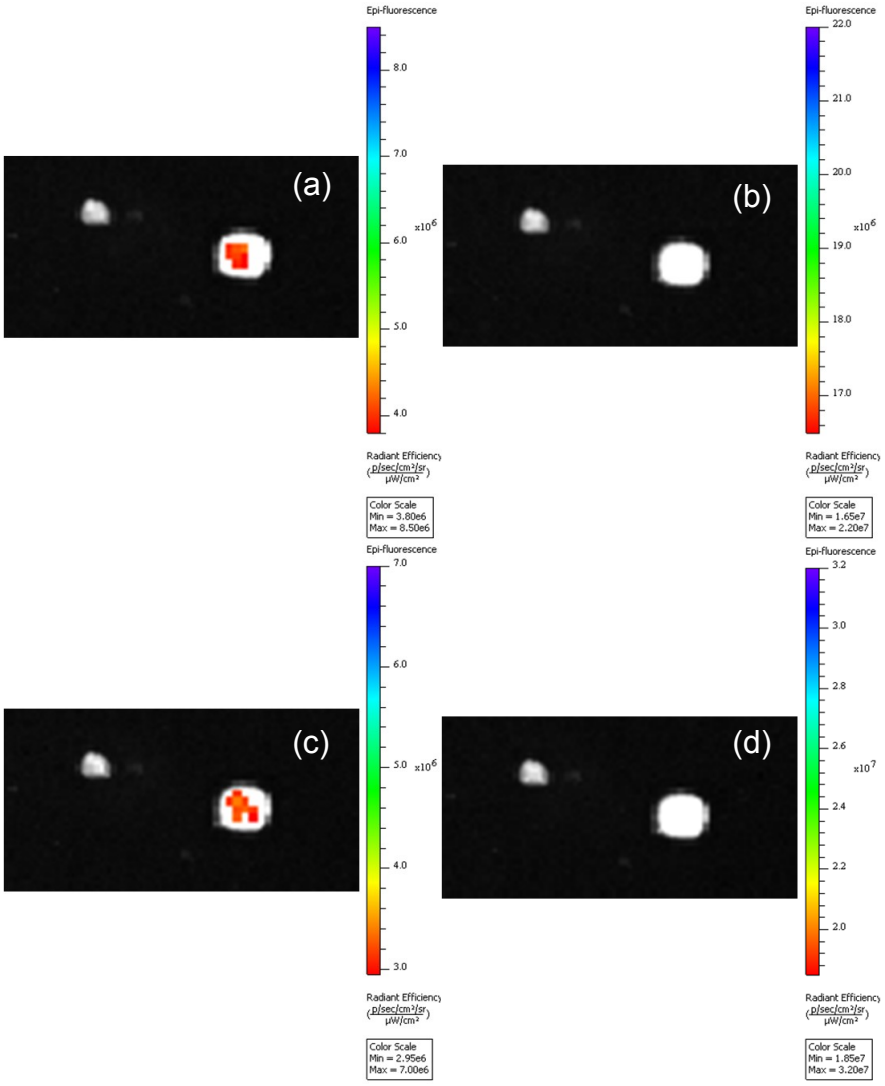

Figure 65. *Ex vivo* QD-FRET analysis of popiteal lymph nodes of mice injected with Au-MDS-TNF-C2-HepQD710-ChitAF790 nanocomplexes with different excitation/emission filter sets. (a) 605/ICG, (b) 605/Cy5.5, (c) 570/ICG, (d) 570/Cy5.5.

6.4 Conclusion

In summary, we have successfully conjugated QD710 to heparin, AlexaFluo 790 to chitosan and formulated nanocomplexes to encapsulate TNF-α for delivery to the lymph nodes. In the animal testing we could not detect strong QD-FRET signal 24 h post-injection possibly due to lack of T-cells in nude mice that affected the delivery mechanism, the nanocomplexes might have partially degraded along the delivery route, or the nanocomplexes might have traversed further to other lymph nodes such that the nanocomplexes were too dilute for detecting. Further experiments are needed for confirmation.

Chapter 7

Conclusion and Future Direction

Quantum dots (QDs) are attractive for several biological applications. However, the challenge comes from developing biocompatible and heavy-metal free QDs. The goal of this dissertation was to design novel water-soluble, near-infrared emitting quantum dots that have the feasibility for surface modification to append bioactive moieties. Specifically, a biocompatible stabilizing ligand, L-glutathione was used to serve this purpose. Effort was made to elucidate the *in vivo* biodistribution and the outcome was different from the results reported for conventional QDs. Our QDs interestingly are found to be sequestered in the stomach *in vivo*. The underlying mechanism of QDs accumulating in the stomach is still unknown and further studies are required to address this observation.

We also exploited the uniqueness of the stabilizer and appended targeting moiety to the QDs and performed cellular study to validate the utility of QDs for cell specificity applications. From the imaging results we concluded that the surface modification chemistry was successful and this would open up further exploration for various targeting applications. We further explore the feasibility of using our QDs as nanoprobe for delivery to the lymph node. However, the results we obtained were not as expected; only a small portion nanoprobe was delivered to the lymph node. More experiments would be needed to address the delivery mechanisms in order to optimize the design of the nanoprobe for lymph node delivery study.

Potential research directions that can be stem from this work include: (1) a detailed investigation of the mechanism of the unusual *in vivo* biodistribution; (2) incorporation of multifunctionalities onto the surface of QDs to produce nanoprobes that can achieve simultaneous treatment and diagnosis; (3) precise engineering of the QDs as nanoprobes for real time *in vivo* tracking of drug delivery mechanisms and efficacies that can possible lead to better drug carrier designs in the future.

Appendix A: Stablizer selection

Reaction scheme for preparation of ZnSe QDs in aqueous solution

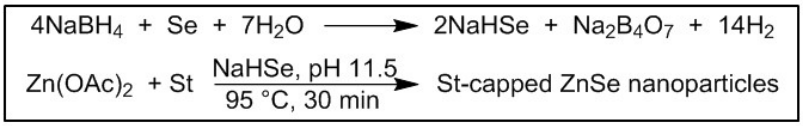

Stabilizer (St)

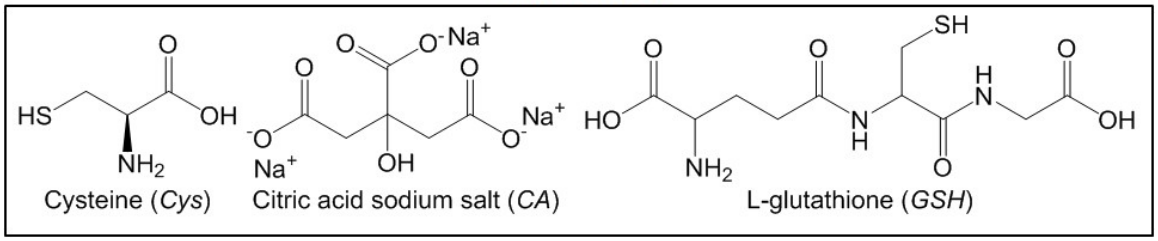

St	$Zn(OAc)_2$ (mmol)	NaHSe (mmol)	St (mmol)	E_{max} (nm)
Cys	0.5	0.2	0.6	QDs ppt
CA	0.5	0.2	0.6	No QDs formed
GSH	0.5	0.2	0.6	385

Appendix B: Dopant selection

Reaction scheme for preparation of ZnSeX QDs in aqueous solution

$NaBH_4$: sodium borohydride, Se: selenium, $Zn(OAc)_2$: zinc acetate, GSH: glutathione, X: dopant

Dopant	$Zn(OAc)_2$ (mmol)	Dopant (mmol)	NaHSe (mmol)	GSH (mmol)	Temp (°C)	E_{max} (nm)
$Cu(OAc)_2$	0.5	0.005	0.2	0.6	95	436
AgOAc	0.5	0.005	0.2	0.6	RT	648
$Au(OAc)_3$	0.5	0.005	0.2	0.6	RT/95	No QDs formed

Appendix C: Effect of pH on rate of reaction

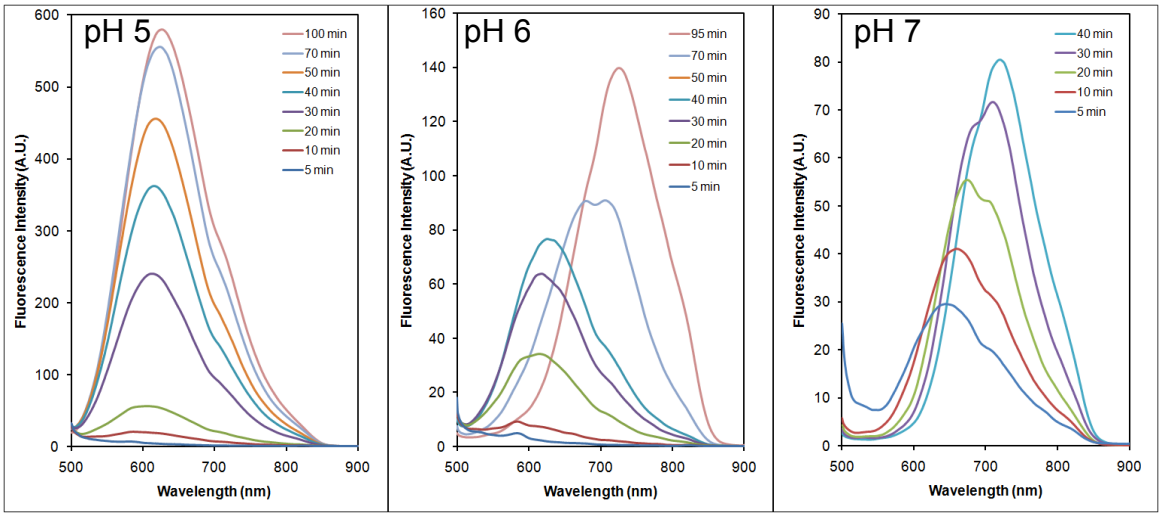

Appendix D: Effect of $Zn(OAc)_2$ on rate of reaction

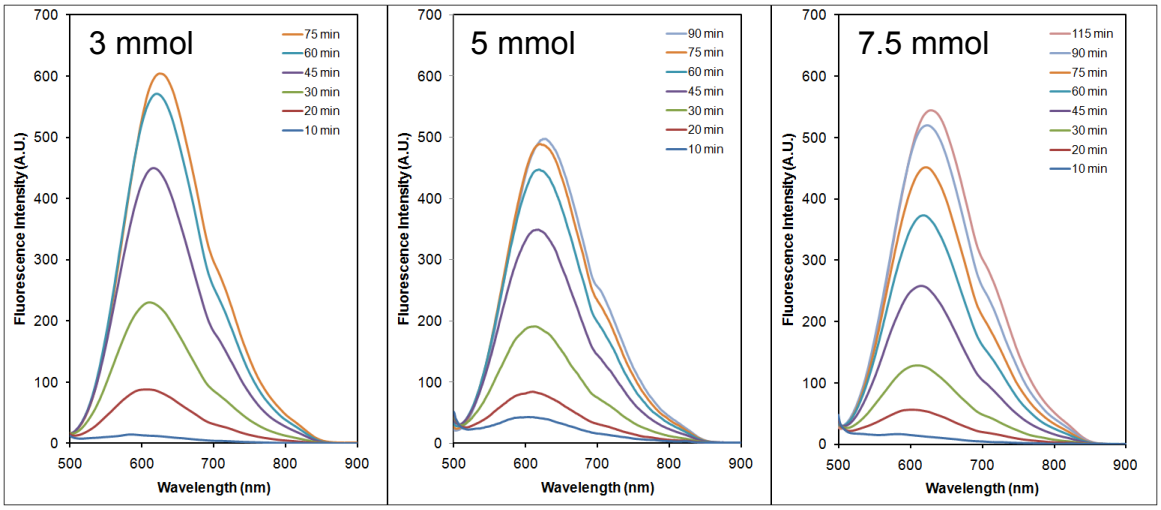

Appendix E: Effect of AgOAC on rate of reaction

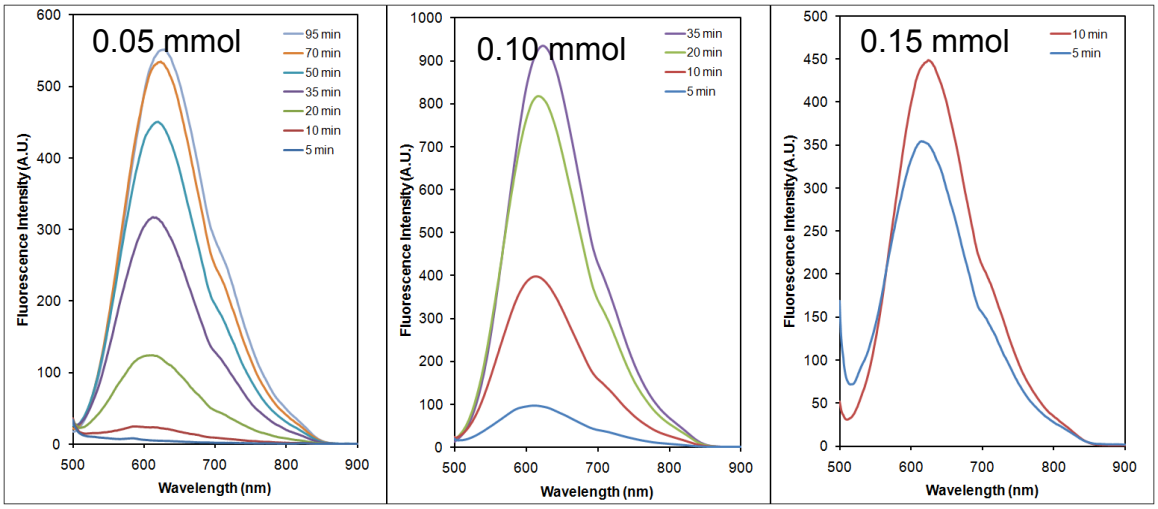

Appendix F: Effect of Se on rate of reaction

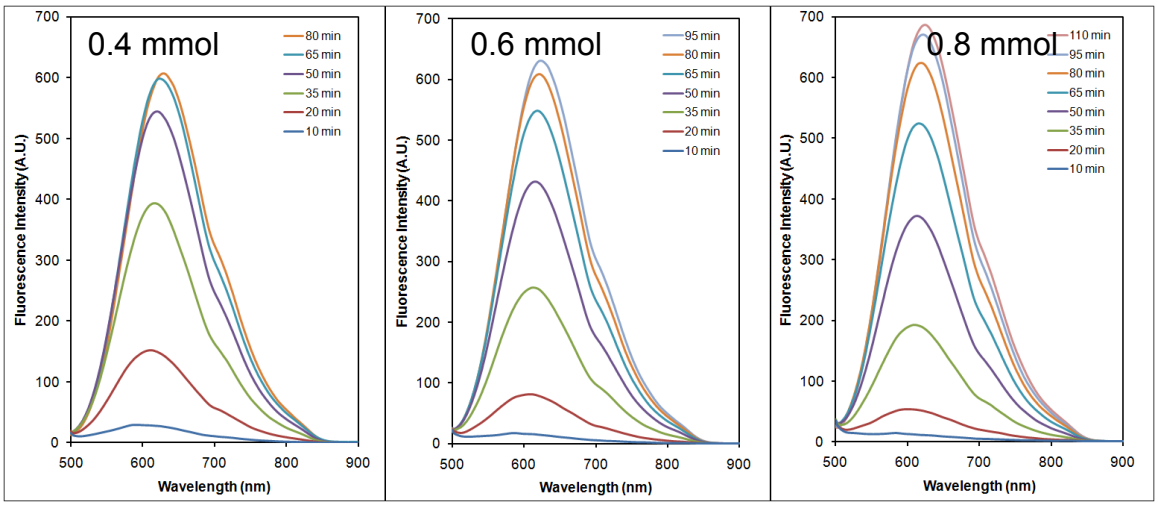

Appendix G: Effect of L-GSH at pH 5 on rate of reaction

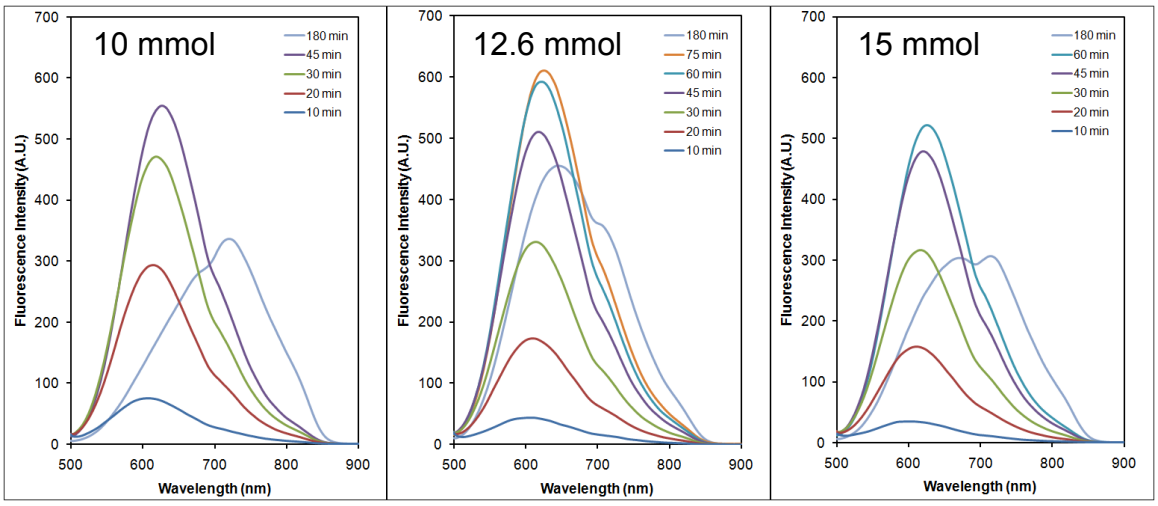

Appendix H: Effect of L-GSH at pH 7 on rate of reaction

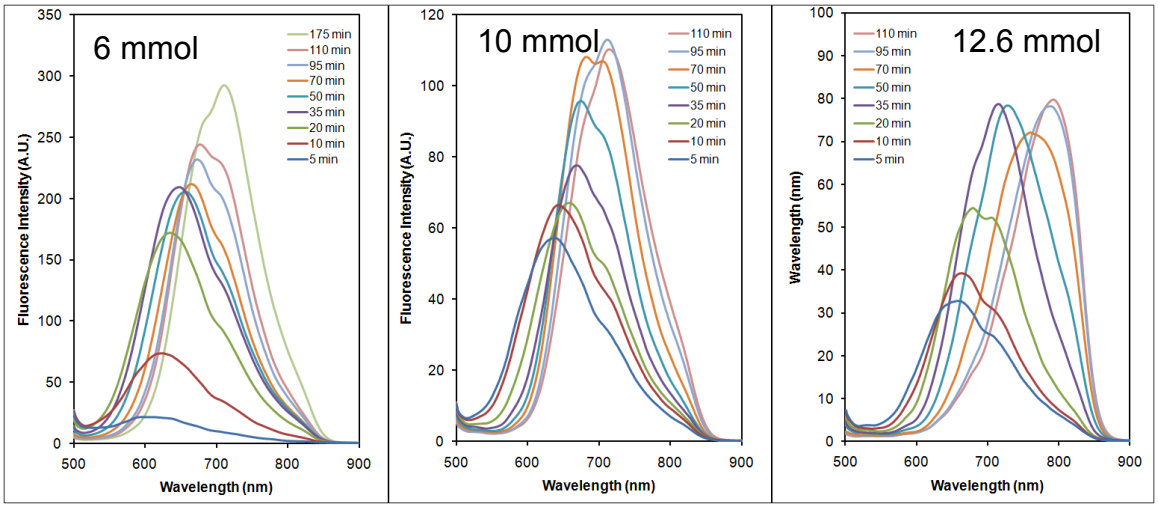

Appendix I: Cryo-section of stomach where QD710 was detected

(Slice 1)

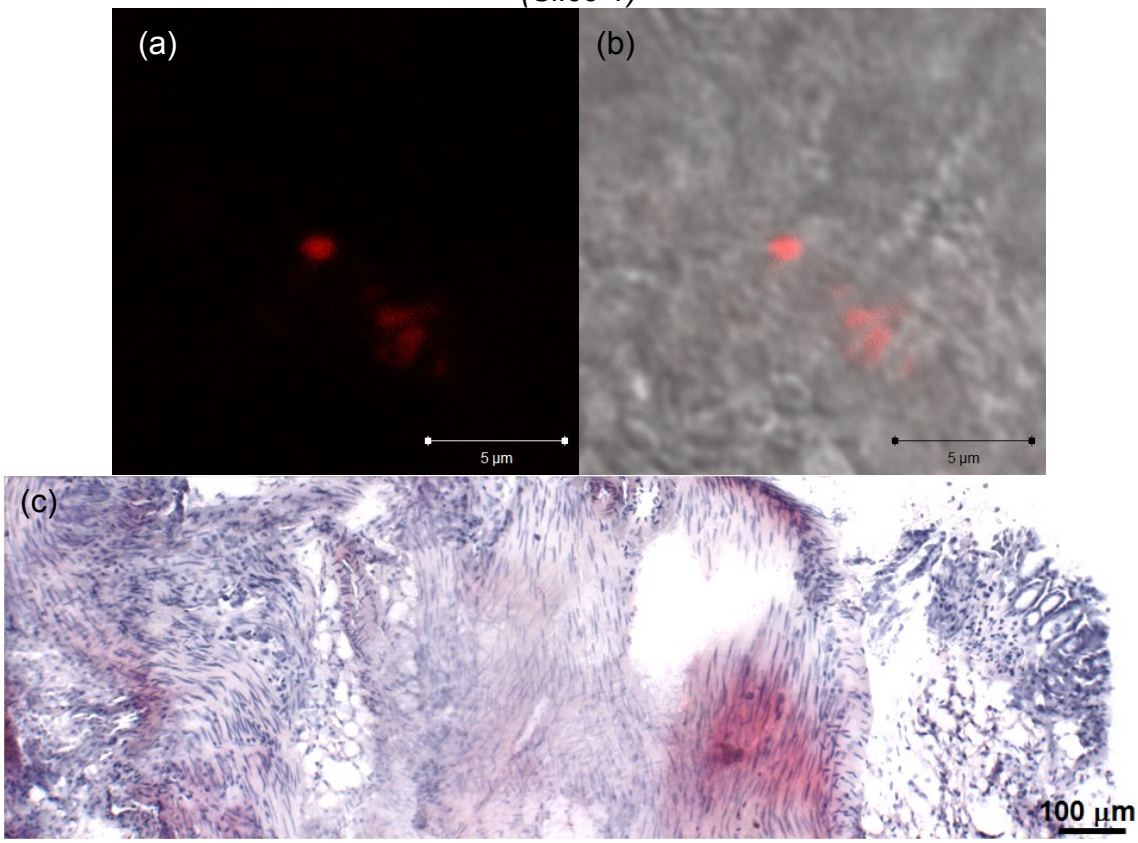

(a) Confocal image with 561 nm excitation source and observed with red filter. (b) Overlaps of brightfield and red filter.

(Slice 2)

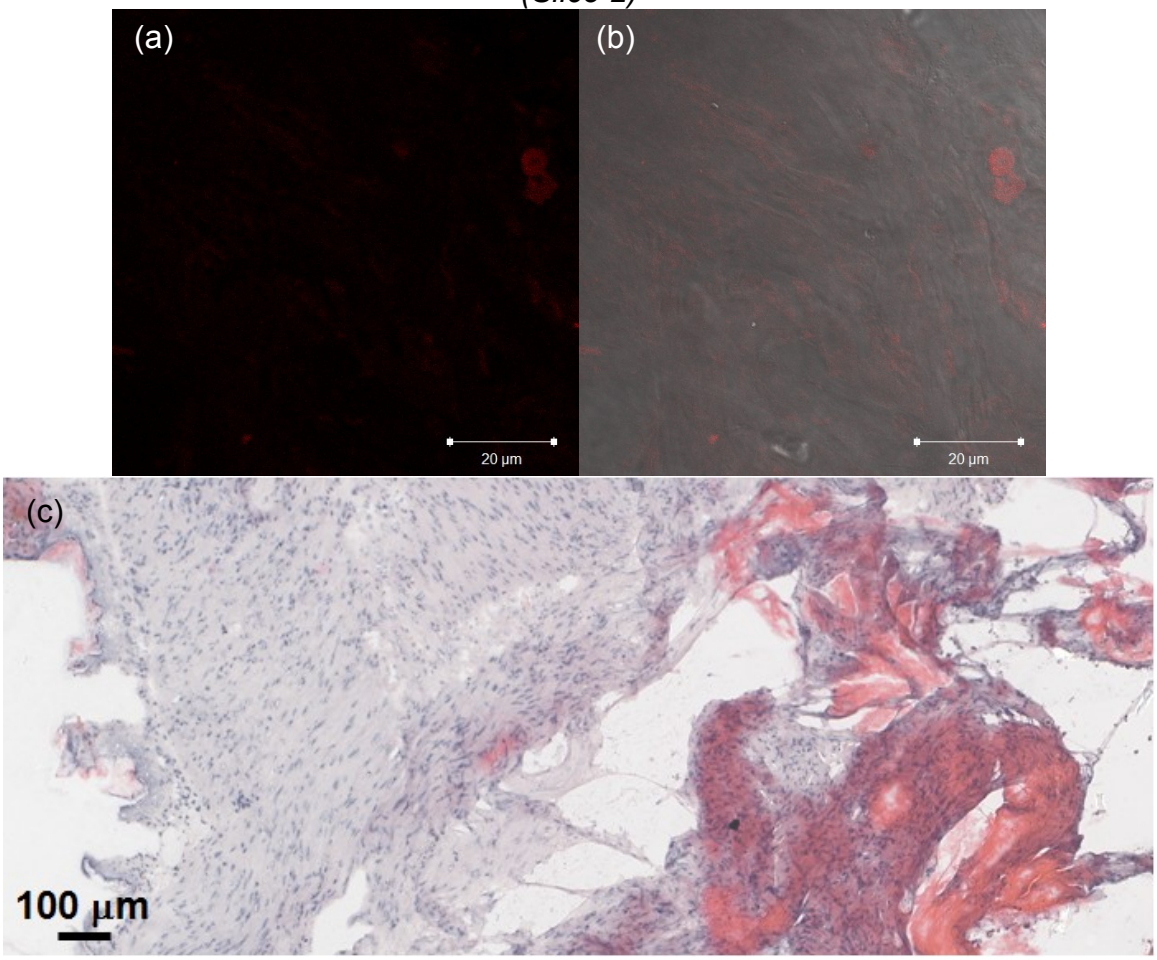

(a) Confocal image with 561 nm excitation source and observed with red filter. (b) Overlaps of brightfield and red filter.

(Slice 4)

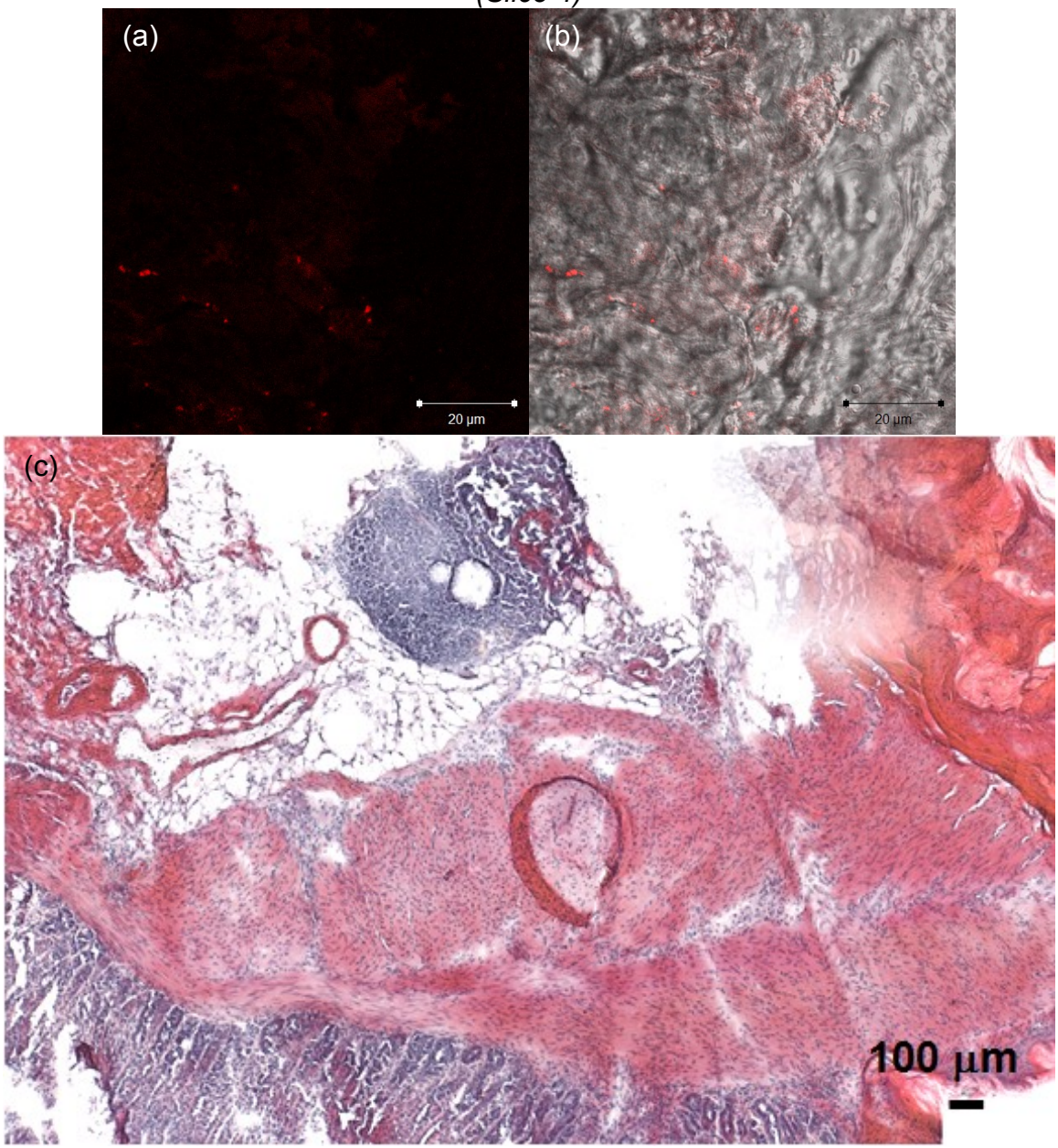

(a) Confocal image with 561 nm excitation source and observed with red filter. (b) Overlaps of brightfield and red filter.

(Slice 5)

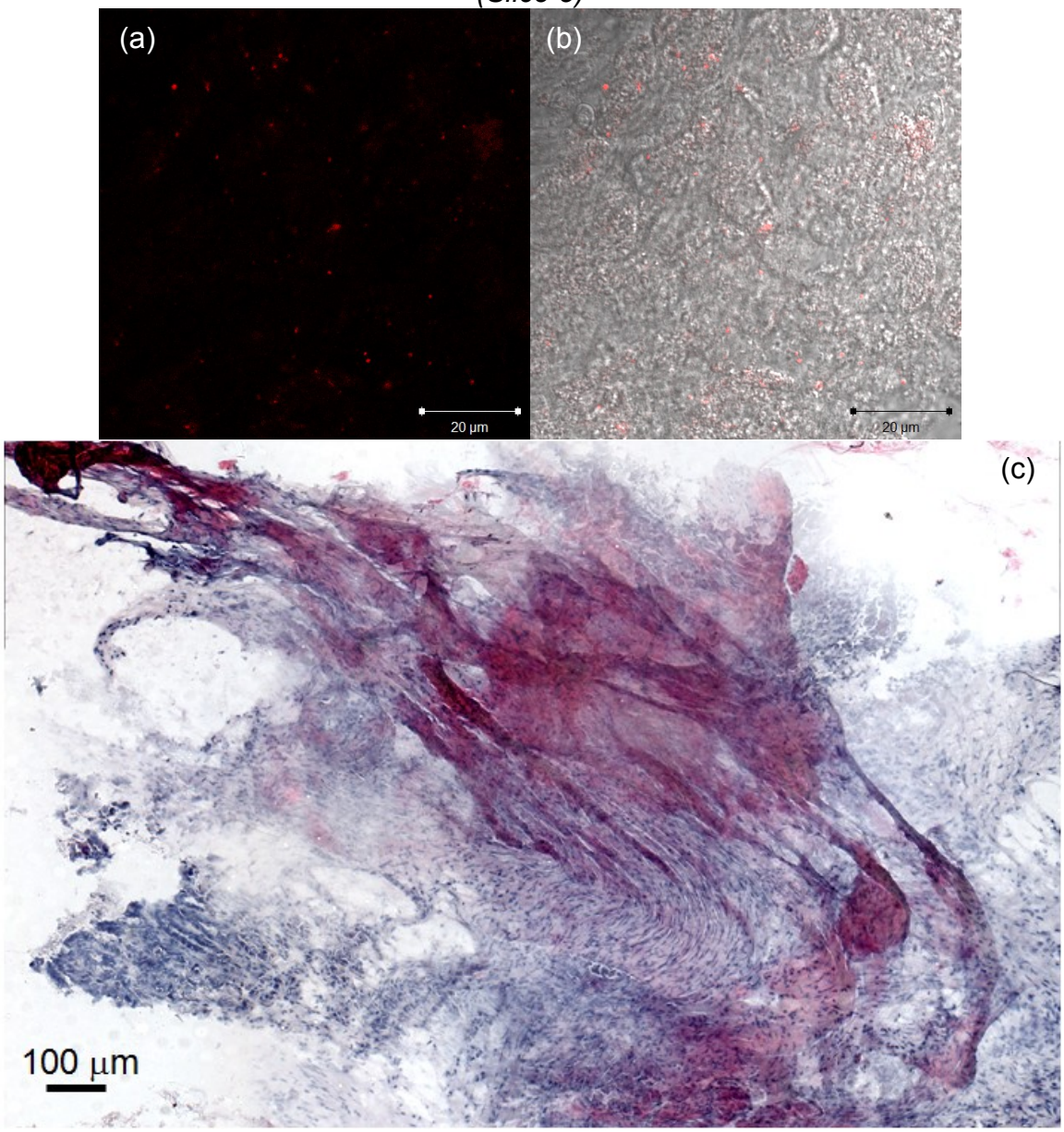

(a) Confocal image with 561 nm excitation source and observed with red filter. (b) Overlaps of brightfield and red filter.

(Slice 6)

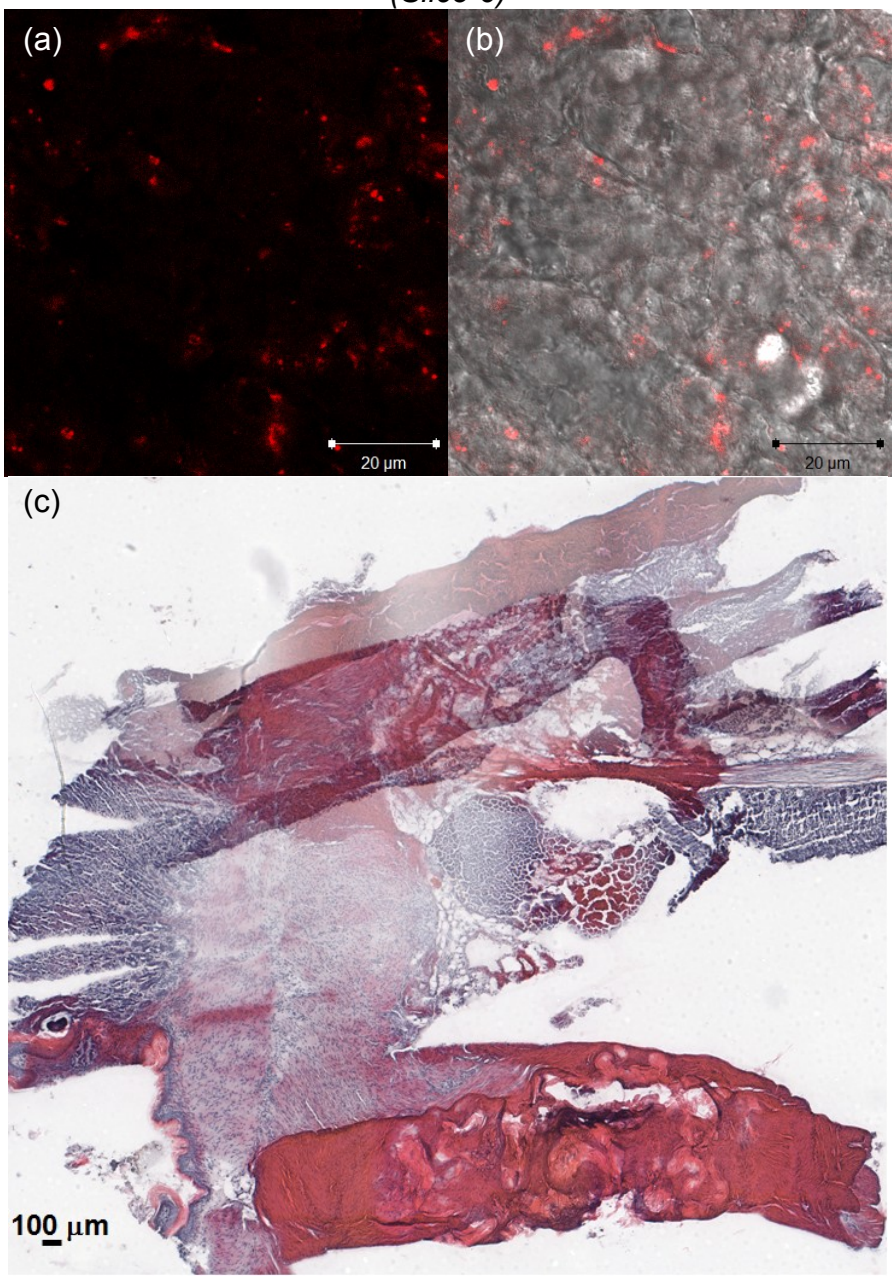

(a) Confocal image with 561 nm excitation source and observed with red filter. (b) Overlaps of brightfield and red filter.

(Slice 7)

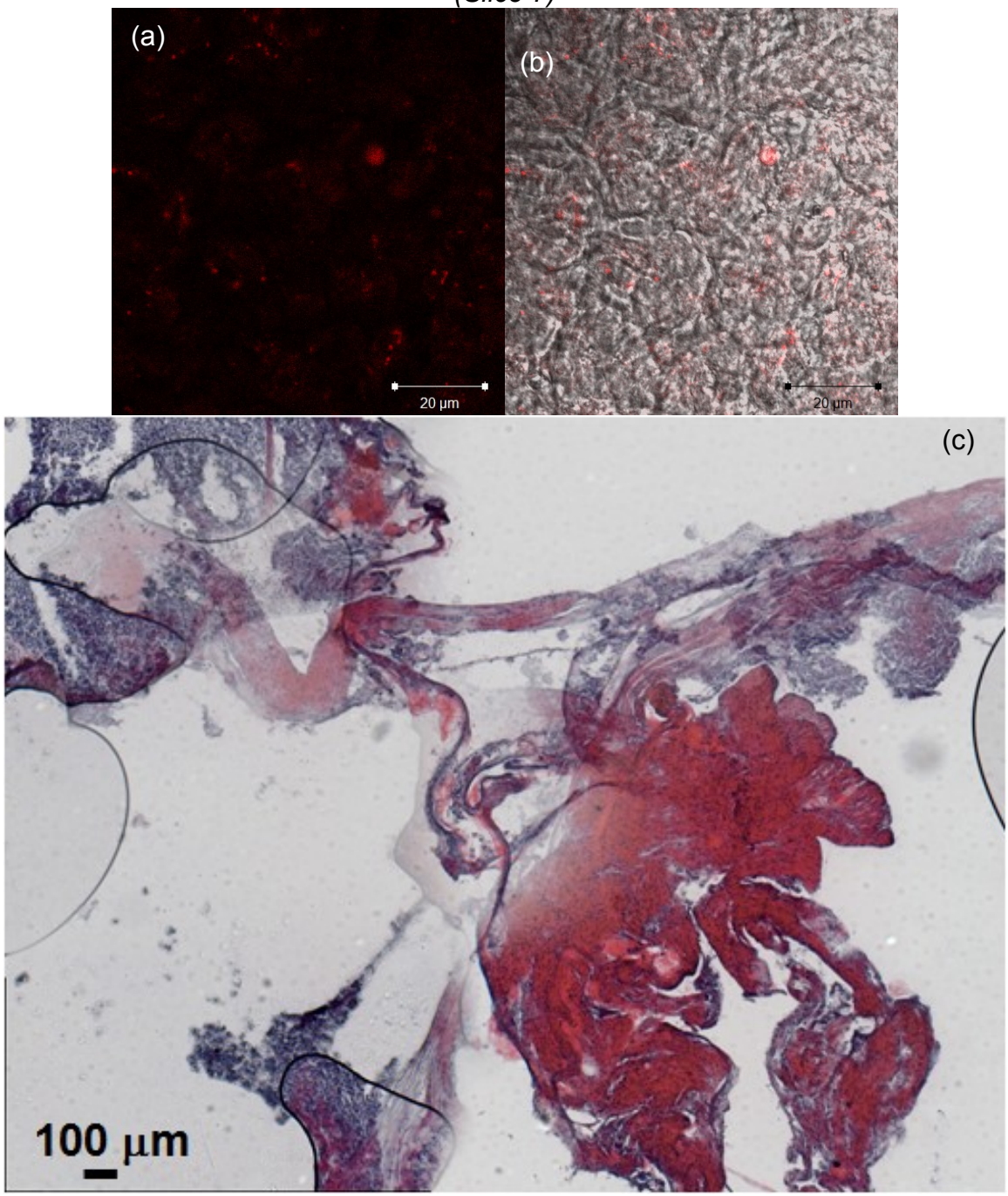

(a) Confocal image with 561 nm excitation source and observed with red filter. (b) Overlaps of brightfield and red filter.

(Slice 8)

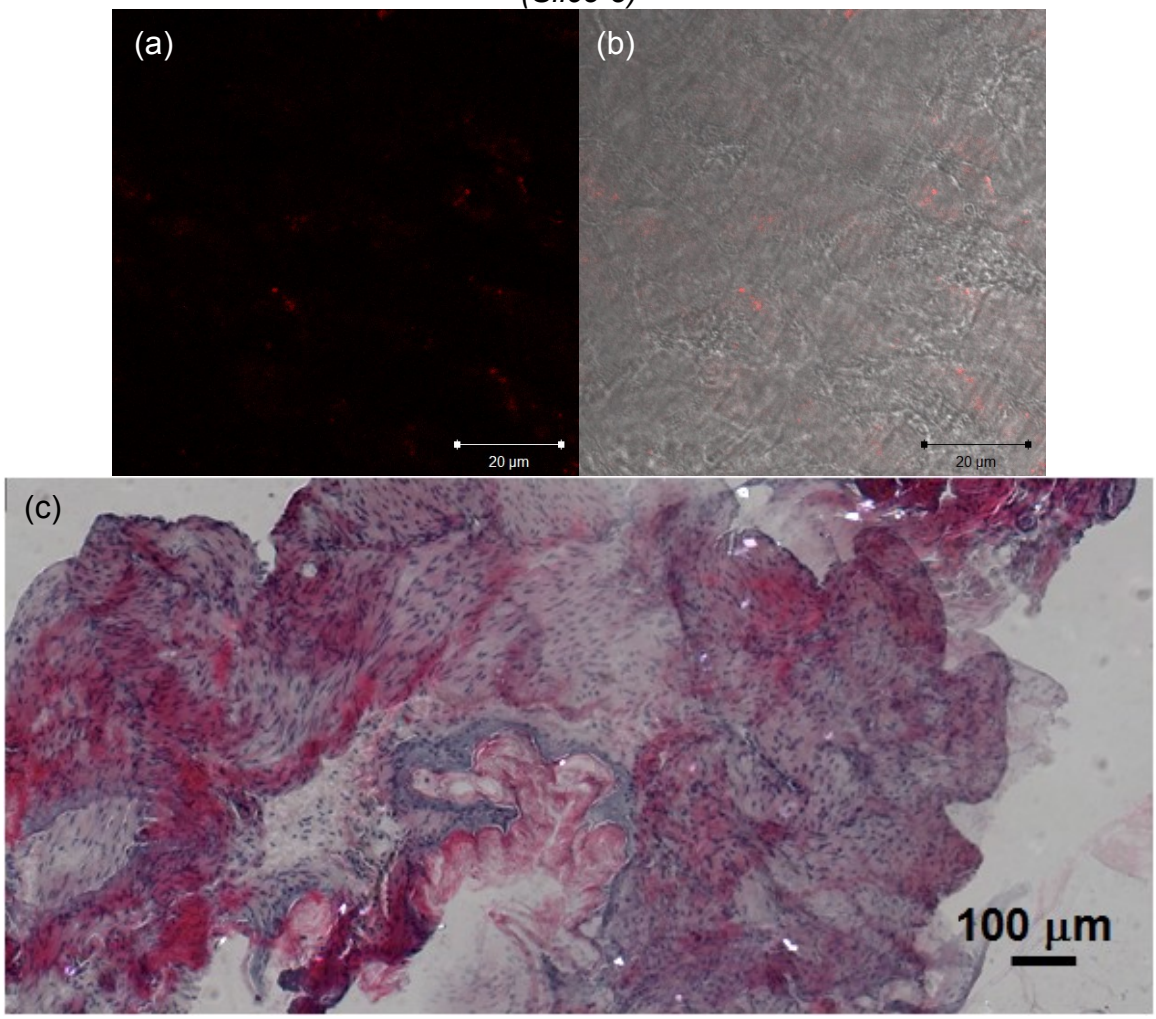

(a) Confocal image with 561 nm excitation source and observed with red filter. (b) Overlaps of brightfield and red filter.

(Slice 9)

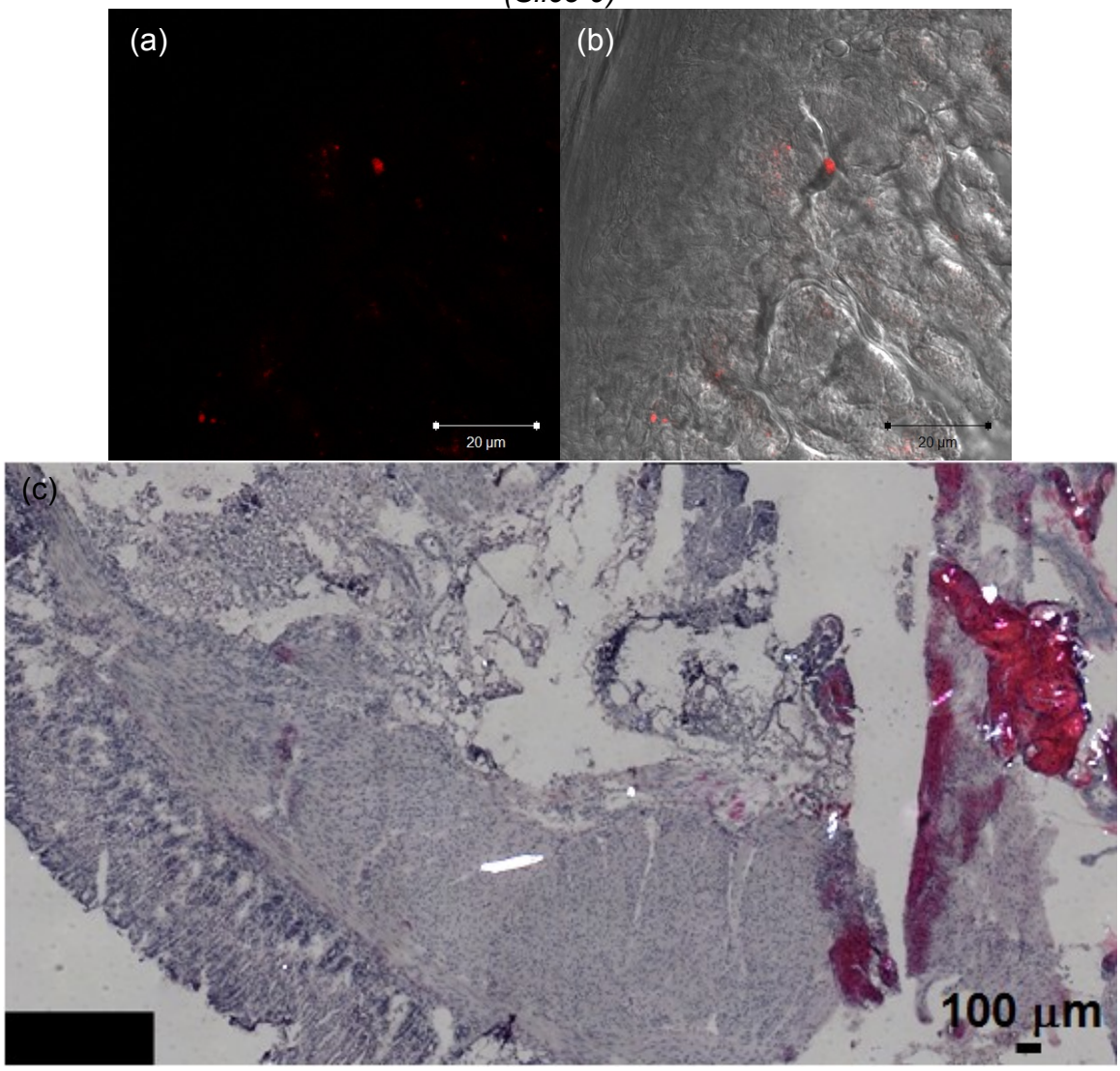

(a) Confocal image with 561 nm excitation source and observed with red filter. (b) Overlaps of brightfield and red filter.

(Slice 10)

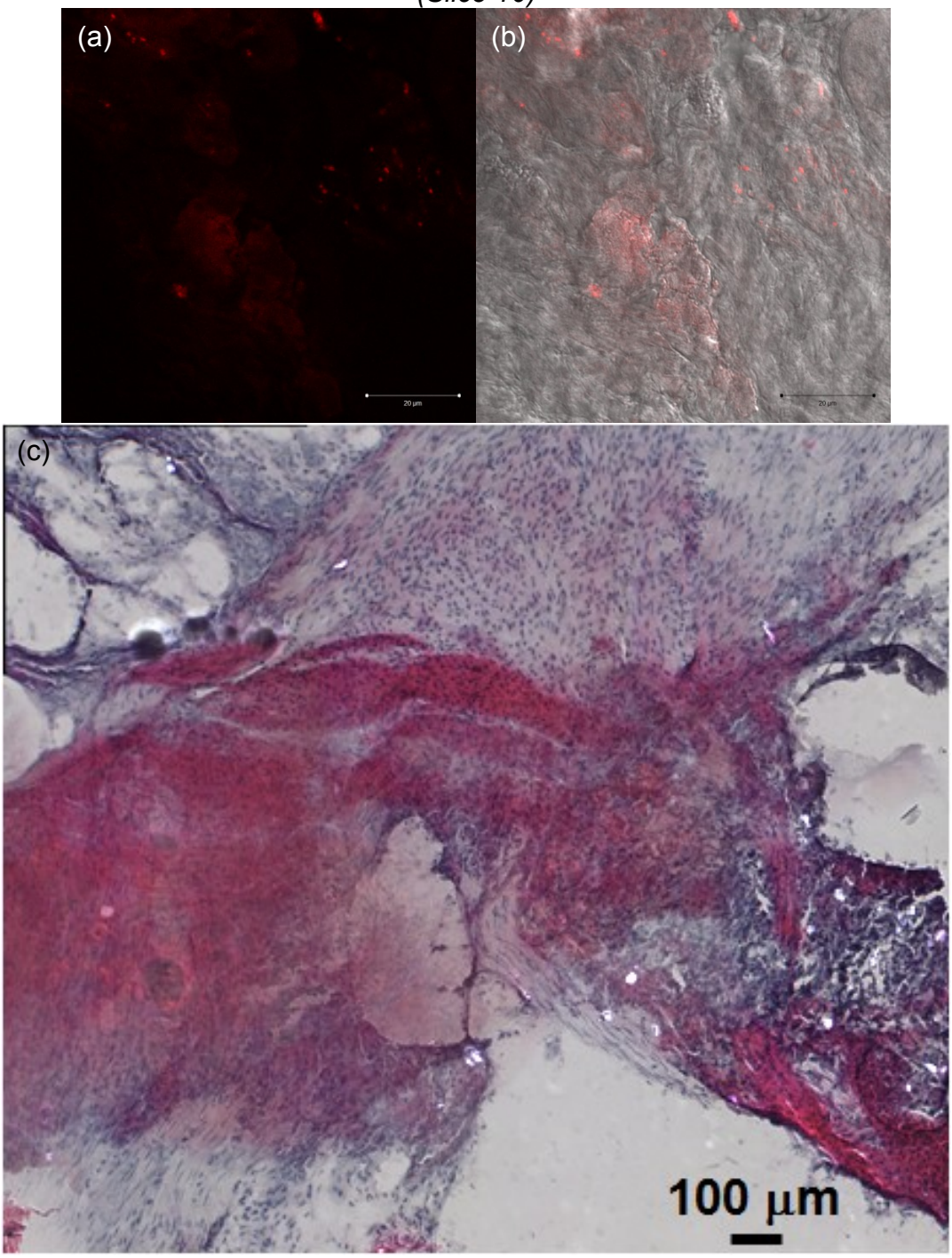

(a) Confocal image with 561 nm excitation source and observed with red filter. (b) Overlaps of brightfield and red filter.

(Slice 13)

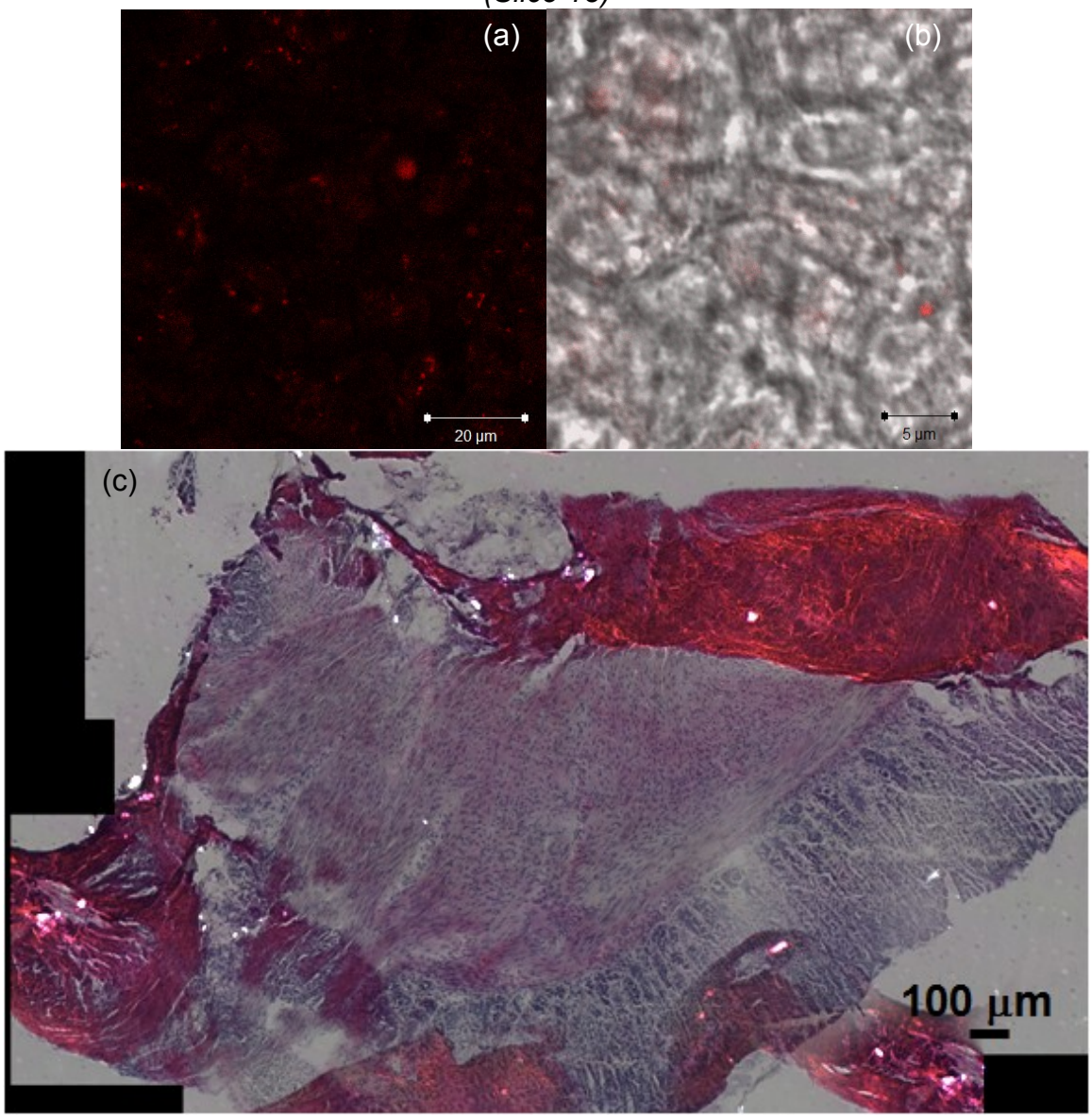

(a) Confocal image with 561 nm excitation source and observed with red filter. (b) Overlaps of brightfield and red filter.

(Slice 14)

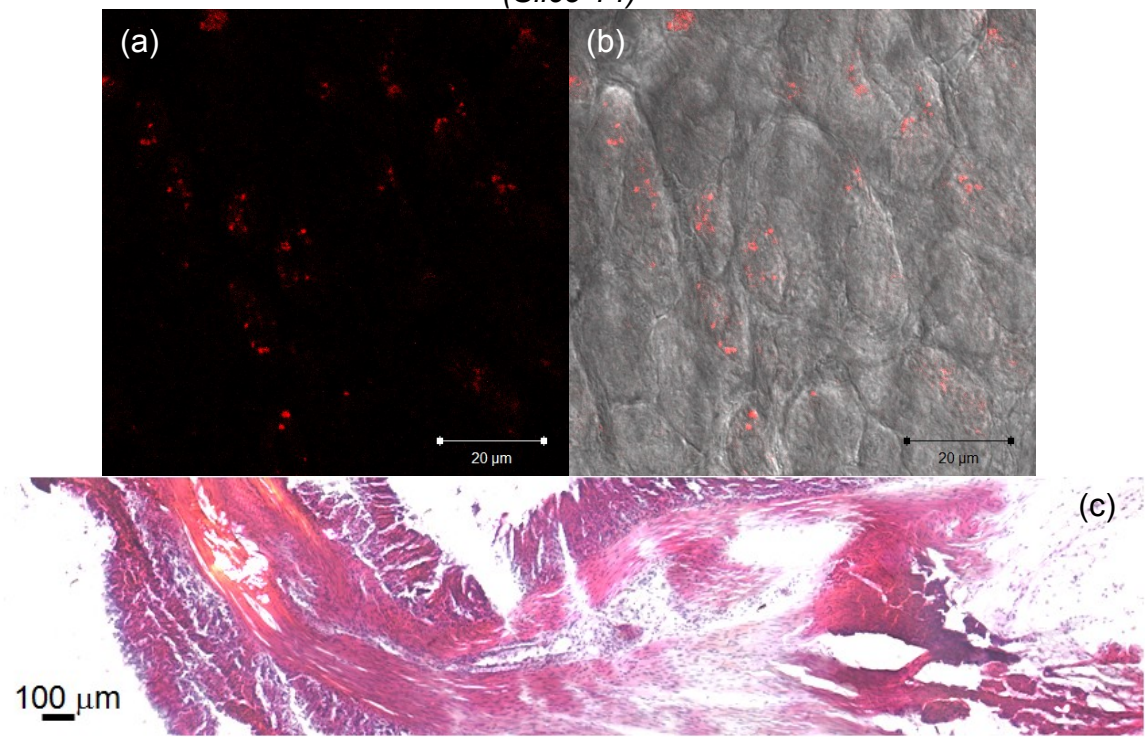

(a) Confocal image with 561 nm excitation source and observed with red filter. (b) Overlaps of brightfield and red filter.

Appendix J: Zeta potential distribution of LbL study

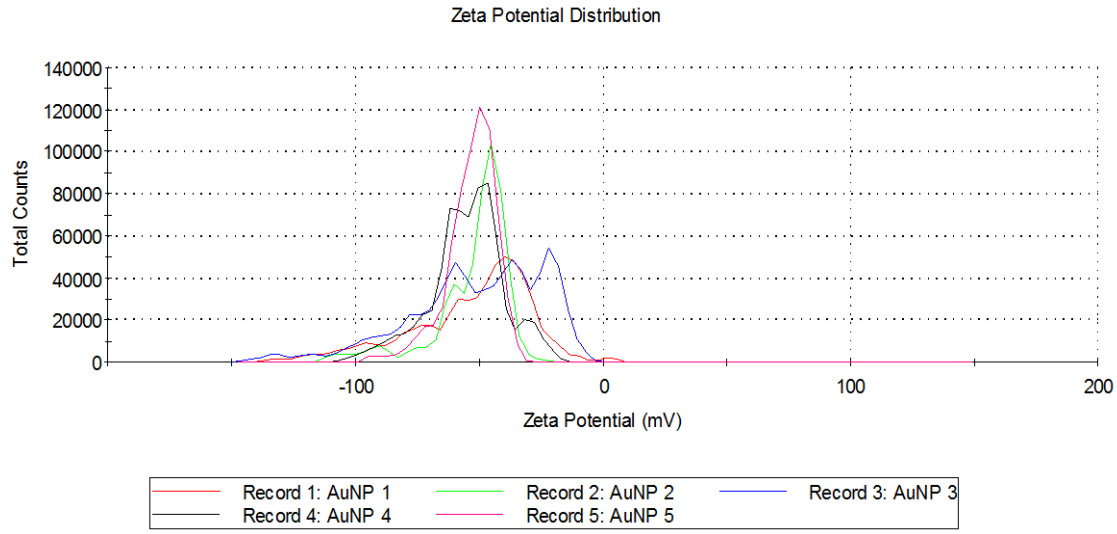

Zeta potential of Au-MDS

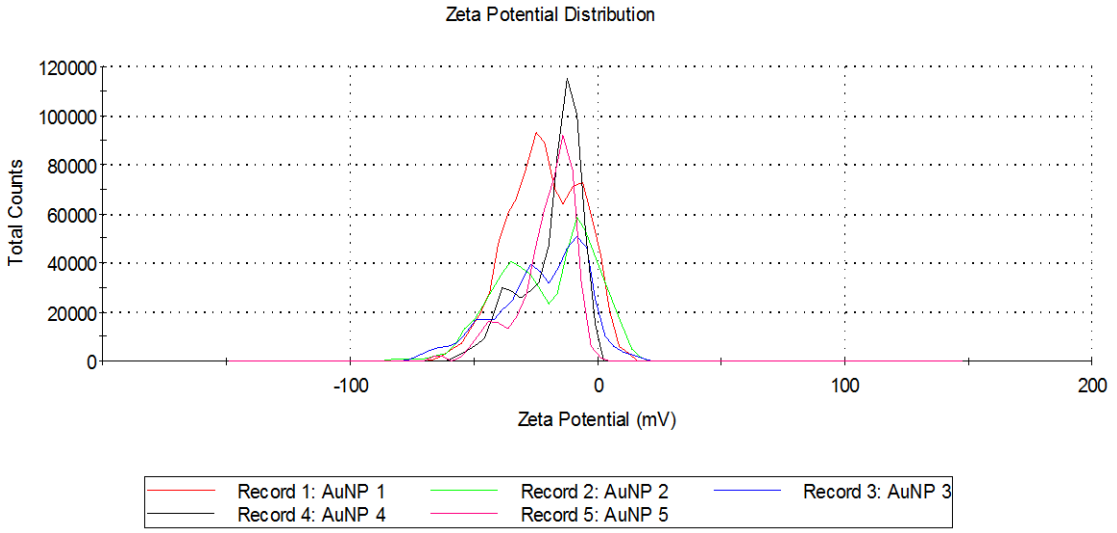

Zeta potential of Au-MDS-TNF

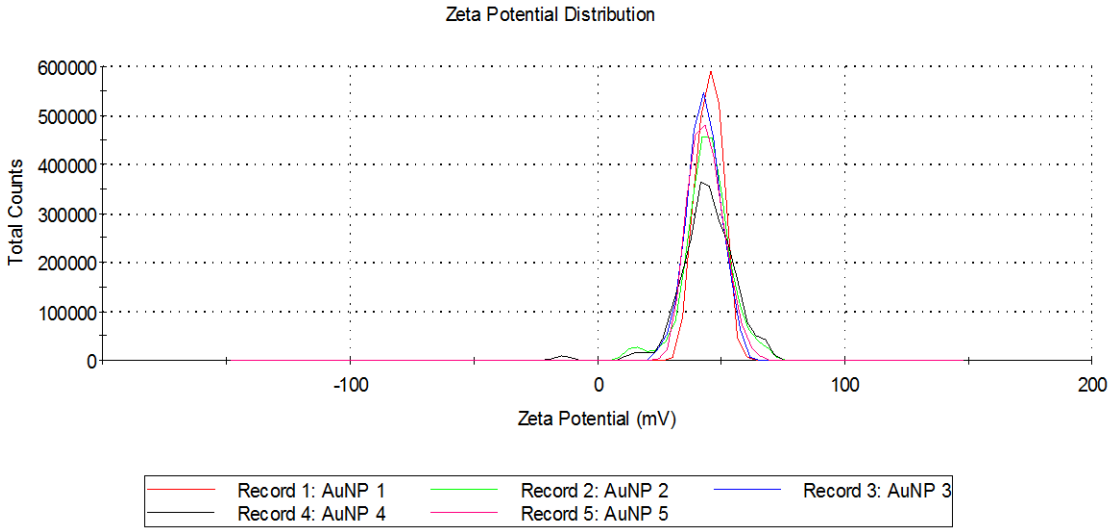

Zeta potential of Au-MDS-TNF-C1

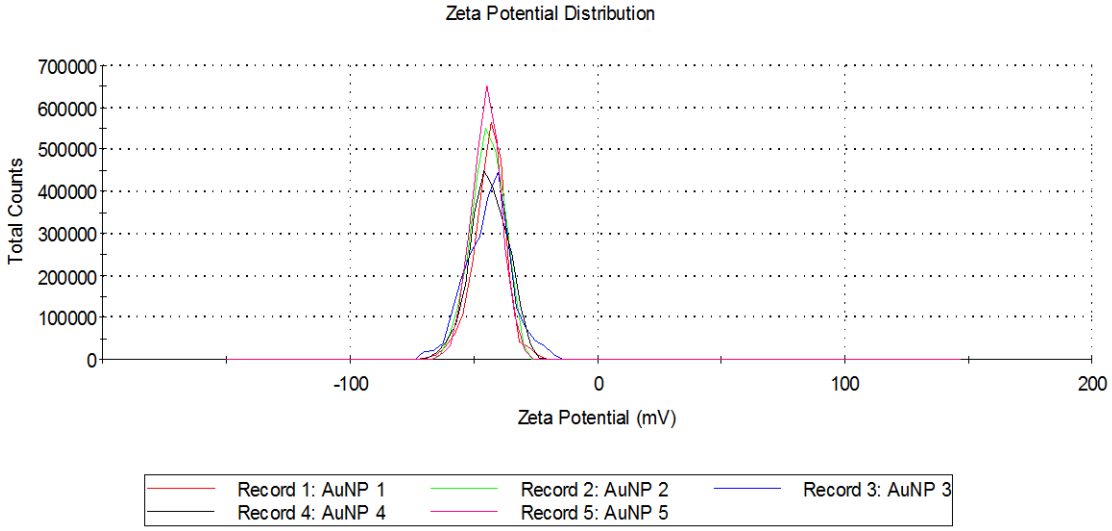

Zeta potential of Au-MDS-TNF-C1-H1

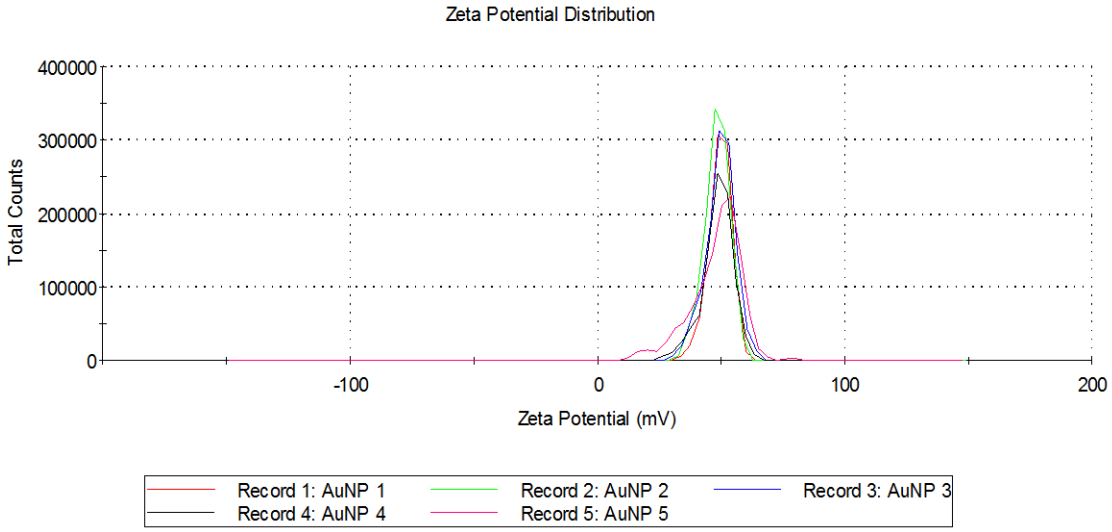

Zeta potential of Au-MDS-TNF-C2-H1

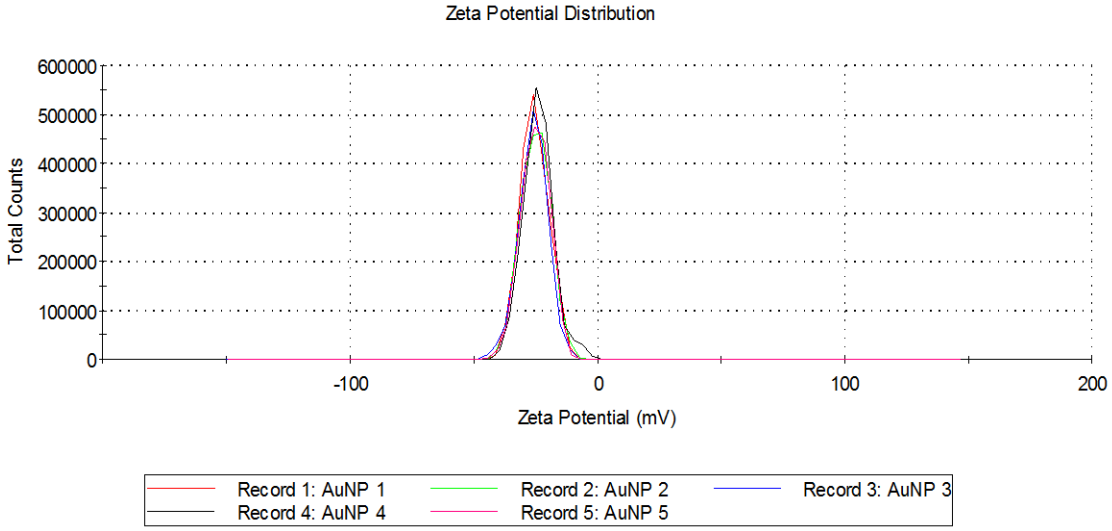

Zeta potential of Au-MDS-TNF-C1-Heparin-QD710

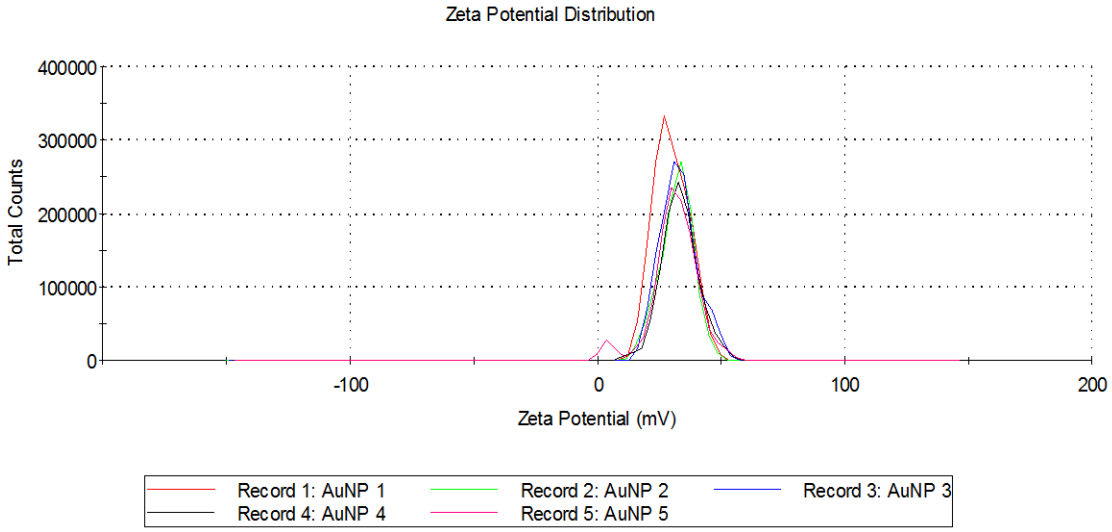

Zeta potential of Au-MDS-TNF-C2-Heparin-QD710

References

Abraham, S. N. and A. L. St John (2010). "Mast cell-orchestrated immunity to pathogens." Nature Reviews Immunology **10**(6): 440-452.

Achilefu, S. and R. B. Dorshow (2002). "Dynamic and continuous monitoring of renal and hepatic functions with exogenous markers." Contrast Agents Ii **222**: 31-72.

Achilefu, S., H. N. Jimenez, R. B. Dorshow, J. E. Bugaj, E. G. Webb, R. R. Wilhelm, R. Rajagopalan, J. Johler and J. L. Erion (2002). "Synthesis, in vitro receptor binding, and in vivo evaluation of fluorescein and carbocyanine peptide-based optical contrast agents." Journal of Medicinal Chemistry **45**(10): 2003-2015.

Alivisatos, A. P. (1996). "Semiconductor clusters, nanocrystals, and quantum dots." Science **271**(5251): 933-937.

Alivisatos, A. P., W. W. Gu and C. Larabell (2005). Quantum dots as cellular probes. Annual Review of Biomedical Engineering. Palo Alto, Annual Reviews. **7:** 55-76.

Alivisatos, P. (2004). "The use of nanocrystals in biological detection." Nature Biotechnology **22**(1): 47-52.

Allen, P. M. and M. G. Bawendi (2008). "Ternary I-III-VI quantum dots luminescent in the red to near-infrared." Journal of the American Chemical Society **130**(29): 9240-9241.

Ballou, B., G. W. Fisher, T. R. Hakala and D. L. Farkas (1997). "Tumor detection and visualization using cyanine fluorochrome-labeled antibodies." Biotechnology Progress **13**(5): 649-658.

Ballou, B., G. W. Fisher, A. S. Waggoner, D. L. Farkas, J. M. Reiland, R. Jaffe, R. B. Mujumdar, S. R. Mujumdar and T. R. Hakala (1995). "Tumor labeling in-vivo using cyanine-conjugated monoclonal-antibodies " Cancer Immunology Immunotherapy **41**(4): 257-263.

Bao, Y., H.-C. Yeh, C. Zhong, S. A. Ivanov, J. K. Sharma, M. L. Neidig, D. M. Vu, A. P. Shreve, R. B. Dyer, J. H. Werner and J. S. Martinez (2010). "Formation and stabilization of fluorescent gold nanoclusters using small molecules." Journal of Physical Chemistry C **114**(38): 15879-15882.

Barltrop, J. A., T. C. Owen, A. H. Cory and J. G. Cory (1991). "5-(3-Carboxymethoxyphenyl)-2-(4,5-dimethylthiazolyl)-3-(4-sulfophenyl)-tetrazolium, inner salt (MTS) and related analogs of 3-(4,5-dimethylthiazolyl)-2,5-diphenyltetrazolium bromide (MTT) reducing to purple water-soluble formazans as cell-viability indicators." Bioorganic & Medicinal Chemistry Letters **1**(11): 611-614.

Baughman, R. H., A. A. Zakhidov and W. A. de Heer (2002). "Carbon nanotubes - the route toward applications." Science **297**(5582): 787-792.

Becker, A., C. Hessenius, K. Licha, B. Ebert, U. Sukowski, W. Semmler, B. Wiedenmann and C. Grotzinger (2001). "Receptor-targeted optical imaging of tumors with near-infrared fluorescent ligands." Nature Biotechnology **19**(4): 327-331.

Birchler, M., G. Neri, L. Tarli, C. Halin, F. Viti and D. Neri (1999). "Infrared photodetection for the in vivo localisation of phage-derived antibodies directed against angiogenic markers." Journal of Immunological Methods **231**(1-2): 239-248.

Blum, G., G. von Degenfeld, M. J. Merchant, H. M. Blau and M. Bogyo (2007). "Noninvasive optical imaging of cysteine protease activity using fluorescently quenched activity-based probes." Nature Chemical Biology **3**(10): 668-677.

Bremer, C., V. Ntziachristos and R. Weissleder (2003). "Optical-based molecular imaging: contrast agents and potential medical applications." European Radiology **13**(2): 231-243.

Bruchez, M., M. Moronne, P. Gin, S. Weiss and A. P. Alivisatos (1998). "Semiconductor nanocrystals as fluorescent biological labels." Science **281**(5385): 2013-2016.

Bugaj, J. E., S. Achilefu, R. B. Dorshow and R. Rajagopalan (2001). "Novel fluorescent contrast agents for optical imaging of in vivo tumors based on a receptor-targeted dye-peptide conjugate platform." Journal of Biomedical Optics **6**(2): 122-133.

Buhro, W. E. and V. L. Colvin (2003). "Semiconductor nanocrystals - Shape matters." Nature Materials **2**(3): 138-139.

Bullok, K. E., D. Maxwell, A. H. Kesarwala, S. Gammon, J. L. Prior, M. Snow, S. Stanley and D. Piwnica-Worms (2007). "Biochemical and in vivo characterization of a small, membrane-permeant, caspase-activatable far-red fluorescent peptide for imaging apoptosis." Biochemistry **46**(13): 4055-4065.

Cao, Y. C. (2011). "Impurities enhance semiconductor nanocrystal performance." Science **332**(6025): 48-49.

Carion, O., B. Mahler, T. Pons and B. Dubertret (2007). "Synthesis, encapsulation, purification and coupling of single quantum dots in phospholipid micelles for their use in cellular and in vivo imaging." Nature Protocols **2**(10): 2383-2390.

Chan, W. C. W., D. J. Maxwell, X. H. Gao, R. E. Bailey, M. Y. Han and S. M. Nie (2002). "Luminescent quantum dots for multiplexed biological detection and imaging." Current Opinion in Biotechnology **13**(1): 40-46.

Chan, W. C. W. and S. M. Nie (1998). "Quantum dot bioconjugates for ultrasensitive nonisotopic detection." Science **281**(5385): 2016-2018.

Chen, D. A., R. Viswanatha, G. L. Ong, R. G. Xie, M. Balasubramaninan and X. G. Peng (2009). "Temperature dependence of "elementary processes" in doping semiconductor nanocrystals." Journal of the American Chemical Society **131**(26): 9333-9339.

Chen, H. H., Y.-P. Ho, X. Jiang, H.-Q. Mao, T.-H. Wang and K. W. Leong (2008). "Quantitative comparison of intracellular unpacking kinetics of polyplexes by a model constructed from quantum Dot-FRET." Molecular Therapy **16**(2): 324-332.

Chen, H. H. and K. W. Leong (2006). "Quantum-dots-FRET nanosensors for detecting unamplified nucleic acids by single molecule detection." Nanomedicine **1**(1): 119-122.

Cho, K. S., E. K. Lee, W. J. Joo, E. Jang, T. H. Kim, S. J. Lee, S. J. Kwon, J. Y. Han, B. K. Kim, B. L. Choi and J. M. Kim (2009). "High-performance crosslinked colloidal quantum-dot light-emitting diodes." Nature Photonics **3**(6): 341-345.

Cho, S. J., D. Maysinger, M. Jain, B. Roder, S. Hackbarth and F. M. Winnik (2007). "Long-term exposure to CdTe quantum dots causes functional impairments in live cells." Langmuir **23**(4): 1974-1980.

Clapp, A. R., E. R. Goldman and H. Mattoussi (2006). "Capping of CdSe-ZnS quantum dots with DHLA and subsequent conjugation with proteins." Nature Protocols **1**(3): 1258-1266.

Clapp, A. R., I. L. Medintz and H. Mattoussi (2006). "Forster resonance energy transfer investigations using quantum-dot fluorophores." Chemphyschem **7**(1): 47-57.

Clarke, S. J., C. A. Hollmann, Z. J. Zhang, D. Suffern, S. E. Bradforth, N. M. Dimitrijevic, W. G. Minarik and J. L. Nadeau (2006). "Photophysics of dopamine-modified quantumdots and effects on biological systems." Nature materials **5**(5): 409-417.

Coe, S., W. K. Woo, M. Bawendi and V. Bulovic (2002). "Electroluminescence from single monolayers of nanocrystals in molecular organic devices." Nature **420**(6917): 800-803.

Colvin, V. L. (2004). "The potential environmental impact of engineered nanomaterials (vol 21, pg 1166, 2003)." Nature Biotechnology **22**(6): 760-760.

Colvin, V. L., M. C. Schlamp and A. P. Alivisatos (1994). "Light-emitting diodes made from cadmium selenide nanocrystals and a semiconducting polymer. ." Nature **370**(6488): 354-357.

Contag, P. R. (2002). "Whole-animal cellular and molecular imaging to accelerate drug development." Drug Discovery Today **7**(10): 555-562.

Dai, H. J. (2002). "Carbon nanotubes: Synthesis, integration, and properties." Accounts of Chemical Research **35**(12): 1035-1044.

Dai, Q. Q., Y. N. Wang, X. B. Li, Y. Zhang, D. J. Pellegrino, M. X. Zhao, B. Zou, J. Seo, Y. D. Wang and W. W. Yu (2009). "Size-dependent composition and molar extinction coefficient of PbSe semiconductor nanocrystals." ACS Nano **3**(6): 1518-1524.

Dellian, M., F. Yuan, V. S. Trubetskoy, V. P. Torchilin and R. K. Jain (2000). "Vascular permeability in a human tumour xenograft: molecular charge dependence." British Journal of Cancer **82**(9): 1513-1518.

Derfus, A. M., W. C. W. Chan and S. N. Bhatia (2004). "Probing the cytotoxicity of semiconductor quantum dots." Nano Letters **4**(1): 11-18.

Derfus, A. M., A. A. Chen, D. H. Min, E. Ruoslahti and S. N. Bhatia (2007). "Targeted quantum dot conjugates for siRNA delivery." Bioconjugate Chemistry **18**(5): 1391-1396.

Devadas, M. S., J. Kim, E. Sinn, D. Lee, T. Goodson and G. Ramakrishna (2010). "Unique Ultrafast Visible Luminescence in Monolayer-Protected Au(25) Clusters." Journal of Physical Chemistry C **114**(51): 22417-22423.

Duan, H. W. and S. M. Nie (2007). "Etching colloidal gold nanocrystals with hyperbranched and multivalent polymers: A new route to fluorescent and water-soluble atomic clusters." Journal of the American Chemical Society **129**(9): 2412-2413.

Dubertret, B., P. Skourides, D. J. Norris, V. Noireaux, A. H. Brivanlou and A. Libchaber (2002). "In vivo imaging of quantum dots encapsulated in phospholipid micelles." Science **298**(5599): 1759-1762.

Dufort, S., L. Sancey, C. Wenk, V. Josserand and J. L. Coll (2010). "Optical small animal imaging in the drug discovery process." Biochimica Et Biophysica Acta-Biomembranes **1798**(12): 2266-2273.

Edgington, L. E., A. B. Berger, G. Blum, V. E. Albrow, M. G. Paulick, N. Lineberry and M. Bogyo (2009). "Noninvasive optical imaging of apoptosis by caspase-targeted activity-based probes." Nature Medicine **15**(8): 967-973.

Elbakry, A., A. Zaky, R. Liebkl, R. Rachel, A. Goepferich and M. Breunig (2009). "Layer-by-Layer Assembled Gold Nanoparticles for siRNA Delivery." Nano Letters **9**(5): 2059-2064.

Erogbogbo, F., K. T. Yong, R. Hu, W. C. Law, H. Ding, C. W. Chang, P. N. Prasad and M. T. Swihart (2010). "Biocompatible magnetofluorescent probes: Luminescent silicon quantum dots coupled with superparamagnetic iron(III) oxide." ACS Nano **4**(9): 5131-5138.

Erogbogbo, F., K. T. Yong, I. Roy, G. X. Xu, P. N. Prasad and M. T. Swihart (2008). "Biocompatible luminescent silicon quantum dots for imaging of cancer cells." ACS Nano **2**(5): 873-878.

Erwin, S. C., L. J. Zu, M. I. Haftel, A. L. Efros, T. A. Kennedy and D. J. Norris (2005). "Doping semiconductor nanocrystals." Nature **436**(7047): 91-94.

Escobedo, J. O., O. Rusin, S. Lim and R. M. Strongin (2010). "NIR dyes for bioimaging applications." Current Opinion in Chemical Biology **14**(1): 64-70.

Espevik, T. and J. Nissenmeyer (1986). "A highly sensitive cell-line, WEHI-164 clone 13, for measuring cytotoxic factor tumor-necrosis-factor from human-monocytes." Journal of Immunological Methods **95**(1): 99-105.

Feng, L. Z. and Z. A. Liu (2011). "Graphene in biomedicine: opportunities and challenges." Nanomedicine **6**(2): 317-324.

Figueiredo, J. L., H. Alencar, R. Weissleder and U. Mahmood (2006). "Near infrared thoracoscopy of tumoral protease activity for improved detection of peripheral lung cancer." International Journal of Cancer **118**(11): 2672-2677.

Fischer, J. E., H. Dai, A. Thess, R. Lee, N. M. Hanjani, D. L. Dehaas and R. E. Smalley (1997). "Metallic resistivity in crystalline ropes of single-wall carbon nanotubes." Physical Review B **55**(8): R4921-R4924.

Fiurasek, P. and L. Reven (2007). "Phosphonic and sulfonic acid-functionalized gold nanoparticles: A solid-state NMR study." Langmuir **23**(5): 2857-2866.

Folli, S., P. Westermann, D. Braichotte, A. Pelegrin, G. Wagnieres, H. Vandenbergh and J. P. Mach (1994). "Antibody-indocyanin conjugates for immunophotodetection of human squamous-cell carcinoma in nude-mice." Cancer Research **54**(10): 2643-2649.

Frangioni, J. V. (2003). "In vivo near-infrared fluorescence imaging." Current Opinion in Chemical Biology **7**(5): 626-634.

Fujioka, K., M. Hiruoka, K. Sato, N. Manabe, R. Miyasaka, S. Hanada, A. Hoshino, R. D. Tilley, Y. Manome, K. Hirakuri and K. Yamamoto (2008). "Luminescent passive-oxidized silicon quantum dots as biological staining labels and their cytotoxicity effects at high concentration." Nanotechnology **19**(41).

Gao, M. Y., S. Kirstein, H. Mohwald, A. L. Rogach, A. Kornowski, A. Eychmuller and H. Weller (1998). "Strongly photoluminescent CdTe nanocrystals by proper surface modification." Journal of Physical Chemistry B **102**(43): 8360-8363.

Gao, X. H., Y. Y. Cui, R. M. Levenson, L. W. K. Chung and S. M. Nie (2004). "In vivo cancer targeting and imaging with semiconductor quantum dots." Nature Biotechnology **22**(8): 969-976.

Gaponik, N. and A. L. Rogach (2010). "Thiol-capped CdTe nanocrystals: progress and perspectives of the related research fields." Physical Chemistry Chemical Physics **12**(31): 8685-8693.

Gartlon, J., A. Kinsner, A. Bal-Price, S. Coecke and R. H. Clothier (2006). "Evaluation of a proposed in vitro test strategy using neuronal and non-neuronal cell systems for detecting neurotoxicity." Toxicology in Vitro **20**(8): 1569-1581.

Gioux, S., H. S. Choi and J. V. Frangioni (2010). "Image-guided surgery using invisible near-infrared light: Fundamentals of clinical translation." Molecular Imaging **9**(5): 237-255.

Gittins, D. I. and F. Caruso (2001). "Tailoring the polyelectrolyte coating of metal nanoparticles." Journal of Physical Chemistry B **105**(29): 6846-6852.

Gross, S. and D. Piwnica-Worms (2006). "Molecular imaging strategies for drug discovery and development." Current Opinion in Chemical Biology **10**(4): 334-342.

Guo, G. N., W. Liu, J. G. Liang, Z. K. He, H. B. Xu and X. L. Yang (2007). "Probing the cytotoxicity of CdSe quantum dots with surface modification." Materials Letters **61**(8-9): 1641-1644.

Guo, S. J. and E. K. Wang (2011). "Noble metal nanomaterials: Controllable synthesis and application in fuel cells and analytical sensors." Nano Today **6**(3): 240-264.

Hardman, R. (2006). "A toxicologic review of quantum dots: Toxicity depends on physicochemical and environmental factors." Environmental Health Perspectives **114**(2): 165-172.

Hargreaves, R. J. (2008). "The role of molecular imaging in drug discovery and development." Clinical Pharmacology & Therapeutics **83**(2): 349-353.

Herbort, C. P., P. LeHoang and Y. Guex-Crosier (1998). "Schematic interpretation of indocyanine green angiography in posterior uveitis using a standard angiographic protocol." Ophthalmology **105**(3): 432-440.

Hickson, J. (2009). "In vivo optical imaging: Preclinical applications and considerations." Urologic Oncology-Seminars and Original Investigations **27**(3): 295-297.

Ho, Y.-P., H. H. Chen, K. W. Leong and T.-H. Wang (2006). "Evaluating the intracellular stability and unpacking of DNA nanocomplexes by quantum dots-FRET." Journal of Controlled Release **116**(1): 83-89.

Hong, H., Y. Zhang and W. B. Cai (2010). "In vivo imaging of RNA interference." Journal of Nuclear Medicine **51**(2): 169-172.

Hong, S. K., E. Kurtz, J. H. Chang, T. Hanada, M. Oku and T. Yao (2001). "Low stacking-fault density in ZnSe epilayers directly grown on epi-ready GaAs substrates without GaAs buffer layers." Applied Physics Letters **78**(2): 165-167.

Hua, F. J., F. Erogbogbo, M. T. Swihart and E. Ruckenstein (2006). "Organically capped silicon nanoparticles with blue photoluminescence prepared by hydrosilylation followed by oxidation." Langmuir **22**(9): 4363-4370.

Huang, C. C., C. T. Chen, Y. C. Shiang, Z. H. Lin and H. T. Chang (2009). "Synthesis of fluorescent carbohydrate-protected Au nanodots for detection of concanavalin A and escherichia coli." Analytical Chemistry **81**(3): 875-882.

Hunter, A. C. (2006). "Molecular hurdles in polyfectin design and mechanistic background to polycation induced cytotoxicity." Advanced Drug Delivery Reviews **58**(14): 1523-1531.

Huynh, W. U., J. J. Dittmer and A. P. Alivisatos (2002). "Hybrid nanorod-polymer solar cells." Science **295**(5564): 2425-2427.

Iijima, S. (1991). "Helical microtubules of graphitic carbon." Nature **354**(6348): 56-58.

Jana, N. R. and X. G. Peng (2003). "Single-phase and gram-scale routes toward nearly monodisperse Au and other noble metal nanocrystals." Journal of the American Chemical Society **125**(47): 14280-14281.

Jasieniak, J., M. Califano and S. E. Watkins (2011). "Size-dependent valence and conduction band-edge energies of semiconductor nanocrystals." ACS Nano **5**(7): 5888-5902.

Jeon, H., J. Ding, W. Patterson, A. V. Nurmikko, W. Xie, D. C. Grillo, M. Kobayashi and R. L. Gunshor (1991). "Blue-green injection-laser diodes in (Zn, Cd)Se/ZnSe quantum-wells." Applied Physics Letters **59**(27): 3619-3621.

Jokerst, J. V. and S. S. Gambhir (2011). "Molecular Imaging with Theranostic Nanoparticles." Accounts of Chemical Research **44**(10): 1050-1060.

Kevles, B. (1997). Naked to the bone : medical imaging in the twentieth century. New Brunswick, N.J., Rutgers University Press.

Kim, D. E., F. A. Jaffer, R. Weissleder, C. H. Tung and D. Schellingerhout (2005). "Near-infrared fluorescent imaging of cerebral thrombi and blood-brain barrier disruption in a mouse model of cerebral venous sinus thrombosis." Journal of Cerebral Blood Flow and Metabolism **25**(2): 226-233.

Kim, S., Y. T. Lim, E. G. Soltesz, A. M. De Grand, J. Lee, A. Nakayama, J. A. Parker, T. Mihaljevic, R. G. Laurence, D. M. Dor, L. H. Cohn, M. G. Bawendi and J. V. Frangioni (2004). "Near-infrared fluorescent type II quantum dots for sentinel lymph node mapping." Nature Biotechnology **22**(1): 93-97.

Kim, S. W., J. P. Zimmer, S. Ohnishi, J. B. Tracy, J. V. Frangioni and M. G. Bawendi (2005). "Engineering InAsxP1-x/InP/ZnSe III-V alloyed core/shell quantum dots for the near-infrared." Journal of the American Chemical Society **127**(30): 10526-10532.

Kirchner, C., T. Liedl, S. Kudera, T. Pellegrino, A. M. Javier, H. E. Gaub, S. Stolzle, N. Fertig and W. J. Parak (2005). "Cytotoxicity of colloidal CdSe and CdSe/ZnS nanoparticles." Nano Letters **5**(2): 331-338.

Klayman, D. L. and T. S. Griffin (1973). "Reaction of selenium with sodium-borohydride in protic solvents-Facile method for introduction of selenium into organic-molecules. ." Journal of the American Chemical Society **95**(1): 197-200.

Koba, W., K. Kim, M. L. Lipton, L. Jelicks, B. Das, L. Herbst and E. Fine (2011). "Imaging devices for use in small animals." Seminars in Nuclear Medicine **41**(3): 151-165.

Kunder, C. A., A. L. S. John, G. J. Li, K. W. Leong, B. Berwin, H. F. Staats and S. N. Abraham (2009). "Mast cell-derived particles deliver peripheral signals to remote lymph nodes." Journal of Experimental Medicine **206**(11): 2455-2467.

Lee, H., I. K. Kim and T. G. Park (2010). "Intracellular trafficking and unpacking of siRNA/quantum dot-PEI complexes modified with and without cell penetrating peptide: Confocal and flow cytometric FRET analysis." Bioconjugate Chemistry **21**(2): 289-295.

Li, J. B., D. D. Wu, Z. R. Miao and Y. Zhang (2010). "Preparation of quantum dot bioconjugates and their applications in bio-imaging." Current Pharmaceutical Biotechnology **11**(6): 662-671.

Li, L., H. F. Qian and J. C. Ren (2005). "Rapid synthesis of highly luminescent CdTe nanocrystals in the aqueous phase by microwave irradiation with controllable temperature." Chemical Communications(4): 528-530.

Li, X. G., Y. Q. He, S. S. Talukdar and M. T. Swihart (2003). "Process for preparing macroscopic quantities of brightly photoluminescent silicon nanoparticles with emission spanning the visible spectrum." Langmuir **19**(20): 8490-8496.

Li, Z. F. and E. Ruckenstein (2004). "Water-soluble poly(acrylic acid) grafted luminescent silicon nanoparticles and their use as fluorescent biological staining labels." Nano Letters **4**(8): 1463-1467.

Licha, K. (2002). Contrast agents for optical imaging. Contrast Agents Ii. W. Krause. Berlin, Springer-Verlag Berlin. **222:** 1-29.

Liebert, A., P. Sawosz, D. Milej, M. Kacprzak, W. Weigl, M. Botwicz, J. Maczewska, K. Fronczewska, E. Mayzner-Zawadzka, L. Krolicki and R. Maniewski (2011). "Assessment of inflow and washout of indocyanine green in the adult human brain by monitoring of diffuse reflectance at large source-detector separation." Journal of Biomedical Optics **16**(4).

Liebert, A., H. Wabnitz, H. Obrig, R. Erdmann, M. Moller, R. Macdonald, H. Rinneberg, A. Villringer and J. Steinbrink (2006). "Non-invasive detection of fluorescence from exogenous chromophores in the adult human brain." Neuroimage **31**(2): 600-608.

Lim, Y. T., S. Kim, A. Nakayama, N. E. Stott, M. G. Bawendi and J. V. Frangioni (2003). "Selection of quantum dot wavelengths for biomedical assays and imaging." Molecular imaging **2**(1): 50-64.

Lin, C. A. J., T. Y. Yang, C. H. Lee, S. H. Huang, R. A. Sperling, M. Zanella, J. K. Li, J. L. Shen, H. H. Wang, H. I. Yeh, W. J. Parak and W. H. Chang (2009). "Synthesis, characterization, and bioconjugation of fluorescent gold nanoclusters toward biological labeling applications." ACS Nano **3**(2): 395-401.

Liu, J. J., J. E. Kohler, A. L. Blass, J. A. Moncaster, A. Mocofanescu, M. A. Marcus, E. A. Blakely, K. A. Bjornstad, C. Amarasiriwardena, N. Casey, L. E. Goldstein and D. I. Soybel (2011). "Demand for Zn2+ in Acid-Secreting Gastric Mucosa and Its Requirement for Intracellular Ca2+." Plos One **6**(6).

Liu, X., X. L. Guo, F. Liu, Y. Zhang, H. Zhang, G. S. Hu and J. Bai (2011). "Imaging of indocyanine green perfusion in mouse liver with fluorescence diffuse optical tomography." IEEE Transactions on Biomedical Engineering **58**(8).

Liu, Z., J. T. Robinson, S. M. Tabakman, K. Yang and H. J. Dai (2011). "Carbon materials for drug delivery & cancer therapy." Materials Today **14**(7-8): 316-323.

Lordi, V., N. Yao and J. Wei (2001). "Method for supporting platinum on single-walled carbon nanotubes for a selective hydrogenation catalyst." Chemistry of Materials **13**(3): 733-737.

Lovric, J., H. S. Bazzi, Y. Cuie, G. R. A. Fortin, F. M. Winnik and D. Maysinger (2005). "Differences in subcellular distribution and toxicity of green and red emitting CdTe quantum dots." Journal of Molecular Medicine-Jmm **83**(5): 377-385.

Lovric, J., S. J. Cho, F. M. Winnik and D. Maysinger (2005). "Unmodified cadmium telluride quantum dots induce reactive oxygen species formation leading to multiple organelle damage and cell death." Chemistry & Biology **12**(11): 1227-1234.

Manna, S. K., S. Sarkar, J. Barr, K. Wise, E. V. Barrera, O. Jejelowo, A. C. Rice-Ficht and G. T. Ramesh (2005). "Single-walled carbon nanotube induces oxidative stress and activates nuclear transcription factor-kappa B in human keratinocytes." Nano Letters **5**(9): 1676-1684.

Marten, K., C. Bremer, K. Khazaie, M. Sameni, B. Sloane, C.-H. Tung and R. Weissleder (2002). "Detection of dysplastic intestinal adenomas using enzyme-sensing molecular beacons in mice." Gastroenterology **122**(2): 406-414.

Massoud, T. F. and S. S. Gambhir (2003). "Molecular imaging in living subjects: Seeing fundamental biological processes in a new light." Genes & Development **17**(5): 545-580.

Mayya, K. S., B. Schoeler and F. Caruso (2003). "Preparation and organization of nanoscale polyelectrolyte-coated gold nanoparticles." Advanced Functional Materials **13**(3): 183-188.

Medintz, I. L., H. T. Uyeda, E. R. Goldman and H. Mattoussi (2005). "Quantum dot bioconjugates for imaging, labelling and sensing." Nature Materials **4**(6): 435-446.

Mei, B. C., K. Susumu, I. L. Medintz and H. Mattoussi (2009). "Polyethylene glycol-based bidentate ligands to enhance quantum dot and gold nanoparticle stability in biological media." Nature Protocols **4**(3): 412-423.

Melinon, P., B. Masenelli, F. Tournus and A. Perez (2007). "Playing with carbon and silicon at the nanoscale." Nature Materials **6**(7): 479-490.

Michalet, X., F. F. Pinaud, L. A. Bentolila, J. M. Tsay, S. Doose, J. J. Li, G. Sundaresan, A. M. Wu, S. S. Gambhir and S. Weiss (2005). "Quantum dots for live cells, in vivo imaging, and diagnostics." Science **307**(5709): 538-544.

Mishra, A., R. K. Behera, P. K. Behera, B. K. Mishra and G. B. Behera (2000). "Cyanines during the 1990s: A review." Chemical Reviews **100**(6): 1973-2011.

Mocatta, D., G. Cohen, J. Schattner, O. Millo, E. Rabani and U. Banin (2011). "Heavily doped semiconductor nanocrystal quantum dots." Science **332**(6025): 77-81.

Murray, C. B., C. R. Kagan and M. G. Bawendi (2000). "Synthesis and characterization of monodisperse nanocrystals and close-packed nanocrystal assemblies." Annual Review of Materials Science **30**: 545-610.

Murugesan, S., J. Xie and R. J. Linhardt (2008). "Immobilization of heparin: Approaches and applications." Current Topics in Medicinal Chemistry **8**(2): 80-100.

Nabiev, I., S. Mitchell, A. Davies, Y. Williams, D. Kelleher, R. Moore, Y. K. Gun'ko, S. Byrne, Y. P. Rakovich, J. F. Donegan, A. Sukhanova, J. Conroy, D. Cottell, N. Gaponik, A. Rogach and Y. Volkov (2007). "Nonfunctionalized nanocrystals can exploit a cell's active transport machinery delivering them to specific nuclear and cytoplasmic compartments." Nano Letters **7**(11): 3452-3461.

Negishi, Y., N. K. Chaki, Y. Shichibu, R. L. Whetten and T. Tsukuda (2007). "Origin of magic stability of thiolated gold clusters: A case study on Au-25(SC6H13)(18)." Journal of the American Chemical Society **129**(37): 11322-11323.

Negishi, Y., K. Nobusada and T. Tsukuda (2005). "Glutathione-protected gold clusters revisited: Bridging the gap between gold(I)-thiolate complexes and thiolate-protected gold nanocrystals." Journal of the American Chemical Society **127**(14): 5261-5270.

Negishi, Y., Y. Takasugi, S. Sato, H. Yao, K. Kimura and T. Tsukuda (2004). "Magic-numbered Au-n clusters protected by glutathione monolayers (n=18, 21, 25, 28, 32, 39): Isolation and spectroscopic characterization." Journal of the American Chemical Society **126**(21): 6518-6519.

Neri, D., B. Carnemolla, A. Nissim, A. Leprini, G. Querze, E. Balza, A. Pini, L. Tarli, C. Halin, P. Neri, L. Zardi and G. Winter (1997). "Targeting by affinity-matured recombinant antibody fragments of an angiogenesis associated fibronectin isoform." Nature Biotechnology **15**(12): 1271-1275.

Neu, M., D. Fischer and T. Kissel (2005). "Recent advances in rational gene transfer vector design based on poly(ethylene imine) and its derivatives." Journal of Gene Medicine **7**(8): 992-1009.

Norris, D. J., A. L. Efros and S. C. Erwin (2008). "Doped nanocrystals." Science **319**(5871): 1776-1779.

Nune, S. K., P. Gunda, B. K. Majeti, P. K. Thallapally and M. L. Forrest (2011). "Advances in lymphatic imaging and drug delivery." Advanced Drug Delivery Reviews **63**(10-11): 876-885.

Park, J., C. Dvoracek, K. H. Lee, J. F. Galloway, H. E. C. Bhang, M. G. Pomper and P. C. Searson (2011). "CuInSe/ZnS core/shell NIR quantum dots for biomedical imaging." Small **7**(22): 3148-3152.

Park, J. H., L. Gu, G. von Maltzahn, E. Ruoslahti, S. N. Bhatia and M. J. Sailor (2009). "Biodegradable luminescent porous silicon nanoparticles for in vivo applications." Nature Materials **8**(4): 331-336.

Pic, E., T. Pons, L. Bezdetnaya, A. Leroux, F. Guillemin, B. Dubertret and F. Marchall (2010). "Fluorescence imaging and whole-body biodistribution of near-infrared-emitting quantum dots after subcutaneous injection for regional lymph node mapping in mice." Molecular Imaging and Biology **12**(4): 394-405.

Pons, T., E. Pic, N. Lequeux, E. Cassette, L. Bezdetnaya, F. Guillemin, F. Marchal and B. Dubertret (2010). "Cadmium-Free CuInS2/ZnS Quantum Dots for Sentinel Lymph Node Imaging with Reduced Toxicity." Acs Nano **4**(5): 2531-2538.

Pons, T., E. Pic, N. Lequeux, E. Cassette, L. Bezdetnaya, F. Guillemin, F. Marchal and B. Dubertret (2010). "Cadmium-free CuInS(2)/ZnS quantum dots for sentinel lymph node imaging with reduced toxicity." ACS Nano **4**(5): 2531-2538.

Porti, M., X. Blasco, M. Nafria and X. Aymerich (2003). "Electrical characterization and fabrication of SiO2 based metal-oxide-semiconductor nanoelectronic devices with atomic force microscopy." Nanotechnology **14**(6): 584-587.

Pozharski, E. V. and R. C. MacDonald (2007). "Single lipoplex study of cationic Lipoid-DNA, self-assembled complexes." Molecular Pharmaceutics **4**(6): 962-974.

Quek, C. H. L., K. W. (2012). "Near-Infrared fluorescent nanoprobes for in vivo optical imaging." Nanomaterials **2**(2): 92-112.

Raabe, A., J. Beck, R. Gerlach, M. Zimmermann and V. Seifert (2003). "Near-infrared indocyanine green video angiography: A new method for intraoperative assessment of vascular flow." Neurosurgery **52**(1): 132-139.

Richards, C. I., S. Choi, J. C. Hsiang, Y. Antoku, T. Vosch, A. Bongiorno, Y. L. Tzeng and R. M. Dickson (2008). "Oligonucleotide-stabilized Ag nanocluster fluorophores." Journal of the American Chemical Society **130**(15): 5038-5039.

Rieger, S., R. P. Kulkarni, D. Darcy, S. E. Fraser and R. W. Koster (2005). "Quantum dots are powerful multipurpose vital labeling agents in zebrafish embryos." Developmental Dynamics **234**(3): 670-681.

Roduner, E. (2006). "Size matters: why nanomaterials are different." Chemical Society Reviews **35**(7): 583-592.

Rogach, A. L., T. Franzl, T. A. Klar, J. Feldmann, N. Gaponik, V. Lesnyak, A. Shavel, A. Eychmuller, Y. P. Rakovich and J. F. Donegan (2007). "Aqueous synthesis of thiol-capped CdTe nanocrystals: State-of-the-art." Journal of Physical Chemistry C **111**(40): 14628-14637.

Rogach, A. L., M. T. Harrison, S. V. Kershaw, A. Kornowski, M. G. Burt, A. Eychmuller and H. Weller (2001). "Colloidally prepared CdHgTe and HgTe quantum dots with strong near-infrared luminescence." Physica Status Solidi B-Basic Research **224**(1): 153-158.

Rudin, M. (2009). "Noninvasive structural, functional, and molecular imaging in drug development." Current Opinion in Chemical Biology **13**(3): 360-371.

Rudin, M. and R. Weissleder (2003). "Molecular imaging in drug discovery and development." Nature Reviews Drug Discovery **2**(2): 123-131.

Sargent, E. H. (2012). "Colloidal quantum dot solar cells." Nature Photonics **6**(3): 133-135.

Sayes, C. M., A. A. Marchione, K. L. Reed and D. B. Warheit (2007). "Comparative pulmonary toxicity assessments of C-60 water suspensions in rats: Few differences in fullerene toxicity in vivo in contrast to in vitro profiles." Nano Letters **7**(8): 2399-2406.

Schaafsma, B. E., J. S. D. Mieog, M. Hutteman, J. R. Van der Vorst, P. J. K. Kuppen, C. Lowik, J. V. Frangioni, C. J. H. Van de Velde and A. L. Vahrmeijer (2011). "The clinical use of indocyanine green as a near-infrared fluorescent contrast agent for image-guided oncologic surgery." Journal of Surgical Oncology **104**(3): 323-332.

Schipper, M. L., N. Nakayama-Ratchford, C. R. Davis, N. W. S. Kam, P. Chu, Z. Liu, X. Sun, H. Dai and S. S. Gambhir (2008). "A pilot toxicology study of single-walled carbon nanotubes in a small sample of mice." Nature Nanotechnology **3**(4): 216-221.

Schneider, G. and G. Decher (2008). "Functional core/shell nanoparticles via layer-by-layer assembly. investigation of the experimental parameters for controlling particle aggregation and for enhancing dispersion stability." Langmuir **24**(5): 1778-1789.

Schuler, A., M. Python, M. V. del Olmo and E. de Chambrier (2007). "Quantum dot containing nanocomposite thin films for photoluminescent solar concentrators." Solar Energy **81**(9): 1159-1165.

Selvam, T. S. and K. M. Chi (2011). "Synthesis of hydrophobic gold nanoclusters: growth mechanism study, luminescence property and catalytic application." Journal of Nanoparticle Research **13**(4): 1769-1780.

Semonin, O. E., J. M. Luther and M. C. Beard (2012). "Quantum dots for next-generation photovoltaics." Materials Today **15**(11): 508-515.

Shang, L. and S. J. Dong (2009). "Sensitive detection of cysteine based on fluorescent silver clusters." Biosensors & Bioelectronics **24**(6): 1569-1573.

Shichibu, Y., Y. Negishi, H. Tsunoyama, M. Kanehara, T. Teranishi and T. Tsukuda (2007). "Extremely high stability of glutathionate-protected Au-25 clusters against core etching." Small **3**(5): 835-839.

Singhal, R. K., M. E. Anderson and A. Meister (1987). "Glutathione, a 1st line of defense against cadmium toxicity." Faseb Journal **1**(3): 220-223.

Sivaraman, D., P. Biswas, L. N. Cella, M. V. Yates and W. Chen (2011). "Detecting RNA viruses in living mammalian cells by fluorescence microscopy." Trends in Biotechnology **29**(7): 307-313.

Slotkin, J. R., L. Chakrabarti, H. N. Dai, R. S. E. Carney, T. Hirata, B. S. Bregman, G. I. Gallicano, J. G. Corbin and T. F. Haydar (2007). "In vivo quantum dot labeling of mammalian stem and progenitor cells." Developmental Dynamics **236**(12): 3393-3401.

Smith, A. M., S. Dave, S. M. Nie, L. True and X. H. Gao (2006). "Multicolor quantum dots for molecular diagnostics of cancer." Expert Review of Molecular Diagnostics **6**(2): 231-244.

Smith, A. M., M. C. Mancini and S. M. Nie (2009). "BIioimaging second window for in vivo imaging." Nature Nanotechnology **4**(11): 710-711.

Soderberg, K. A., G. W. Payne, A. Sato, R. Medzhitov, S. S. Segal and A. Iwasaki (2005). "Innate control of adaptive immunity via remodeling of lymph node feed arteriole." Proceedings of the National Academy of Sciences of the United States of America **102**(45): 16315-16320.

Soltesz, E. G., S. Kim, S. W. Kim, R. G. Laurence, A. M. De Grand, C. P. Parungo, L. H. Cohn, M. G. Bawendi and J. V. Frangioni (2006). "Sentinel lymph node mapping of the gastrointestinal tract by using invisible light." Annals of Surgical Oncology **13**(3): 386-396.

St John, A. L., C. Y. Chan, H. F. Staats, K. W. Leong and S. N. Abraham (2012). "Synthetic mast-cell granules as adjuvants to promote and polarize immunity in lymph nodes." Nature materials **11**(3): 250-257.

Staros, J. V., R. W. Wright and D. M. Swingle (1986). "Enhancement by N-hydroxysulfosuccinimide of water-soluble carbodiimide-mediated coupling reactions." Analytical Biochemistry **156**(1): 220-222.

Sun, Y., K. Balasubramanian, T. U. B. Rao and T. Pradeep (2011). "First principles studies of two luminescent molecular quantum clusters of silver, Ag(7)(H(2)MSA)(7) and Ag(8)(H(2)MSA)(8), based on experimental fluorescence spectra." Journal of Physical Chemistry C **115**(42): 20380-20387.

Susumu, K., B. C. Mei and H. Mattoussi (2009). "Multifunctional ligands based on dihydrolipoic acid and polyethylene glycol to promote biocompatibility of quantum dots." Nature Protocols **4**(3): 424-436.

Swayambunathan, V., D. Hayes, K. H. Schmidt, Y. X. Liao and D. Meisel (1990). "THIOL SURFACE COMPLEXATION ON GROWING CDS CLUSTERS." Journal of the American Chemical Society **112**(10): 3831-3837.

Taggart, D. P., B. Choudhary, K. Anastasiadis, Y. Abu-Omar, L. Balacumaraswami and D. W. Pigott (2003). "Preliminary experience with a novel intraoperative fluorescence imaging technique to evaluate the patency of bypass grafts in total arterial revascularization." Annals of Thoracic Surgery **75**(3): 870-873.

Tan, I. B., T. Ivanova, K. H. Lim, C. W. Ong, N. T. Deng, J. Lee, S. H. Tan, J. Wu, M. H. Lee, C. H. Ooi, S. Y. Rha, W. K. Wong, A. Boussioutas, K. G. Yeoh, J. So, W. P. Yong, A. Tsuburaya, H. Grabsch, H. C. Toh, S. Rozen, J. H. Cheong, S. H. Noh, W. K. Wan, J. A. Ajani, J. S. Lee, M. S. Tellez and P. Tan (2011). "Intrinsic Subtypes of Gastric Cancer, Based on Gene Expression Pattern, Predict Survival and Respond Differently to Chemotherapy." Gastroenterology **141**(2): 476-U551.

Tan, I. B., I. Ng, W. M. Tai and P. Tan (2012). "Understanding the genetic basis of gastric cancer: recent advances." Expert Review of Gastroenterology & Hepatology **6**(3): 335-341.

Tan, W. B., S. Jiang and Y. Zhang (2007). "Quantum-dot based nanoparticles for targeted silencing of HER2/neu gene via RNA interference." Biomaterials **28**(8): 1565-1571.

Tao, J., N. T. Deng, K. Ramnarayanan, B. H. Huang, H. K. Oh, S. H. Leong, S. S. Lim, I. B. Tan, C. H. Ooi, J. N. Wu, M. H. Lee, S. L. Zhang, S. Y. Rha, H. C. Chung, D. T. Smoot, H. Ashktorab, O. L. Kon, V. Cacheux, C. Yap, N. Palanisamy and P. Tan (2011). "CD44-SLC1A2 gene fusions in gastric cancer." Science Translational Medicine **3**(77).

Thayer, K. A., R. Melnick, K. Burns, D. Davis and J. Huff (2005). "Fundamental flaws of hormesis for public health decisions." Environmental Health Perspectives **113**(10): 1271-1276.

Tsay, J. M., M. Pflughoefft, L. A. Bentolila and S. Weiss (2004). "Hybrid approach to the synthesis of highly luminescent CdTe/ZnS and CdHgTe/ZnS nanocrystals." Journal of the American Chemical Society **126**(7): 1926-1927.

Turkevich, J., P. C. Stevenson and J. Hillier (1951). "A study of the nucleation and growth processes in the synthesis of colloidal gold." Discussions of the Faraday Society(11): 55-75.

Uyeda, H. T., I. L. Medintz, J. K. Jaiswal, S. M. Simon and H. Mattoussi (2005). "Synthesis of compact multidentate ligands to prepare stable hydrophilic quantum dot fluorophores." Journal of the American Chemical Society **127**(11): 3870-3878.

Vogel, E. M. (2007). "Technology and metrology of new electronic materials and devices." Nature Nanotechnology **2**(1): 25-32.

Wagner, V., A. Dullaart, A. K. Bock and A. Zweck (2006). "The emerging nanomedicine landscape." Nature Biotechnology **24**(10): 1211-1217.

Wang, G. L., T. Huang, R. W. Murray, L. Menard and R. G. Nuzzo (2005). "Near-IR luminescence of monolayer-protected metal clusters." Journal of the American Chemical Society **127**(3): 812-813.

Weber, M. J. (2003). "Handbook of Optical Materials." Boca Raton, CRC Press: 5.4.

Wei, H., Z. D. Wang, L. M. Yang, S. L. Tian, C. J. Hou and Y. Lu (2010). "Lysozyme-stabilized gold fluorescent cluster: Synthesis and application as Hg(2+) sensor." Analyst **135**(6): 1406-1410.

Weissleder, R. (2001). "A clearer vision for in vivo imaging." Nature Biotechnology **19**(4): 316-317.

Weissleder, R. (2002). "Scaling down imaging: Molecular mapping of cancer in mice." Nature Reviews Cancer **2**(1): 11-18.

Weissleder, R. and V. Ntziachristos (2003). "Shedding light onto live molecular targets." Nature Medicine **9**(1): 123-128.

Weissleder, R., C. H. Tung, U. Mahmood and A. Bogdanov (1999). "In vivo imaging of tumors with protease-activated near-infrared fluorescent probes." Nature Biotechnology **17**(4): 375-378.

Welsher, K., Z. Liu, S. P. Sherlock, J. T. Robinson, Z. Chen, D. Daranciang and H. J. Dai (2009). "A route to brightly fluorescent carbon nanotubes for near-infrared imaging in mice." Nature Nanotechnology **4**(11): 773-780.

Welsher, K., S. P. Sherlock and H. J. Dai (2011). "Deep-tissue anatomical imaging of mice using carbon nanotube fluorophores in the second near-infrared window." Proceedings of the National Academy of Sciences of the United States of America **108**(22): 8943-8948.

Wu, X., X. He, K. Wang, C. Xie, B. Zhou and Z. Qing (2010). "Ultrasmall near-infrared gold nanoclusters for tumor fluorescence imaging in vivo." Nanoscale **2**(10): 2244-2249.

Wu, Z. K. and R. C. Jin (2010). "On the ligand's role in the fluorescence of gold nanoclusters." Nano Letters **10**(7): 2568-2573.

Xie, J. P., Y. G. Zheng and J. Y. Ying (2009). "Protein-directed synthesis of highly fluorescent gold nanoclusters." Journal of the American Chemical Society **131**(3): 888-889.

Xie, R. G. and X. G. Peng (2009). "Synthesis of Cu-doped InP nanocrystals (d-dots) with ZnSe diffusion barrier as efficient and color-tunable NIR emitters." Journal of the American Chemical Society **131**(30): 10645-10651.

Xing, G., W. Ji, Y. Zheng and J. Y. Ying (2008). "High efficiency and nearly cubic power dependence of below-band-edge photoluminescence in water-soluble, copper-doped ZnSe/ZnS quantum dots." Optics Express **16**(8): 5710-5715.

Yamamoto, M., S. Sasaguri and T. Sato (2011). "Assessing intraoperative blood flow in cardiovascular surgery." Surgery Today **41**(11): 1467-1474.

Yu, J., S. A. Patel and R. M. Dickson (2007). "In vitro and intracellular production of peptide-encapsulated fluorescent silver nanoclusters." Angewandte Chemie-International Edition **46**(12): 2028-2030.

Yu, J. H., S. Choi and R. M. Dickson (2009). "Shuttle-based fluorogenic silver-cluster biolabels." Angewandte Chemie-International Edition **48**(2): 318-320.

Yuan, X., Z. T. Luo, Q. B. Zhang, X. H. Zhang, Y. G. Zheng, J. Y. Lee and J. P. Xie (2011). "Synthesis of highly fluorescent metal (Ag, Au, Pt, and Cu) nanoclusters by electrostatically induced reversible phase transfer." ACS Nano **5**(11): 8800-8808.

Zhang, L., F. X. Gu, J. M. Chan, A. Z. Wang, R. S. Langer and O. C. Farokhzad (2008). "Nanoparticles in medicine: Therapeutic applications and developments." Clinical Pharmacology & Therapeutics **83**(5): 761-769.

Zhang, W. J. and X. H. Zhong (2011). "Facile synthesis of ZnS-CuInS2-alloyed nanocrystals for a color-tunable fuorchrome and photocatalyst." Inorganic Chemistry **50**(9): 4065-4072.

Zhang, W. J. and X. H. Zhong (2011). "Facile synthesis of ZnS-CuInS(2)-alloyed nanocrystals for a color-tunable fluorchrome and photocatalyst." Inorganic Chemistry **50**(9): 4065-4072.

Zhang, Y. P., P. Sun, X. R. Zhang and W. L. Yang (2012). "In vitro gastric cancer cell imaging using near-infrared quantum dot-conjugated CC49." Oncology Letters **4**(5): 996-1002.

Zheng, J., P. R. Nicovich and R. M. Dickson (2007). Highly fluorescent noble-metal quantum dots. Annual Review of Physical Chemistry. Palo Alto, Annual Reviews. **58:** 409-431.

Zheng, Y. G., S. J. Gao and J. Y. Ying (2007). "Synthesis and cell-imaging applications of glutathione-capped CdTe quantum dots." Advanced Materials **19**(3): 376-380.

Zimmer, J. P., S. W. Kim, S. Ohnishi, E. Tanaka, J. V. Frangioni and M. G. Bawendi (2006). "Size series of small indium arsenide-zinc selenide core-shell nanocrystals and their application to in vivo imaging." Journal of the American Chemical Society **128**(8): 2526-2527.

Zintchenko, A., A. S. Susha, M. Concia, J. Feldmann, E. Wagner, A. L. Rogach and M. Ogris (2009). "Drug nanocarriers labeled with near-infrared-emitting quantum dots (quantoplexes): Imaging fast dynamics of distribution in living animals." Molecular Therapy **17**(11): 1849-1856.

Biography

Chai Hoon Quek was born on October 8, 1971 and raised in Singapore. She graduated with a Bachelor of Science degree in 1993. She was awarded the National University of Singapore Graduate Research Scholarship in 2000-2001 to pursue a graduate degree with the Department of Chemistry at National University of Singapore and graduated with a Master of Science degree in 2003. In 2007, she came to Duke University to enroll in graduate program and received Master of Science degree with the Department of Mechanical Engineering and Materials Science in 2008. She continued her doctoral studies in the Department of Mechanical Engineering and Materials Science at Duke Univeristy in 2009. Under the supervision of D. Kam Leong, her research focused on developing biocompatible quantum dots for biological applications. During 2010-2011 she was awarded Medtronic Fellowships at Duke University. As part of her training, she has mentored two undergraduate students and undertook teaching assistant duties for the Structure and Properties of Solids class.